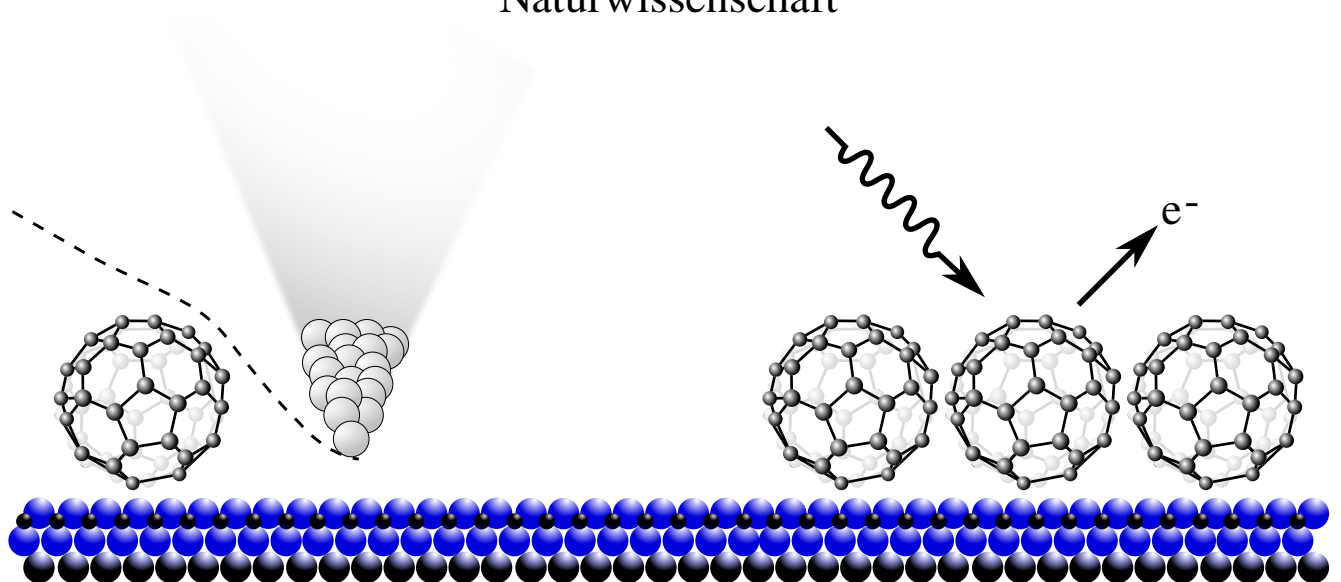


Fullerene and bismuth clusters on nanostructured oxide films: Influence of nearest neighbors and surface contribution on charging energy

Dissertation

Zur Erlangung des Doktorgrades der
Naturwissenschaft



Lehrstuhl für Experimentelle Physik I
Fakultät Physik
Technische Universität Dortmund

vorgelegt von
Alexander Kononov

Erstgutachter: Apl. Prof. Dr. Heinz Hövel

Zweitgutachter: Apl. Prof. Dr. Ilya Akimov

Abgabedatum: 29.05.2024

Prüfungsdatum: 19.07.2024

Abstract

In this study, C_{60} molecules and Bi clusters are investigated on the surfaces of two noble metals (Au(111) and Ag(111)) and on the surface of $Al_2O_3||Ni_3Al$, characterized by very low conductivity. For the investigation, ultraviolet photoelectron spectroscopy (UPS) and scanning tunneling microscope (STM) are used in ultra-high vacuum (UHV). On the $Al_2O_3||Ni_3Al$ surface, both C_{60} and Bi clusters exhibit a noticeable shift of the photoemission signal due to the influence of the charging energy: in the case of C_{60} , this shift is attributed to the energy shift of the HOMO, while for Bi clusters, it is visible for the shift of the core level. Conversely, minimal shifts are observed on metal surfaces. For C_{60} , the shift originates from the reduction in charging energy induced by next-neighbor screening, whereas for Bi clusters, it is attributed to the increase in cluster size, with the influence of the $Ni_3Al(111)$ surface playing a significant role in the change of core level shift. Both effects are explained within the electrostatic approximation, which overlooks quantum mechanical effects like local electron density distribution or electron spill-out, yet still yields excellent agreement with experimental results. Furthermore, STM investigations reveal evidence of Bi cluster adsorption on the periodic superstructure of the $Al_2O_3||Ni_3Al$ surface, and potentially even adsorption of C_{60} molecules on the periodic structure of the $Al_2O_3||Ni_3Al$ network.

Kurzfassung

In der vorliegenden Arbeit werden C_{60} -Moleküle und Bi-Cluster auf den Oberflächen von zwei Edelmetallen (Au(111) und Ag(111)) sowie auf der Oberfläche von $Al_2O_3||Ni_3Al$, das durch sehr niedrige Leitfähigkeit gekennzeichnet ist, untersucht. Zur Untersuchung werden Ultraviolettphotoelektronenspektroskop (UPS) und Rastertunnelmikroskop (RTM) in Ultrahochvakuum (UHV) eingesetzt. Auf der $Al_2O_3||Ni_3Al$ -Oberfläche zeigen sowohl C_{60} -Moleküle als auch Bi-Cluster eine deutliche Verschiebung des Photoemissionssignals aufgrund des Einflusses der Ladungsenergie: Im Fall von C_{60} werden dieser Effekt der Verschiebung des Energieniveaus des highest occupied molecular orbital (HOMO) zugeschrieben, während bei Bi-Clustern die Verschiebung des Kernniveaus beobachtet wird. Im Gegensatz dazu werden auf Metalloberflächen nur minimale Verschiebungen festgestellt. Für C_{60} resultiert die Verschiebung aus der Reduktion der Ladungsenergie, die durch die Abschirmung durch Nachbarn hervorgerufen wird, während sie bei Bi-Clustern auf die Zunahme der Clustergröße zurückzuführen ist, wobei der Einfluss der $Ni_3Al(111)$ -Oberfläche eine bedeutende Rolle bei der Veränderung des Photoemissionssignals des Kernniveaus spielt. Beide Effekte können innerhalb der elektrostatischen Näherung erklärt werden. Dabei werden die quantenmechanischen Effekte wie lokale Elektronendichteverteilung oder der Elektron spill-out außer Acht gelassen. Dennoch zeigt diese Näherung eine ausgezeichnete Übereinstimmung mit den experimentellen Ergebnissen. Darüber hinaus zeigen STM-Untersuchungen Hinweise auf die Adsorption von Bi-Clustern auf der periodischen Superstruktur der $Al_2O_3||Ni_3Al$ -Oberfläche und möglicherweise sogar die Adsorption von C_{60} -Molekülen auf der periodischen Struktur des $Al_2O_3||Ni_3Al$ -Netzwerks.

Contents

1. Introduction	1
2. Essential concepts	3
2.1. Clusters	3
2.2. Clusters on surfaces	7
2.2.1. Simple picture of PVD growth	8
2.2.2. Post deposition growth	10
2.3. Experimental techniques	11
2.3.1. Low Energy Electron Diffraction	11
2.3.2. Scanning tunneling microscope	14
2.3.3. Photoemission Spectroscopy	18
2.4. Experimental setup	21
3. Samples	23
3.1. Oxide Layer on Ni ₃ Al(111) crystal	23
3.2. Fullerene C ₆₀	25
3.3. Bismuth	26
4. Results	29
4.1. Fullerene C ₆₀	30
4.1.1. Deposition	30
4.1.1.1. Calibration with STM	31
4.1.1.2. Calibration with AFM	32
4.1.2. C ₆₀ on Ag(111)	34
4.1.3. C ₆₀ on Au(111)	35
4.1.4. C ₆₀ on Al ₂ O ₃ Ni ₃ Al(111)	39
4.1.5. Discussion	45
4.2. Bismuth	50
4.2.1. Deposition	50
4.2.1.1. Calibration with QCM	51
4.2.1.2. Precision calibration with LEED	53
4.2.2. Bi on Au(111)	54
4.2.3. Bi on Al ₂ O ₃ Ni ₃ Al	59

4.2.4. Discussion	63
4.2.4.1. Charging energy of Bi clusters	66
4.2.4.2. Substrate contribution	68
5. Summary and outlook	73
A. Appendix	75
A.1. Energy position of HOMO in UPS	75
A.1.1. Smoothing	75
A.1.2. Peak onset position	76
A.2. UPS experimental resolution	77
A.3. Line shape of core level in UPS	79
A.4. Cluster height determination in STM images	79
A.5. Error Propagation	82
A.5.1. Capacitance of a sphere in vicinity of surface.	82
B. Supplementary material	83
B.1. C ₆₀ on Au(111)	84
B.1.1. Au(111) clean surface	84
B.1.2. 0.02 ML C ₆₀ Au(111)	86
B.2. C ₆₀ on Al ₂ O ₃ Ni ₃ Al	88
B.3. Al ₂ O ₃ Ni ₃ Al preparation procedure	88
B.4. Separated C ₆₀ islands deposited at room temperature	89
B.5. C ₆₀ highly ordered pyrolytic graphite (HOPG)	90
B.6. Bi on Au(111)	91
B.7. Bi on Al ₂ O ₃ Ni ₃ Al	93
Bibliography	95

1. Introduction

In recent years, there has been a significant trend towards miniaturization across both science and technology. In electronics, chip manufacturing is on the cusp of transitioning from the nanometer (nm) to the ångström (Å) scale [1, 2]. Another example is a C₆₀ molecule, which, with the size of approximately 1 nm, holds potential as a quantum computing unit [3, 4]. Moreover, in medicine C₆₀ molecules are being investigated as contrast enhancers in nuclear magnetic resonance (NMR) imaging [5] and as potential drug delivery systems in the fight against cancer [6, 7].

Meanwhile, nano-quantum dots (QDs) offer promising prospects for establishing highly secure quantum communication channels [8, 9].

While some of these concepts have already permeated everyday life, for example QDs in the display industry [10], the underlying physics remain incompletely understood. In such small-scale structures, the addition or removal of even a single atom can lead to drastic changes in macroscopic properties [11]. As a result, this area of research holds immense potential for new discoveries.

The best way to study small, well-defined nano-objects is to isolate and measure these structures in an environment with minimal interaction. One approach to achieve this are free beam experiments, where clusters are produced in vacuum, e.g. by gas phase aggregation [12], and either fly in a beam through an experimental setup [13] or are confined in an ion trap [14] for study. However, for practical applications, the clusters need to be supported, i.e. deposited and stabilized on a surface. While this adds complexity due to the interaction between the clusters and the surface, it can also reveal new effects.

In the scope of this thesis the combination of a nanostructured surface of an oxide film (grown on Ni₃Al(111) crystal) ¹ and two different adsorbed materials: Fullerene (C₆₀) and bismuth were investigated. The choice of Bi as cluster material is motivated by studies of Pb clusters in the free beam [15], which indicated a metal-to-nonmetal transition similar to that observed for Hg clusters (see section 2.1). This transition was studied by the size-dependent shift of the Pb 5d_{5/2} core level in x-ray photoelectron spectroscopy (XPS). For Bi, a similar effect could occur for the 5d_{5/2} level using an oxide film to decouple the clusters from the substrate, thereby avoiding strong cluster-substrate interaction. In the present work these studies began by comparing the results for Bi clusters with C₆₀ as a well-known model system. Several effects which have to be included in the analysis of the photoemission data in order to describe such cluster-surface system were investigated.

In the case of C₆₀, the cluster structure is fixed, while bismuth forms clusters during the deposition process, likely due to the nanostructure of the substrate. The pre-synthesized C₆₀ molecules initially follow the nanostructure of the surface and then form larger islands. The increase in size of the Bi clusters was

¹Also the surface of Au(111) and Ag(111) was used, mainly as a metallic reference to the non-conducting Al₂O₃||Ni₃Al layer.

achieved by depositing Bi atoms on the surface at low temperatures, primarily at liquid nitrogen (LN_2) temperature, followed by gradual annealing at higher temperatures. For C_{60} , commercially available pre-synthesized molecules were deposited at low temperature, and their aggregation into larger islands was observed during annealing.

The investigations were carried out in UHV using three methods: STM, UPS, and low-energy electron diffraction (LEED). The latter method was used only to verify the quality of the substrate and to determine more precisely the amount of bismuth deposited.

The content of the current thesis is structured as follows:

Chapter 2 provides a concise overview of the cluster concept and the topic of cluster-surface interaction, detailing the experimental techniques employed and describing the experimental setup utilized.

Chapter 3 offers an overview of the primary substrate utilized ($\text{Al}_2\text{O}_3||\text{Ni}_3\text{Al}$) and describes the adsorbate materials: Bi and C_{60} .

In the first part of Chapter 4, the calibration of the C_{60} evaporator is detailed alongside the results of experiments conducted with C_{60} on the surfaces of Au(111), Ag(111), and $\text{Al}_2\text{O}_3||\text{Ni}_3\text{Al}$. Additionally, this chapter presents the electrostatic model, which describes the influence of the nearest neighbors of C_{60} on the charging energy, resulting in the shift of the HOMO level in UPS spectra.

The second part of Chapter 4 presents the results of experiments conducted with Bi both on the surface of Au(111) and on the surface of $\text{Al}_2\text{O}_3||\text{Ni}_3\text{Al}$. In this case, the core level shift could also be explained by the electrostatic model. However, due to the different incorporation of Bi clusters compared to pre-synthesized C_{60} molecules, the primary factor influencing the change in the charging energy, as measured by the shift of the core level in UPS spectra, is the proximity of the metal surface of the $\text{Ni}_3\text{Al}(111)$ beneath the Al_2O_3 layer.

Chapter 5 concludes with a brief summary of the results and provides additional suggestions for further possible investigations on the current systems.

2. Essential concepts

In this chapter, a brief overview of the concept of metallic clusters, as well as their growth on surfaces, will be provided. Following this, a short description of the techniques used is presented, with minimal theoretical background.

2.1. Clusters

For many centuries people have philosophized about the construction of the matter from the single atoms [18]. However, only in 19th and 20th century the existence of the atom, even if not directly, was proved¹. The discovery of the STM [21] allowed the observation of surfaces on the atomic scale. Since then, many other techniques have been developed to the point where they also allow atomic resolution, extending and intensifying the study of clusters and their properties (e.g. scanning transmission electron microscopy (STEM))[22, 23].

In general, a cluster is a collection of objects that either have the same properties or are bound together under certain conditions or can be classified into a certain class. There are e.g. clusters in astrophysics (galaxy cluster: collection of galaxies bound by gravity, asteroid cluster: asteroid families such as Karin cluster [24]) or in computer science (computer cluster: network of several computers, data cluster: grouping of data into clusters with the same properties [25]). Furthermore, this term appears in engineering, biology, chemistry, environmental science, neuroscience, plant science, telecommunication and so on. Therefore, when researching and revising the literature, the emphasis must be placed on the field of interest. For instance, when searching for the term “cluster” in the titles and topics of publications using the online database “Web of Science” [26], over 200 000 papers from the last 40 years are retrieved. By filtering the search to include only physics, chemistry, material science, and similar fields, the results are narrowed down to “only” over 90 000 papers. Nonetheless, it still shows that there have been enormous efforts and many investigations in the last half century in the field of cluster physics and cluster chemistry. In the latter, the clusters are often synthesized from pre-agents by chemical reaction and usually stored in a kind of liquid stabilizer to avoid coagulation. In the present work we deal with the clusters produced and studied by physical processes in vacuum. So when clusters are mentioned in this work, it refers to the accumulation of atoms.

If one examines the physical or chemical properties of small particles, in some cases enormous deviations from the properties of the underlying atoms and/or from the properties of the solids, which are “built up” from these atoms, can appear. This emerges because of electron confinement and high surface to volume ratio. The general property change with cluster size can be roughly represented in an empirical graph

¹The main contribution to the consolidation of the general opinion in the scientific community about the real existence of atoms was made in Albert Einstein’s paper of 1905. [19]. Which was later confirmed by experiments [20].

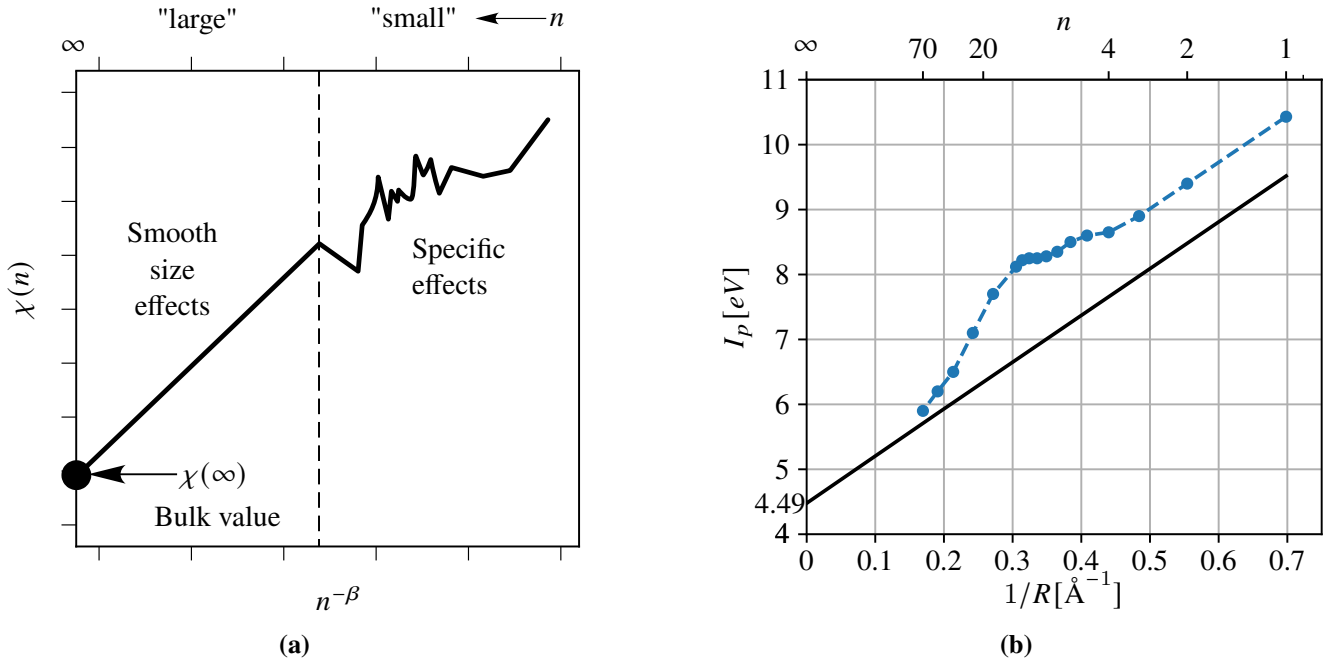


Figure 2.1.: (a) The cluster size dependence of a cluster property $\chi(n)$ on the number, n , of the cluster constituents. The data is plotted vs $n^{-\beta}$ where $0 \leq \beta \leq 1$. “Small” clusters reveal specific size effects, while “large” clusters are expected to exhibit for many properties a “smooth” size dependence of $\chi(n)$ which converges for $n \rightarrow \infty$ to the bulk value $\chi(\infty)$ [16]. (b) Comparison of the experimentally determined ionization potential data with the predictions of the classical spherical-droplet model (solid black line)[17]. Ionization potential data are plotted vs $1/R$, where R is the radius of the clusters calculated from the number of atoms per cluster using the equation 2.2 and 2.1

as shown in Figure 2.1(a). The cluster properties $\chi(n)$ can be structural, energetic, electromagnetic and so on, with n as the number of clusters or atoms per clusters, depending on the representation. The size dependence can be divided into two regimes: smooth cluster size effects, which occur in “large” clusters and converge towards the properties of the bulk material, and the specific cluster size effects, which can be found in “small” clusters and show dramatic deviations from the properties of the corresponding bulk material[16, p.2]. An example of such behavior of clusters with size change is shown in Figure 2.1(b), where the ionization potential I_p of mercury clusters is plotted against their size. Here, the straight line represents a classical electrostatic approximation where the clusters are assumed to be uniformly conducting spheres of radius R . The radius R corresponds to the size of the clusters with the assumption of the density of the bulk material and can be calculated according to the Wigner-Seitz radius r_s equation:

$$r_s = \left(\frac{3M}{4\pi Z\rho N_A} \right)^{\frac{1}{3}} \quad (2.1)$$

Where M corresponds to the molar mass, ρ to the density of the bulk material, Z is the amount of free electrons per atom and N_A stands for the Avogadro constant. One can approximate the radius of the clusters R according to the equation (2.2) as the Wigner-Seitz radius times the number of atoms per cluster n .

$$R = r_s n^{\frac{1}{3}} \quad (2.2)$$

Now with this radius we can calculate the energy E needed to remove one electron from the cluster. For

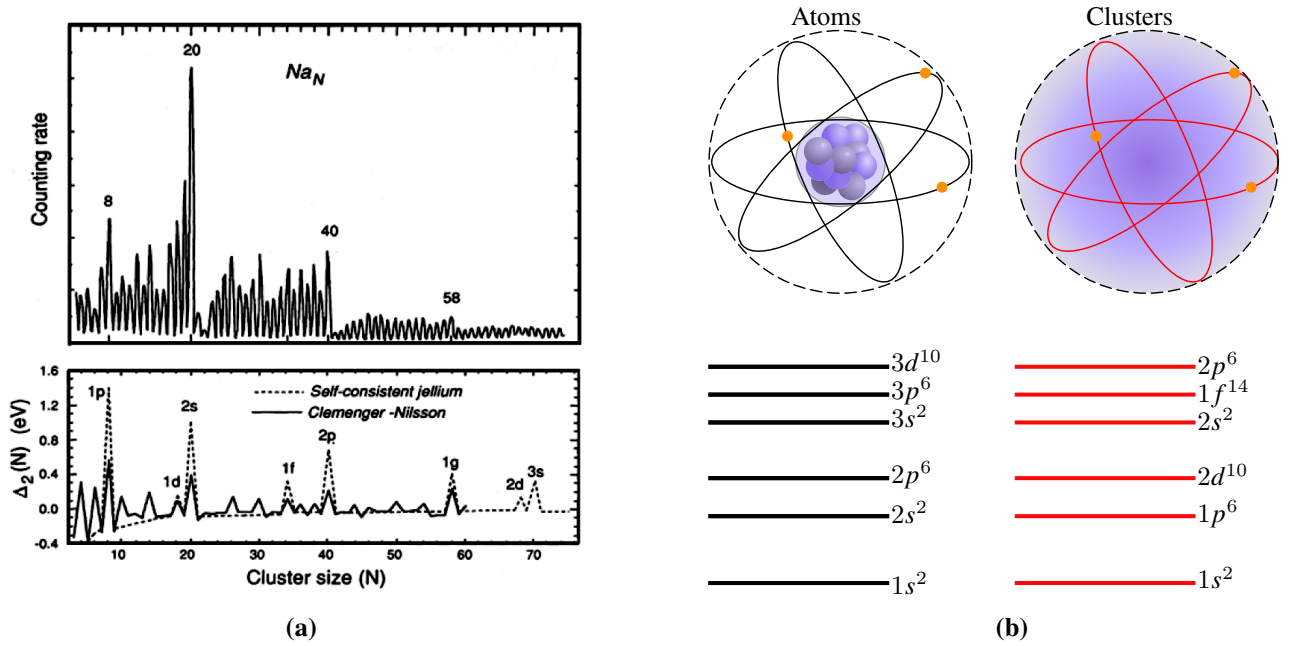


Figure 2.2.: (a) Top: Experimental data of a sodium cluster mass spectrum from [28]. Bottom: Second derivative of the Energy, dashed line using Wooden-Saxon potential (Jellium Model) and solid line using the ellipsoidal shell (Clemenger-Nilsson model) [29]. (b) Schematic diagram of an atom with localized positive charge at the nucleus and the corresponding atomic orbitals (left side), and jellium model of a cluster where the positive charge is distributed in a sphere of finite radius with corresponding electronic orbitals (right side). Based on [30].

a metallic sphere this energy is given by:

$$E = \frac{1}{2}CU^2 = \frac{1}{2}\frac{Q^2}{C} = \frac{1}{2}\frac{Q^2}{4\pi\epsilon_0 R} \quad Q=e \quad = \frac{1}{2}\frac{e^2}{4\pi\epsilon_0 R} [J] = \frac{1}{2}\frac{e}{4\pi\epsilon_0 R} [\text{eV}] \quad (2.3)$$

With $C = 4\pi\epsilon_0 R$ as the capacitance of a sphere, ϵ_0 the electric field constant, U the electric voltage, Q the charge and e^- the elementary charge. Now we can calculate the ionization potential I_p as shown in equation (2.4).

$$I_p = w + \frac{1}{2}\frac{e}{4\pi\epsilon_0 R} \quad (2.4)$$

where w represents the work function [17]. The value for the work function of Hg bulk material $w = 4.49\text{eV}$ is taken from [27]. In figure 2.1(b) the values of the ionization potential are plotted against the inverse radius of the clusters. As you can see with the increase of the cluster size the value of the ionization potential converges against the value of the bulk material. However, for small clusters this value differs enormously from the expected value (about 2 eV for $n \leq 20$). Rademann et al. [17] explain this phenomenon by the metal-to-nonmetal transition (MTNT), where the fully occupied s-derived valence band of small Hg clusters is energetically separated from the empty p-derived conduction band and with increasing cluster size both bands overlap, which causes the non-metallic small clusters to become large clusters with electronic properties of the bulk material. This is an example of the unusual behavior of small clusters. Specific size effects were also obtained by mass spectroscopy of sodium clusters. It was found that clusters with the number of atoms of 8, 20, 40, 58 are particularly abundant and probably more stable. These abundant clusters were called “magic numbers” in pendant to Nuclear physics. The idea was that the closed electron shells explain the stability of the clusters. To verify this, a model was set up where the positive charge of the individual atoms of the clusters was not considered as localized but as a sphere for the whole cluster with radius R where the positive charge is homogeneously distributed

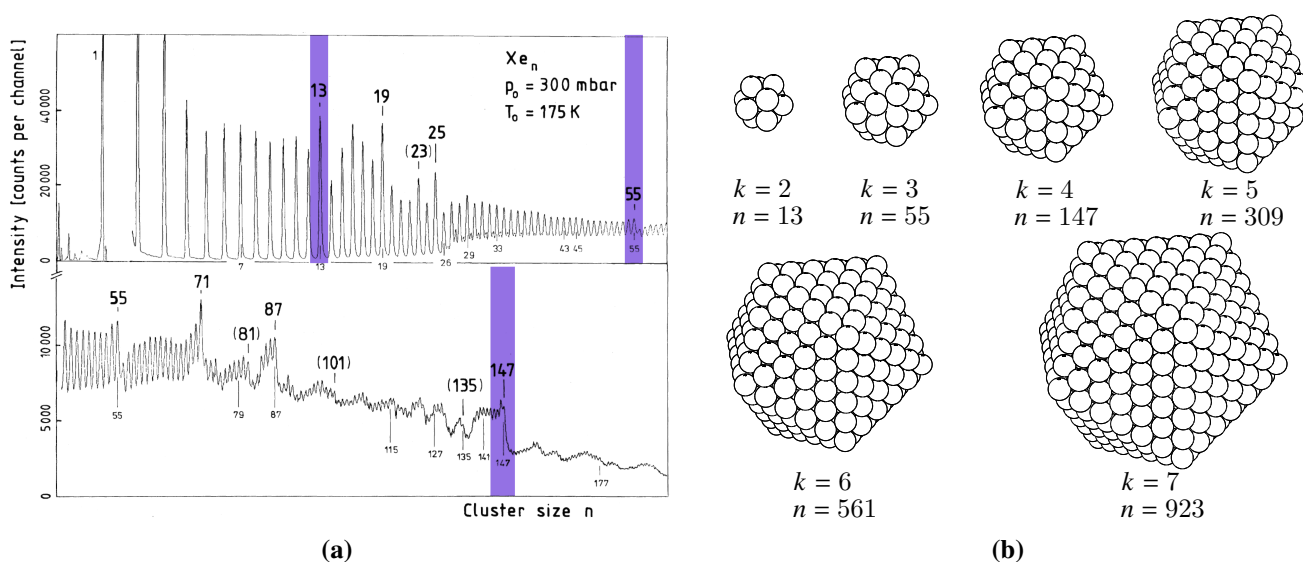


Figure 2.3.: (a) Mass spectrum of Xe clusters in the gas phase. Geometric magic numbers which can be explained by Mackay Icosahedra geometry are denoted by the violet stripes [32]. (b) First six Mackay Icosahedra. k and n represent closed shells number and number of atoms in cluster respectively.

(Figure 2.2(b)). However, as you can see in Figure 2.2(a) (top), the clusters with even number of atoms are more abundant than those with odd number of atoms. This cannot be explained by the Jellium model because sodium clusters with an odd number of atoms undergo distortion to an elliptical geometry. This phenomenon can be explained by applying the Nilsson model [31], as shown in Figure 2.2(a) (bottom). Another very prominent example of cluster stability can be found in noble gas clusters. Here the stability is explained by the atomic shell closure rather than by electronic shell closure. The magic numbers can be explained by Mackay Icosahedra geometry and denoted in the equation (2.5) based on the atoms per cluster n needed for closing one particular shell k .

$$n = \frac{1}{3} (10k^3 - 15k^2 + 11k - 3) \quad (2.5)$$

So for shell numbers $k = 2, 3, 4, 5, 6, \dots$ you will need $n = 13, 55, 147, 309, 561, \dots$ atoms respectively. This is often referred to as geometric magic numbers in comparison to electronic magic numbers. These geometric magic numbers were first theoretically predicted, but the first experimental evidence was found later in Xe clusters (see Figure 2.3(a)). The high ratio of atoms on the surface to atoms inside the cluster can be illustrated by the example of the Mackay Icosahedral clusters (see table 2.1). For the first five shells the ratio of surface to volume is higher than 50%. One can wonder why in the mass spectrum (see Figure 2.3(a)) one does not only see the magic numbers of the icosahedral structure (13, 55, 147) but also the $n = 19, 25, 71, \dots$

According to [32], this could be due to the growth process of the clusters, where the cluster cools down by evaporating an atom and transitions from a liquid state to a solid state. This solid state is more stable because further transformation requires a certain amount of energy to overcome the energy barrier. Consequently, additional preferable cluster sizes are found in the spectra, which could represent the metastable state of clusters. Nevertheless, the stability of the icosahedral shells is clearly evident.

So we can assume that the stability of the Xe clusters largely arises from the closure of geometric shells. This is an extreme example where two effects can be considered separately because the closed atomic shells in the Xe (noble gas) clusters are chemically inert, therefore the atoms in those clusters are

connected by the van der Waal's interaction. Usually the stability of clusters based on atomic packing and electron shell closure are intertwined. The jellium model, which was briefly touched upon above, has been successfully applied in the study of clusters consisting of simple metals (alkali metals, alkaline earth metals and noble metals). However, this model fails in the description of clusters composed of transition metals, rare earth metal atoms, semiconductors or insulators. So one has to resort to the more complex and costly methods of first-principle calculations [30].

2.2. Clusters on surfaces

How strong the interaction between clusters (or in general adsorbates, which could be atoms as well) and surfaces is, can be described in terms of the energy required to release the bond. Weak bonding can be released with small energy transfers (e.g. small temperature increases). This type of bonding is most often referred to as physisorption. On the other hand, bond that requiring several hundreds of Kelvin to break are called chemisorption. The latter can be described by the charge transfer. Depending on the localization of the electron orbitals in k-space, a distinction can be made between ionic, covalent and metallic bonds [34].

In order to discuss or study the interaction between clusters and surfaces, the clusters must first be brought onto a surface. In UHV this can be done in different ways. For example by preforming clusters in the gas phase (mass selected or with broad mass distribution). In this case, first the atoms are extracted from the base material by e.g. magnetron sputtering, laser ablation or thermal heating, then the clusters are nucleated either in a Penning trap or in a gas-filled chamber. After that, the clusters are usually passed through electronic lenses and deposited on the surface. There are several ways to select the clusters by mass before deposition. This method is excellent for the precise investigation of certain cluster sizes, but it has a disadvantage: the amount of produced clusters is usually so small that the interesting properties are only detectable with very sensitive methods and therefore play a minor role in the industry anyway. Another approach is to omit the step of cluster nucleation and proceed directly to the deposition of the atoms on the surface where the clusters are formed by diffusion. This technique is called physical vapor deposition (PVD) and is widely used in industrial applications along with chemical vapor deposition (CVD). PVD can be further subdivided into: (1) thermal evaporation (molecular beam epitaxy, electron

Table 2.1.: Surface ratios for Mackay Icosahedral clusters. k stands for the closed shell number, n is the number of atoms in a cluster and n_s represents the number of surface atoms in a cluster [33]

k	n	n_s	n_s/n
1	1		
2	13	12	0.92
3	55	42	0.76
4	147	92	0.63
5	309	162	0.52
6	561	252	0.45
7	923	362	0.39
8	1415	492	0.35
9	2057	642	0.31
10	2869	812	0.28

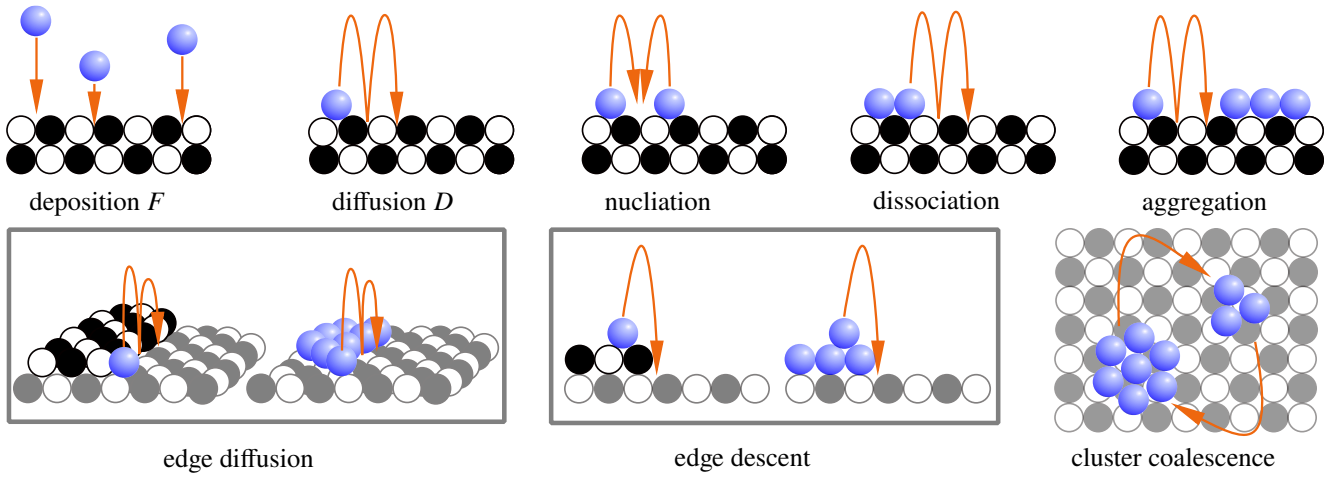


Figure 2.4.: Schematic process of PVD. From left to right: Deposition: atoms impact on to surface. Diffusion: atom propagates on the surface when the energy is sufficient for a jump. Nucleation: two atoms form a dimer. Dissociation: dimer or cluster loses one atom. Aggregation: cluster gets an additional atom. Edge diffusion: Atom migrates along either the step edge of the substrate (denoted by black and white spheres) or the edge of a cluster (purple spheres). Edge descent: Atom from the top of the step edge or from the top of the cluster drops onto the terrace below. Cluster coalescence: two clusters are binding. Inspired by [34]

beam physical vapor deposition (EB-PVD), pulsed laser deposition), (2) ion sputtering (DC-, AC-, RF-sputtering, magnetron sputtering, ion beam sputtering, reactive sputtering), and (3) arc discharge (cathodic-, anodic- arc deposition, reactive arc vapor deposition) [35]. In this work, the clusters were fabricated using the EB-PVD method and therefore this method and the corresponding growth process will be explained in more detail.

2.2.1. Simple picture of PVD growth

In the process of the deposition of atoms on the surface by PVD, the thermal energy of the atoms plays an important role. If an atom with high energy impacts the surface, it will not be completely adsorbed on the crystal lattice and the atoms will diffuse on the surface, find other atoms and aggregate. This is not always desirable because, otherwise, the growth is determined not only by the statistical impact of the clusters but also by diffusion, nucleation, and dissociation. On the other hand, when the thermal energy is low, the atoms remain directly at the impact sites of the lattice, where they are in thermal equilibrium with the surface, thus at low temperature inhibiting diffusion and consequently nucleation or/and aggregation. To achieve this, the surface is cooled to low temperatures so that all the thermal energy of the atoms is dissipated. Control over cluster growth can then be achieved by sequentially adding energy to the system, e.g. by heating [34]. Figure 2.4 illustrates the processes involved in the growth of the clusters during PVD. Using mean-field nucleation theory with the assumption that the atoms wet the surface forming 2D clusters and that the energy needed to make a jump from one lattice site to another is $E \ll k_B T$, the diffusion process of atoms on a surface can be described by Boltzmann statistics:

$$\nu = \nu_0 e^{-\frac{E}{k_B T}} \quad (2.6)$$

With ν as the jump rate and ν_0 being the attempt frequency, which is typical in the range of $10^{12} - 10^{13}$ Hz. The saturation cluster density of stable islands n_x per unit cell can be described as follows [36]:

$$n_x \approx \eta(\theta) \left(\frac{D}{F} \right)^{-\chi} \exp \left(\frac{E_i}{(i+2)k_B T} \right), \text{ with } \chi = \frac{i}{i+2} \quad (2.7)$$

Thereby $\eta(\theta, i)$ is the complete saturation² density at coverage θ , i the critical cluster size³, D the diffusion rate, F the flux or the deposition rate: atoms per square meter and second and E_i the cluster binding energy ($E_1 = 0$). At low temperatures, the critical size remains constant, resulting in a small value for i . Additionally, the value of i is dependent on surface symmetry. For hexagonal surfaces, i is expected to be 1 or 2, while for surfaces with square symmetry, i can take on values of 1, 3, or 8 [36]. If dimers remain stable, i becomes 1 and Equation 2.7 simplifies to:

$$n_x = \eta(\theta, 1) \left(\frac{D}{F} \right)^{-\frac{1}{3}} \quad (2.8)$$

The diffusion rate D is given by:

$$D = D_0 \exp \left(-\frac{E_m}{k_B T} \right), \text{ with } D_0 = \frac{1}{4} \nu_0 \quad (2.9)$$

E_m describes the diffusion energy (also called terrace mobility energy). This rather simple relationship can be then fitted to the experimental data in order to get the cluster density at the certain temperature and specific deposition rate, or to study the surface diffusion energy and attempt frequency. One of examples for latter can be found in [36], where a system of Ag clusters on a Pt(111) surface was investigated, yielding $E_m = (168 \pm 5)$ meV and $\nu_0 = 7 \cdot 10^{13 \pm 0.3}$ Hz. A similar approach was made by Bott and co-workers [37], who gain comparable results for the surface diffusion energy of $E_m = (260 \pm 10)$ meV and the diffusion frequency of $\nu_0 = 5 \cdot 10^{12 \pm 0.5}$ Hz.

Considering the growth of 2D clusters at low temperatures and with the assumption of mobile single atoms and stationary stable clusters with more than two atoms per cluster, equation (2.8) describes the process of growth during deposition quite precisely. Thus, during deposition the number of dimers increases linearly until their density is of the order of the density of single atoms on the surface. Then the probability that a diffusing atom will find another atom or a stable cluster is the same, so that the increase of the stable clusters is not linear, it flattens out until n_x is saturated. After saturation, each further arriving atom only encounters already formed clusters and only contributes to the growth of the clusters and not to the nucleation of new clusters. Further deposition eventually causes the clusters to coalesce and then a monolayer (ML) is formed.

An example of typical coverage during metal-on-metal growth can be found in the work of Brune et al., where saturation occurs at $\theta = 0.15$ ML, coalescence begins at $\theta = 0.2$ ML and film formation begins at $\theta = 0.5$ ML [34, p.72].

This model has been validated by several experimental measurements and theoretical calculations and has

²Saturation density is defined so that the mean free path of the diffusing adatoms is equal to the mean cluster separation. Then in average every new deposited atom will be directly attached to an existing cluster [34, p.72].

³The critical cluster size is reached when the gathering of one additional atom causes the cluster to become stable.

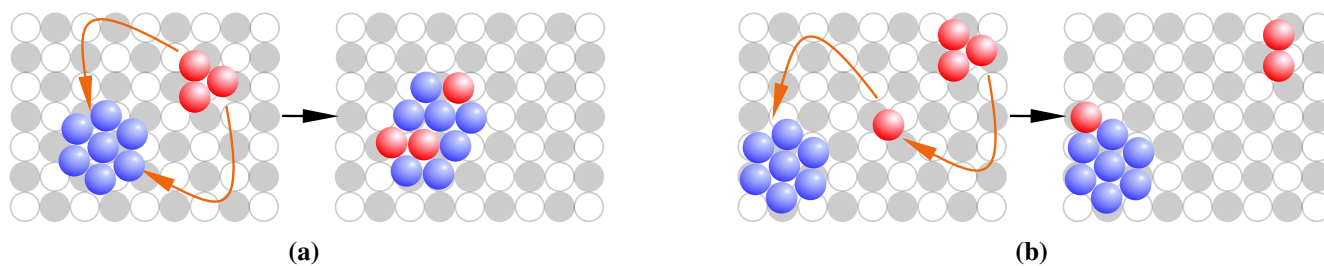


Figure 2.5.: Schematic representation of (a) coalescence: two clusters (colored differently in the image for clarity) merge together due to thermal motion or intergrowth by aggregation of individual atoms and (b) Ostwald ripening: growth of larger clusters due to faster dissociation of atoms from smaller clusters.

significantly contributed to the understanding of cluster and layer formation on surfaces during deposition. However, it is important to remember that this simple image does not take into account surface defects, step edges, or anisotropic surfaces, so in some cases large deviations may occur, for example in the case of a high density of surface defects. In addition, the processes become much more complex when moving from 2D to 3D clusters.

However, if we stay in the above mentioned range, i.e. at low temperatures, well prepared smooth surfaces with few step edges and at moderate deposition rates, this image gives quite a good approximation for the cluster density, which then provides a basis for well defined post deposition growth manipulation.

2.2.2. Post deposition growth

Two mechanisms are mainly responsible for the growth of clusters on a surface in the post deposition process [39]. Coalescence: two clusters come together either by mobility on the surface or by growing together by aggregation to form a new larger cluster, mostly occurring at higher cluster densities. For small cluster densities, where the clusters are well separated from each other, Ostwald ripening [40] is responsible for their growth. As long as the clusters on the surface are not at very low temperatures where all the dynamical processes are frozen, the clusters constantly lose single atoms by dissociation and get new atoms by aggregation. Because dissociation happens faster in small clusters than in large ones, large clusters grow at the expense of small ones. Thus, in order to obtain clusters with relatively narrow size distribution by PVD, the deposition of clusters can be started by very moderate parameters (low flux, short deposition times, low temperatures and small coverage). As described above (see section 2.2.1), the cluster density can then be estimated quite well. However, the size distribution of these clusters is relatively wide. This can be improved to a certain degree in post deposition by subsequently gentle annealing of the sample at higher temperatures. This is exactly where the Ostwald ripening process occurs. ‘The size distribution can be verified between the steps e.g. with STM.

2.3. Experimental techniques

The current chapter encompasses the conceptual principles of experimental techniques such as LEED, STM and UPS, which were utilized within the scope of the present thesis.

2.3.1. Low Energy Electron Diffraction

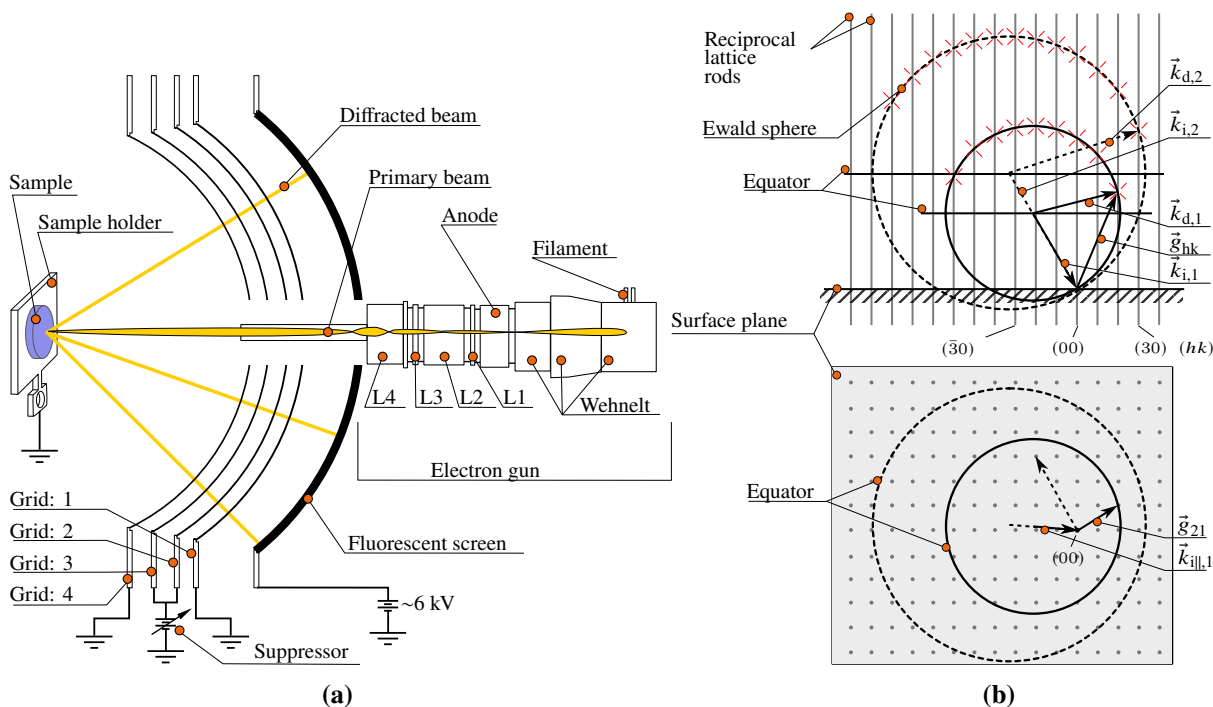


Figure 2.6.: a) Schematic construction of LEED. b) Ewald sphere construction of LEED measurements for two different electron energies $\vec{k}_{i,1}$, $\vec{k}_{i,2}$ in reciprocal space. Top panel: cross-sectional view of the surface. Red crosses indicate diffracted spots on the screen. Bottom panel: top view of the surface, the reciprocal lattice rods point in the direction of the view and therefore appear as dots. All rods enclosed by the equator of the Ewald sphere result in diffracted spots on the fluorescent screen.

LEED is a surface sensitive method which is widely used in surface research. The typical setup consists of an electron gun, a grid system and a luminescent screen. Electrons are emitted from a cathode and accelerated through the anode, passing through an electrical lens system and being focused on the surface of the sample. The diffracted electron beam passes through the grid system and hits the spherical fluorescent screen, which is then recorded by a camera (figure 2.6(a)). The operator usually has an influence on the energy of the electrons (voltage between the cathode (Wehnelt) and anode) and the voltage on the lenses, which set the focus of the electron beam and depend on the energy of the electrons and must be adjusted individually for each device. In addition, the suppression voltage can be applied to the grid system which suppresses the non-elastically scattered electrons.

To understand and visualize the diffracted spots in the reciprocal space of the crystal (which is mapped on the fluorescent screen of the LEED apparatus), the Ewald sphere construction is used, as is common in X-ray diffraction. However, a small modification is necessary because the energy of the electrons is low (about 30 to 300 eV), limiting their penetration depth to a few Å (1×10^{-10} m). As a result, the discrete

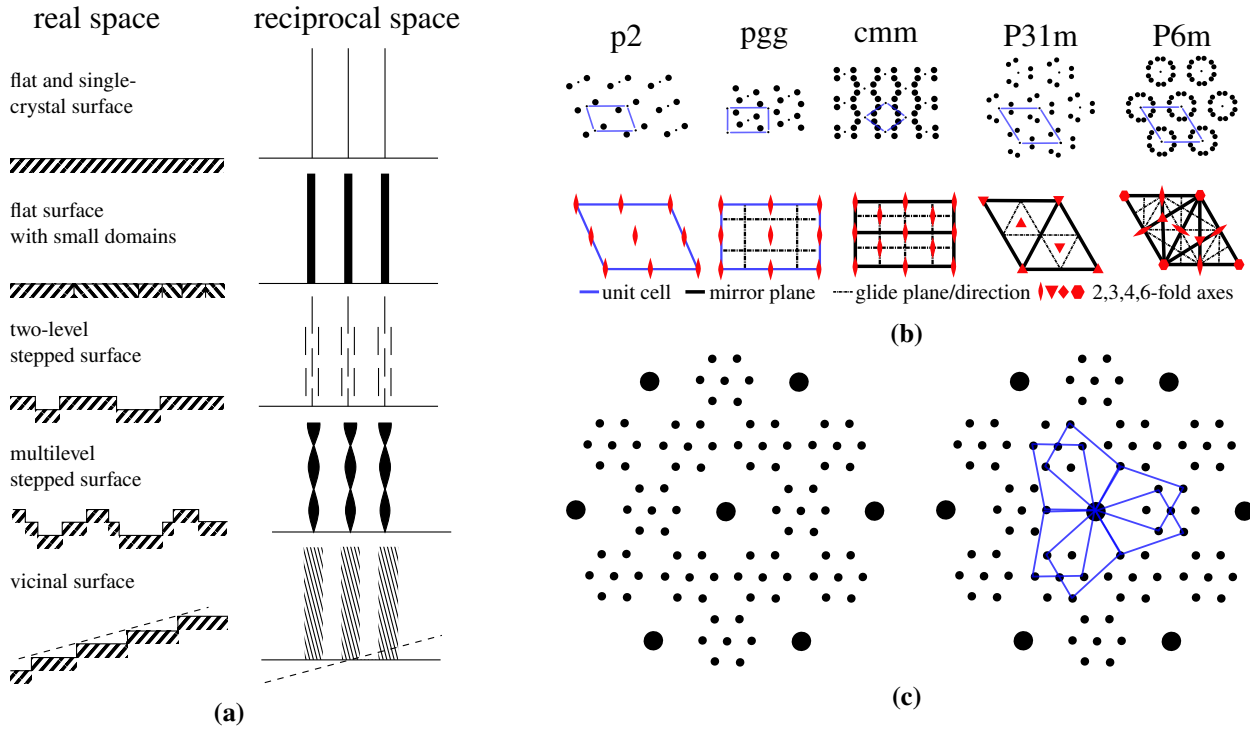


Figure 2.7.: a) Influence of the texture of the surface on the reciprocal space of LEED [41]. b) Top panel: Five examples of the total of 17 two-dimensional lattices with the associated unit cell in blue. The small dots represent the corners or centers of the unit cell. The larger dots can be reconstructed by the respective symmetry operation. Space group designations are also given. E.g. **pmg** stands for **p**erpendicular lattices with **m**irror and **g**lide planes. Based on [42]. b) Bottom panel: Unit cells of the respective symmetry group with corresponding symmetry axis and planes (indicated at the very bottom of the image). Thereby n-fold axes stands for n-times rotation around the corresponding axis. c) Leed pattern for a hexagonal structure. Large dots represent substrate spots. The Right side of the image represents the same pattern as on the left side with the unit cells of different domains denoted in blue [42].

spots in 3D reciprocal space, typical in X-ray diffraction, are represented in LEED as rods perpendicular to the surface of the crystal. As a consequence much more reflexes are allowed.

Figure 2.6(b) shows an example of two different energies of incoming electrons $\vec{k}_{i,1}, \vec{k}_{i,2}$ where \vec{k}_i and \vec{k}_d denote the incoming and diffracted wave vectors of electrons respectively (see upper side of figure 2.6(b)). The reciprocal lattice rods represent the ordered structure of the crystal surface in the reciprocal space. Since we consider here only the elastic diffraction (the inelastically diffracted electrons are suppressed by the suppressor grid), the energy conservation is valid, which means within the diffraction process the energy of the incident electrons is equal to that of the diffracted ones $|\vec{k}_i| = |\vec{k}_d|$. Thus a sphere around the incident electron beam can be constructed, the Ewald sphere. When the Laue condition is satisfied:

$$\vec{k}_d - \vec{k}_i = \vec{g}_{hk} \quad (2.10)$$

constructive interference occurs and a diffracted spot appears on the LEED screen. Here \vec{g} denotes the reciprocal lattice vector:

$$\vec{g}_{hk} = h\vec{a}^* + k\vec{b}^* \quad (2.11)$$

Where \vec{a}^* and \vec{b}^* are the primitive reciprocal translation vectors. The spots visible on the fluorescence screen of the LEED setup correspond to the projection onto the equator plane of the spots originating from the intersection of the Ewald sphere with the reciprocal lattice rods, as shown in figure 2.6(b). When the energy of the electrons is increased, the size of the Ewald sphere also increases and its origin shifts. Hence more reflections are visible on the screen and it appears, that the spots on the screen converge

towards the center [42]. All the above applies to an ideal surface. In reality, the surfaces are often not perfectly smooth, which also has an effect on the LEED image.

Figure 2.7(a) shows some examples of different surface textures and their representation in reciprocal space. This is only the basic idea of the origin of LEED spots. For the interpretation of diffraction patterns, it is important to mention that the symmetry of the surface (be it reconstruction of the top atomic layer of the crystal or the symmetry of the adsorbates/layers) under normal incidence of the electron beam corresponds to the symmetries of the spots on the luminescent screen of the LEED. Due to the low penetration depth of the electrons in the LEED (about 5 to 10 Å), one of the dimensions can be neglected and the 17 space groups in 2D have to be considered [42]. Those 17 space groups can be divided into 5 groups of the basic shapes of the unit cell: Parallelogram lattice (p1, p2), Rectangular lattice (pm, pg, pmm, pmg, pgg), Rhombic (Centered) lattice (cm, cmm), Square lattice (P4, P4g, P4m, P3, P3m1, P31m)⁴ and Hexagonal lattice (P6, P6m). Figure 2.7(b) shows five symmetries, each of which belongs to one of the 5 groups. In addition, if the surface contains different domains, the patterns can be more complex. Figure 2.7(c) shows an example of such a complex LEED pattern.

⁴Sometimes the last three symmetries (P3, P31m, P3m1) are called trigonal lattices.

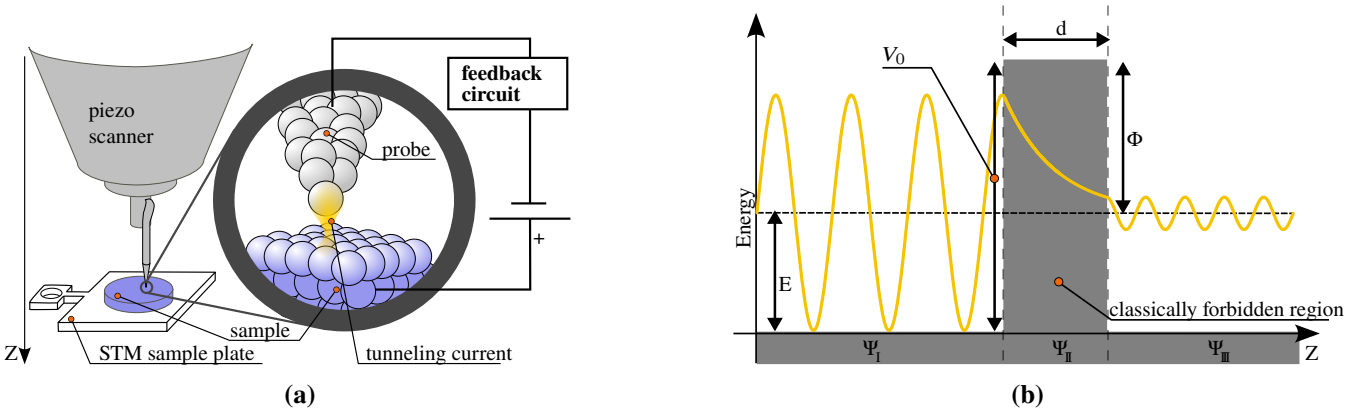


Figure 2.8.: (a) Schematic representation of STM. (b) One-dimensional tunneling effect, with the cathode and anode made of the same material and a non-conducting barrier in between. With a sufficiently thin barrier, the wave function of the electrons can penetrate the barrier and still be found on the other side, without any voltage applied.

2.3.2. Scanning tunneling microscope

STM is a technique which has been developed in the 1980s by Gerd Binnig and Heinrich Rohrer. The discovery and development have been so significant for physics that they were both awarded a Nobel Prize in 1986 which they shared equally with Ernst Ruska for the discovery and development of electron microscopy (1/2 for Ernst Ruska and 1/4 each for Binnig and Rohrer) [43]. In STM measurement, a very sharp tip (also called a probe) is brought very close to a conductive surface (≈ 1 nm) see figure 2.8(a). When a voltage is applied between the tip and the sample, a current flows despite a gap. This quantum mechanical effect is referred to as the tunneling effect. In classical physics, electrons from the tip cannot overcome the non-conducting barrier between the tip and the sample. However, in the quantum mechanical view, where electrons are considered as particles and waves at the same time, electrons in the barrier have non-vanishing probability that decays exponentially. In the very simple picture of a one-dimensional barrier between a tip and the sample of same metal as shown in Figure 2.8(b). To describe the system in quantum mechanics the Schrödinger equation can be used:

$$i\hbar \frac{\partial}{\partial t} \Psi(r, t) = \left(-\frac{\hbar^2}{2m} \Delta + V(r, t) \right) \Psi(r, t) \quad (2.12)$$

If we consider the one-dimensional problem with time independent potential, the time dependence in the wave function can be considered as a separate factor $\Psi(r, t) = \exp(-iEt/\hbar)\Psi(r)$. Accordingly, the Schrödinger equation can be written as:

$$\frac{\hbar^2}{2m} \frac{\partial^2}{\partial z^2} \Psi(z) = [V(z) - E] \Psi(z) \quad (2.13)$$

By inserting the wave functions for each of the three regions shown in Figure 2.8(b) into the Schrödinger equation, we obtain:

$$\Psi(z) = \begin{cases} Ae^{ikz} + Be^{-ikz} & z < 0 \text{ (region I)} \\ Ce^{ikz} + De^{-ikz} & 0 \leq z \leq d \text{ (region II)} \\ Fe^{-ikz} & z > d \text{ (region III)} \end{cases} \quad (2.14)$$

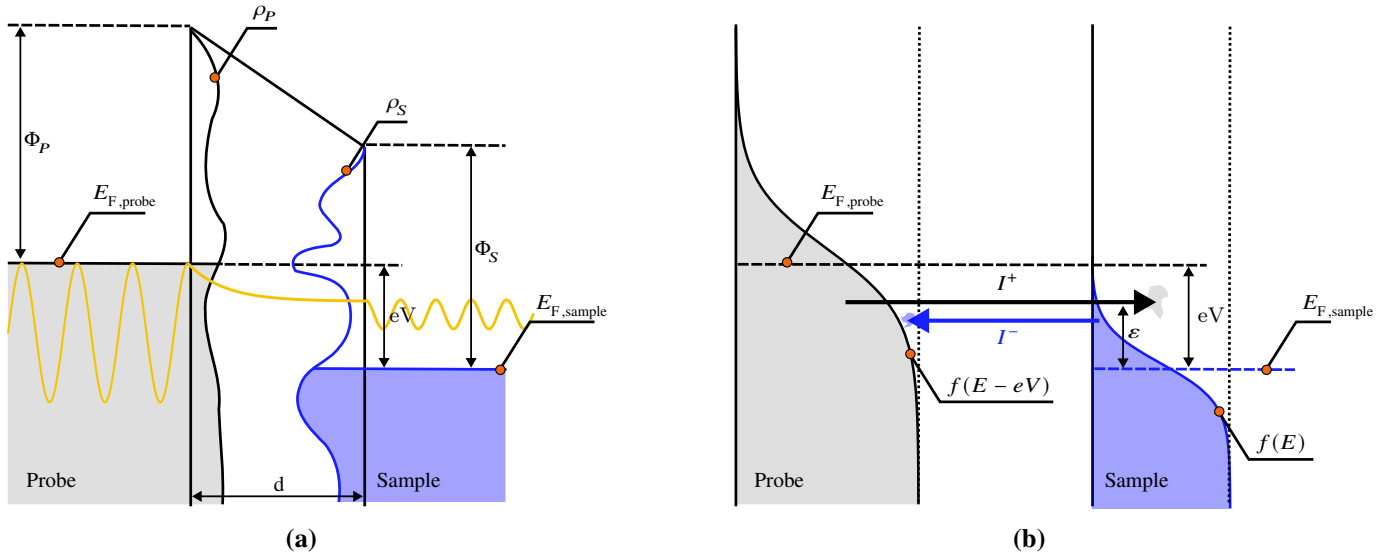


Figure 2.9.: (a) Schematic representation of the tunneling effect with probe and sample made of different materials. A positive voltage is applied to the sample, which lowers the Fermi energy of the sample. The colored areas represent filled electronic states. ρ stands for the density function of electronic states and Φ represents the work function, the energy needed to remove an electron from the material into the vacuum. E_F is the Fermi energy. (b) Effect of finite temperature on the tunneling effect. I^+ and I^- represent the electrons tunneling from the tip into the sample and from the sample into the tip, respectively. $f(E)$ is the Fermi function and ε represents the energy of a particular electron. Both figures are based on [44].

A, B, C, D, F represent the amplitudes of the wave function of an electron in the respective region (I, II, III) and are complex numbers. Considering the continuity condition of the wave function at the transition of regions $I \rightarrow II$ and $II \rightarrow III$ we can solve all these equations and find the solutions for this particular system. Since this exercise is to be found in almost every textbook of quantum mechanics, we will directly write down the important result without proof:

$$T = |F|^2 \propto \exp\left(-\text{const. } d\sqrt{V_0 - E}\right) \quad (2.15)$$

This equation is only valid for the case, where the particle energy is much smaller than the potential barrier. Thereby T is the probability of finding the electron after passing the barrier. We call this the tunneling probability. Thus the tunneling probability decreases exponentially with the thickness of the barrier (distance tip to sample) and the square root of the barrier height. This one dimensional example allows to follow the principle of the quantum mechanical tunneling effect, but it neglects that usually the tip and the sample are not made of the same metal and not only have one electron state with the energy E but rather an electron band structure. Also, no applied voltage between the tip and the sample was considered.

In general, the tip and the sample are made of different materials whose composition consists of the same or different atoms. The electron structure of the tip/sample can be described by the density of states (DOS) $\rho(E)$ and the Fermi energy E_F . The DOS describes how many states are available in a certain energy interval in a physical system (here tip or sample). E_F describes the energy of the highest occupied state in the system. Thus, our system of tip, sample and potential barrier at an applied positive voltage to the sample can be considered as represented in figure 2.9(a). Such a representation and quantum mechanical description of a system of two different metals and an insulating material in between was

made by John Bardeen⁵ in 1960 [45]. As his description happened 20 years before the invention of STM, Bardeen in his paper speaks of two metals and a thin insulating oxide layer. Later many other theoretical physicists, including Tersoff and Hamann, adopted his work for the description of processes in STM. However Bardeen considered the tunnel effect as a many particle system of electrons. Since the description of a real many particle system is quite challenging as they are usually dynamic and also coupled, his theory is based on several assumptions[46]:

- 1) tunneling is weak so that a first-order approximation is valid
- 2) probe and sample states are nearly orthogonal
- 3) electron-electron interactions are ignored
- 4) tunneling has no effect on the occupation probability of probe and sample states
- 5) the probe and sample are in electrochemical equilibrium

With these assumptions and with the help of time-dependent perturbation theory and Fermi's Golden Rule[47], the tunneling current in the low-temperature limit can be represented as follows:

$$I = \frac{4\pi e}{\hbar} \sum_{i,f} |M_{i,f}|^2 \delta(E_{S,f} - E_{P,i}) = \frac{4\pi e}{\hbar} \int_{E_{f,\text{sample}}}^{E_{f,\text{probe}}} \rho_P(\varepsilon) \rho_S(\varepsilon) |M(\varepsilon)|^2 d\varepsilon \quad (2.16)$$

Here, δ represents the Dirac delta function and ensures that the energy conservation is valid, since only the transitions where the initial energy E_i is equal to the final energy E_f are allowed.⁶ $M_{i,f}$ is a so-called tunneling matrix element⁷.

$$M_{i,f} = \frac{\hbar^2}{2m} \int_{S_{P,S}} \left(\Psi_{P,i} \nabla \Psi_{S,f}^* - \Psi_{S,f}^* \nabla \Psi_{P,i} \right) \cdot d\vec{S} \quad (2.17)$$

The integration is performed over the separation surface $S_{P,S}$ within the barrier. P, S, i, f stand for Probe, Sample, initial state and final state respectively. The equation (2.16) applies to systems at very low temperatures. The Fermi energy, as shown in Figure 2.9(a), has a sharp edge. In reality, the Fermi edge is softened and can be represented by the Fermi function as follows:

$$f(E - E_F) = \frac{1}{1 + \exp\left(\frac{E - E_F}{k_B T}\right)} \quad (2.18)$$

This means that in our example of a tip, sample and gap in between, with a positive voltage on the sample, there is not only a transfer from the tip into the sample, but also a transfer from the sample into the tip

⁵John Bardeen is famous for his work in the field of semiconductors and was the first to be awarded two Nobel Prizes in Physics. One of his most famous works is the BCS theory (Bardeen, Cooper, and Schrieffer theory) where he and colleagues theoretically described superconductivity.

⁶The transition from discrete energy levels to the continuous density of states is given here without going into details, the interested reader should be referred to the book of Voigtländer [44], where he describes this problem on several pages.

⁷For simplicity the $\Psi_{P,i}(\vec{r})$ is represented as $\Psi_{P,i}$. Also the matrix element $M(\varepsilon)$ is the same as $M_{i,f}$ but with $\Psi_{P,i}(\vec{r}) \rightarrow \Psi_{P,i}(\vec{r}, \varepsilon)$

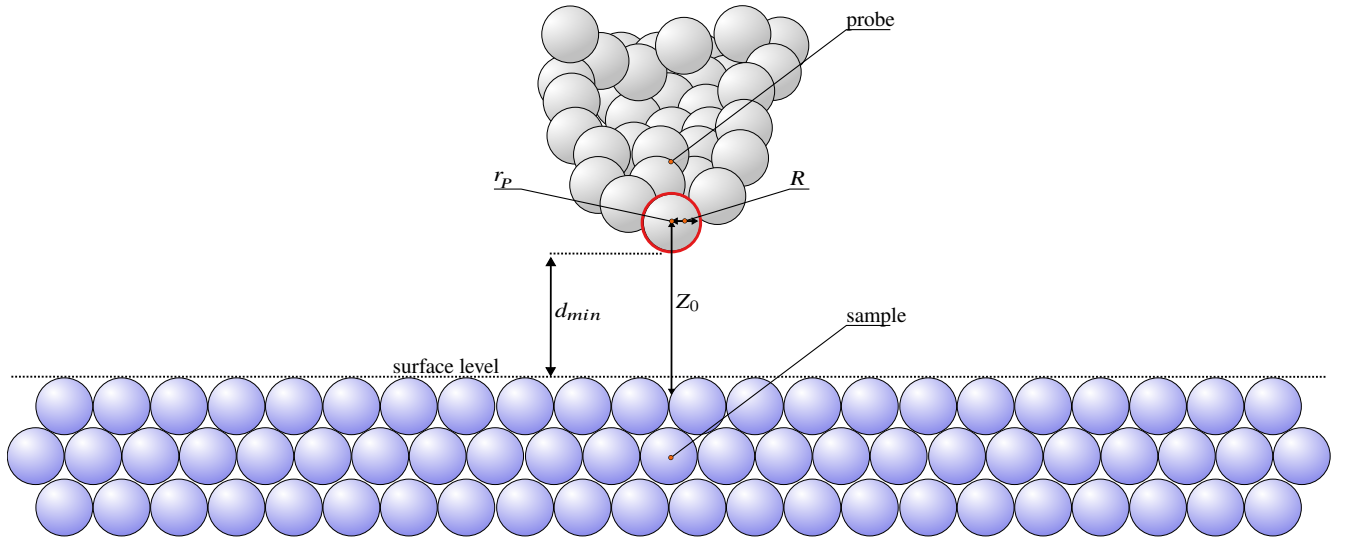


Figure 2.10.: Schematic representation of the Tersoff-Hamann theory.

(see figure 2.9(b)). This leads to a net current:

$$I = \frac{4\pi e}{\hbar} \int_{-\infty}^{\infty} \{f(\varepsilon - eV) - f(\varepsilon)\} \rho_p(\varepsilon - eV) \rho_s(\varepsilon) |M(\varepsilon)|^2 d\varepsilon \quad (2.19)$$

To calculate the current with Bardeen's equation, the wave function of the tip (i.e. its structure) is needed, which however is not known in general. Therefore, Tersoff and Hamann showed in 1983 [48] that under the assumption of very small tunneling voltages, the wave function of the tip can be approximated by a spherical wave function.

This allows the tunneling current to be approximated by the local density of states of the sample at E_F and at the position of the center of the tip r_p [44] :

$$I \propto \sum_n |\Psi_n(\vec{r}_p)|^2 \delta(E_F - E_n) \equiv \rho_s(E_F, \vec{r}_p) \quad (2.20)$$

Figure 2.10 shows the schematic representation of the Tersoff and Hamann approximation of the tip. The Tersoff-Hamann approximation connects STM images in a comprehensible way to the mapping of the local density of states of the sample only for very small bias voltages. For the description of semiconductors, for example, the Tersoff-Hamann approximation is not suitable because in this case bias voltages of more than 2V are needed [49].

For a more realistic description, a better approximation of the real tip is needed. This can be done by different models, such as modeling the tip as a single atom adsorbed on the metal surface and simulating the metal surface by applying the jellium model [50]. Or by simulation of the tip as a tungsten cluster with 10 atoms [51]. Moreover, it is worthwhile to mention that there are several other approaches to approximate the tunneling effect, such as Chen's approximation, Green's function formalism, Scattering theory and Hückel approximation [52].

STM has a limitation when it comes to measuring particles on the surface with sizes in the range of about 0.5 nm. As illustrated in Figure 2.11, when the height does not vary significantly in the lateral direction (as observed in the left part of the resulting height profile in Figure 2.11), tracking the surface

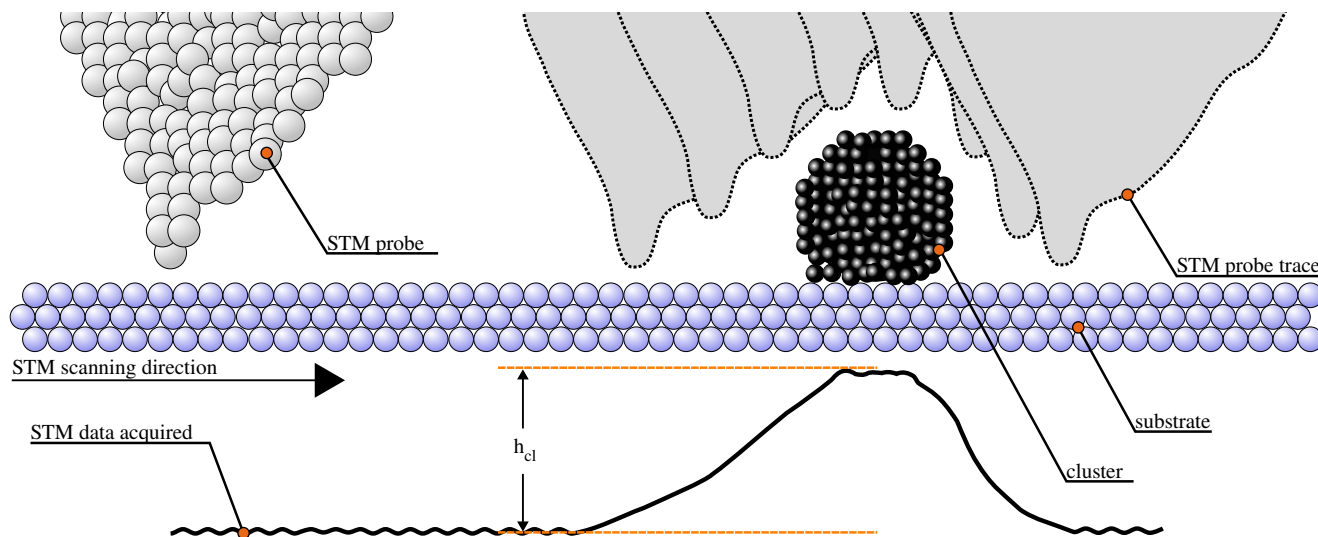


Figure 2.11.: Lateral broadening caused by the STM probe. Top: Schematic representation of the STM data acquisition of a surface with a large cluster. Bottom: Resulting height profile.

is reliable. However, when the height of the particle or cluster becomes sufficiently large that the shape of the probe tip starts to influence the measurement, the lateral shape of the cluster may become distorted (see right part of the Figure 2.11). Nonetheless, the height of the cluster (h_{cl}) remains preserved.

2.3.3. Photoemission Spectroscopy

In 1887 Heinrich Hertz [53] and Wilhelm Hallwachs [54] conducted the first experiments on the photoemission effect. They observed that when shining ultra violet light on a negatively charged insulated metal plate, the plate can be discharged. In contrast to a positively charged metal plate, where the discharge does not take place. However, this effect was not understood at that time. It was not until 1905 that Albert Einstein succeeded in proposing the revolutionary photoelectric equation:

$$E_{kin}^{max} = h\nu - \Phi_0 \quad (2.21)$$

where the photon energy $h\nu$ is directly related to the maximum kinetic energy of the emitted electrons E_{kin}^{max} and the characteristic material constant Φ_0 , also known as the work function. It took several years to obtain a clear experimental proof of the photoelectric effect and Einstein was awarded the Nobel Prize for his theoretical achievement in 1921 [55]. Basically, the photoelectric effect describes the emission of electrons from a solid induced by light (photons). The decisive factor is the energy of the photons and not their intensity. If at a fixed energy of the photons no electrons are emitted from a solid, the increase of the intensity of the light does not lead to a photoelectric effect, however the change of the energy does. Photoemission spectroscopy (PES) is based on the photoelectric effect and gives insight into the electronic structure of solids and molecules. Figure 2.12(a) shows a typical setup of a photoemission spectrometer. The light source is either a discharge lamp, an x-ray tube or a synchrotron radiation source [56]. Typically, the light is monochromatized before it is exposed to the sample, causing electrons to be released from the sample. The electrons are then usually collected in a specific spatial direction. They are guided through electrostatic lenses and pass through the hemisphere energy analyzer, where they can be dispersed by

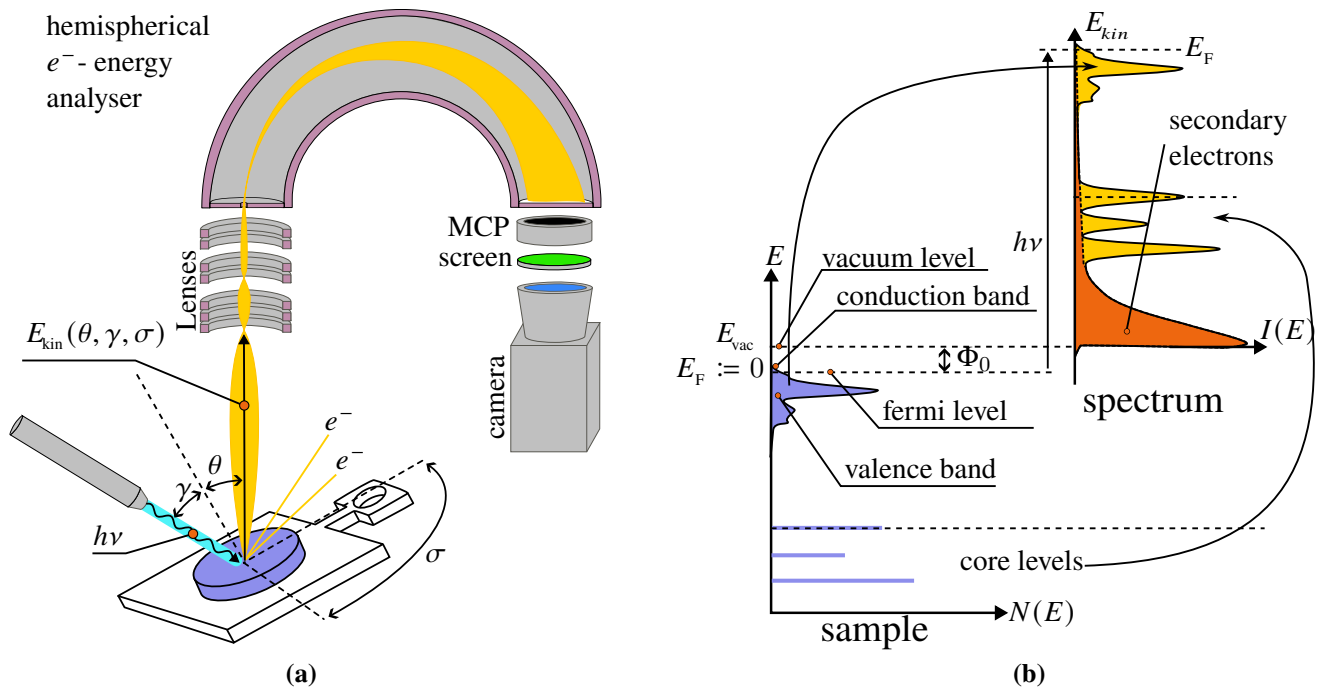


Figure 2.12.: (a) Typical setup for PES. (b) Schematic view of the photoemission process. Electrons with kinetic energy E_{kin} can escape into the vacuum by absorbing photons with energy $h\nu$, as long as they can overcome the work function Φ_0 , see equation (2.22). The intensity of the spectrum $I(E)$ corresponds, in the first approximation, to the density of electron states $N(E)$ in the sample. The Fermi level E_F lies between the valence band and the conduction band. Secondary electron cascades contribution in the spectrum results from the electron-electron scattering in the sample.

energy or momentum. Next the electrons hit multichannel plates (MCP)⁸, then the luminous screen and are finally recorded by a camera. The resulting spectrum is then processed in the computer. Thereby, the kinetic energy of the electrons is measured. Figure 2.12(b) shows the schematic structure of a spectrum obtained during the photoemission spectroscopy experiment. The electron received its energy, shown in the spectrum, from the photon, then overcame the work function and was detected. So by subtracting the work function⁹ and the kinetic energy of the electron from the known photon energy, a residual energy remains which is called binding energy¹⁰ E_B .

$$E_B = h\nu - E_{\text{kin}} - \Phi_0 \quad (2.22)$$

In the spectrum shown in Figure 2.12(b) is one more feature visible, the contribution of so called secondary electrons. The secondary electrons are the photoelectrons that scatter inelastically before leaving the solids into the vacuum.

In reality, the process of photoelectron emission is much more complex than described above. However, this rather simple single-particle picture helps to understand the main processes in PES. The details of a spectrum such as the shape of the core level peaks or the details in the band structure on the meV scale cannot be explained by the single-particle picture. Therefore, the sample must be considered as a many-body system. In the literature often a quantum mechanical approach is used, where Fermi's

⁸Device for multiplying the signal of electrons by emitting secondary electrons in cascades

⁹The work function can be determined experimentally by measuring the whole energy range emitted from the solid ($E_{\text{kin}}^{\text{max}}$) and applying equation (2.21)

¹⁰In the literature, the spectra are usually presented as a function of the binding energy. Thereby the reference energy in solids is taken as E_F and in molecules as E_{vac} .

Golden Rule and the perturbation theory are applied. Thereby it is assumed, that an electron is removed from the N-particle system, but the relaxation of the (N-1) system of particles has no influence on the photoelectron (sudden approximation¹¹).

This yields a current of photoelectrons $J_{\vec{k}}(h\nu)$, which is composed of the individual contributions from each photoelectron with the wave vector \vec{k} :

$$J_{\vec{k}}(h\nu) = \frac{2\pi}{h} \sum_f \underbrace{|\langle \Psi_{\vec{k},s} | H_{PE} | \Psi_i \rangle|^2}_{:=\Delta_{if}} \underbrace{\sum_s |\langle \Psi_s(N-1) | c_{\vec{k}} | \Psi_i(N) \rangle|^2}_{:=A_{\vec{k}}^<(h\nu)} \delta(h\nu - \varepsilon_s) \quad (2.23)$$

With the photoelectron matrix element Δ_{if} , where H_{PE} represents the so called photoemission perturbation operator:

$$H_{PE} = \frac{e}{2m_e c} (\vec{A} \cdot \hat{p} + \hat{p} \cdot \vec{A}) + \frac{e^2}{2m_e c^2} A^2 \quad (2.24)$$

With the electromagnetic field \vec{A} and momentum operator $\hat{p} = i\hbar\nabla$. $A_{\vec{k}}^<(h\nu)$ represents the one-electron spectral function. $c_{\vec{k}}$ is so called creation operator and is responsible for the creation of a photoelectron:

$$|\Psi_{\vec{k},s}(N)\rangle = c_{\vec{k}}^\dagger |\Psi_s(N-1)\rangle \quad (2.25)$$

The index i stands for the initial state and $\Psi_{\vec{k},s}$ describes the final state of the photoelectron. The Index s denotes a complete set of quantum numbers and describes all possible excitations in the final state (photon, plasmon, electron-hole pairs and multiple excitations). Basically $A_{\vec{k}}^<(h\nu)$ describes the probability to remove one electron from the system with the wave vector \vec{k} and energy ε [58, 59]. The equation (2.23) describes a general case. To calculate J , however, all excited states of the (N-1) system must be known. This is impractical and computationally expensive. Besides, the evaluation of equation (2.23) is mostly done with bulk Bloch states, the surface is not considered. This can be compensated if this approach is considered as the first step in the so-called three-step model. Although this leads to the need for further theoretical treatment [59].

Fortunately, $A_{\vec{k}}^<(h\nu)$ can be put in relation with a one-particle Green's function, which allows the calculation without the knowledge of the whole system. With this approach, for example, the explanation of the asymmetric spectral lines of the core level of metals is possible (the Mahan–Doniach–Šunjić line shape)[60–62].

¹¹Which is justified for the energy of photons above a few tens of eV [57].

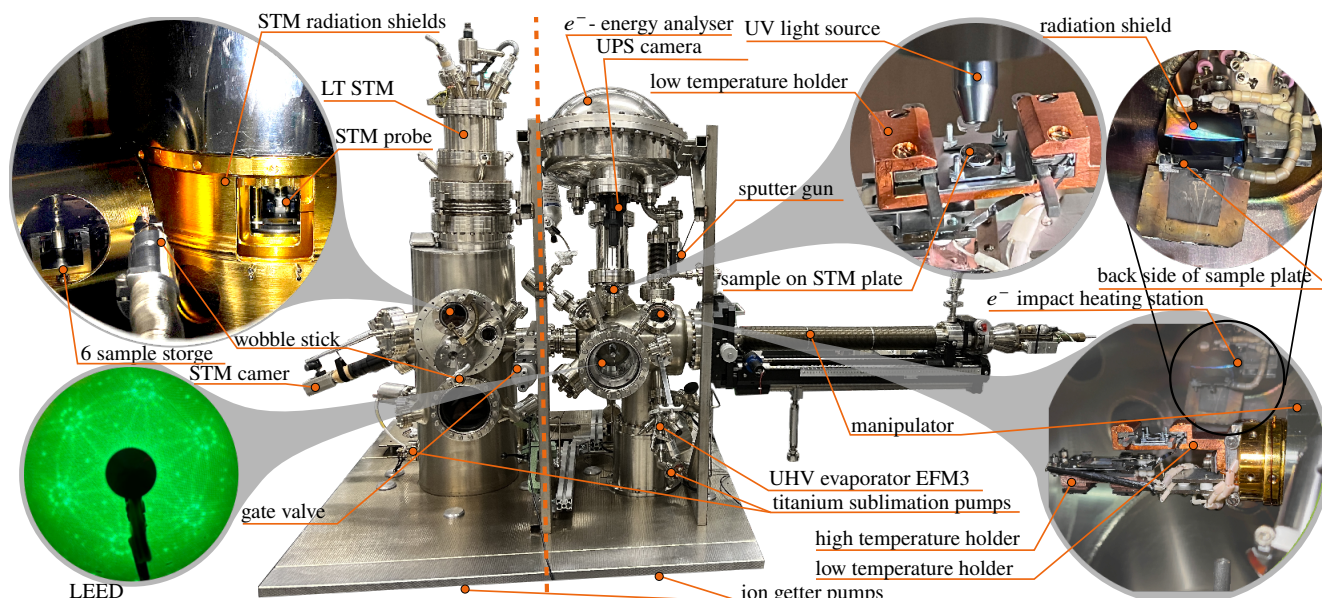


Figure 2.13.: Photo of the UHV surface-science facility. The equipment in the background has been removed for clarity. The vertical dashed line illustrates the separation by means of a gate valve of the two UHV chambers. An ion getter pump is flanged to the bottom of the bench for each chamber. In total, the facility has 4 turbo molecular pumps. One is flanged to the right chamber on the back side under the bench, the second is flanged to the monochromator of the UV source and the other two provide differential pumping of the discharge chamber of the UV source and are also placed on the back side.

2.4. Experimental setup

The experimental setup consists of two main chambers in UHV. In the first chamber the samples are prepared and measured with LEED and UPS. In the second chamber STM measurements are performed and there is a carousel-like sample storage system that can hold up to 6 samples at a time. In order to keep the sample environment as free of contamination as possible, because during sample preparation or UPS measurement the base pressure can deteriorate for a short period of time by one to two orders of magnitude, the second chamber is separated from the first chamber with a gate valve and only STM is performed on samples in the second chamber.

The base pressure is kept below 1×10^{-10} mbar. This is achieved by pumping the entire facility down by turbo molecular pumps to a pressure of about 5×10^{-8} mbar and then baking the entire apparatus at temperatures between 100 and 120 °C for several days. After the base pressure is reached, the maintenance of UHV is ensured by the titanium sublimation pumps and ion getter pumps. Especially during the STM measurement the turbo molecular pumps must be shut down, otherwise the vibration will disturb the measurement.

The cryogenic manipulator with 4 axes (x,y,z and rotation axis θ) allows the transfer between the chambers and the handling during the preparation or measurements (see figure 2.13). The preparation of the samples is performed in the manipulator. There the samples can be heated in a “high temperature” holder up to 600 °C by resistance heating, but the “low temperature” holder must be kept below 150 °C, otherwise there is a high risk that the temperature sensor on the “low temperature” holder is damaged¹². For preparation at even higher temperatures, the samples must be placed in a separate holder, where they can be heated with the help of electron impact heating to over 1000 °C. A more detailed description of

¹²The cooling is achieved by the flow of nitrogen gas through the cryogenic pipes inside the manipulator. Between the “low temperature” holder and the cryostat a monocrystalline sapphire plate is inserted. This insulates the “low temperature” holder electrically from the manipulator while maintaining high heat conductance.

exactly this heating station is presented in the PhD thesis of Wolter [63].

For the cleaning of crystals (samples) an argon ion sputter gun is used. Argon 6.0 is injected into the sputter gun, which leads to the pressure in the chamber raising to about 1×10^{-6} mbar to 1×10^{-7} mbar. By applying a high voltage, the argon ions within the sputter gun are accelerated and then directed towards the surface of the sample. The ions collide with the surface and disintegrate (sputter) the upper layers of the crystal, effectively cleaning it in the process.

3. Samples

The following three subchapters detail the primary substrate used ($\text{Al}_2\text{O}_3||\text{Ni}_3\text{Al}$) and two adsorbate materials (C_{60} and Bi).

3.1. Oxide Layer on $\text{Ni}_3\text{Al}(111)$ crystal

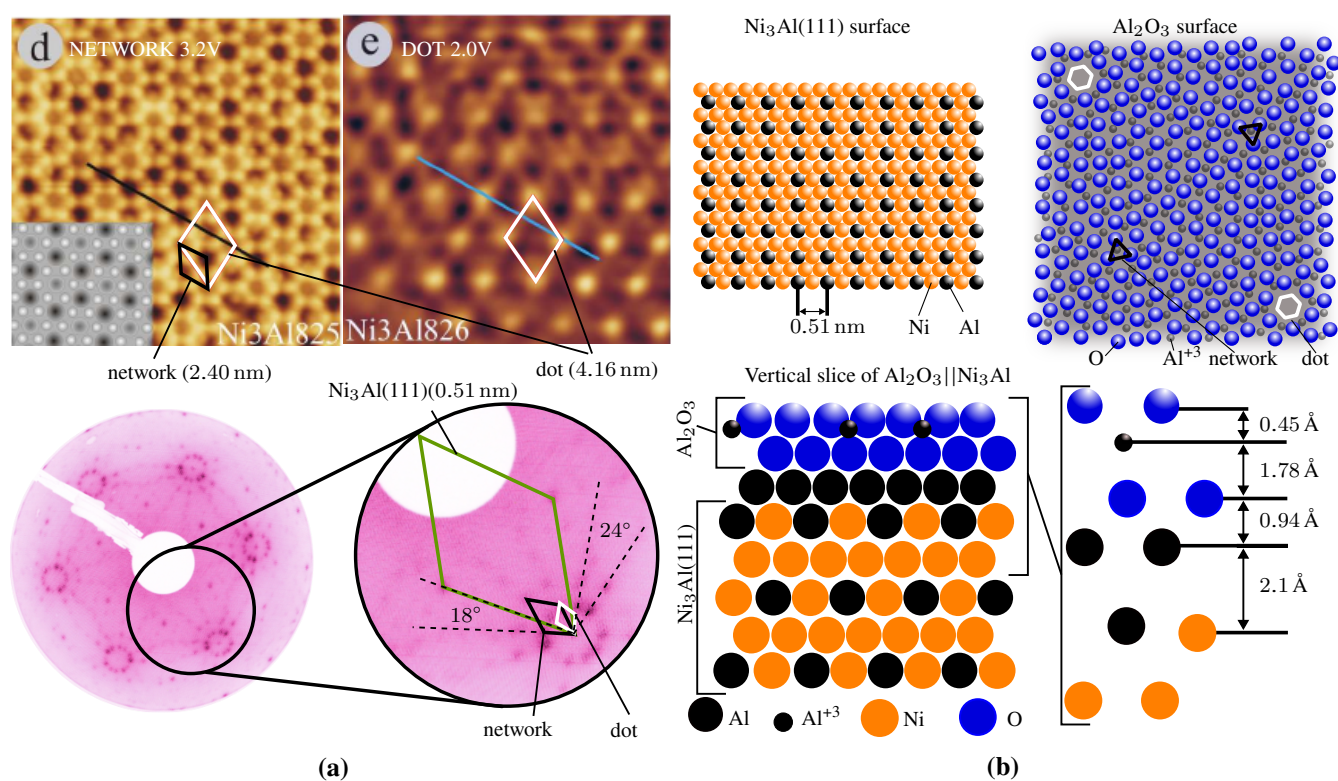


Figure 3.1.: (a) Top: STM images of network and dot structure of $\text{Al}_2\text{O}_3||\text{Ni}_3\text{Al}$, reprinted with minor changes from [64]. (a) Bottom: LEED images of $\text{Al}_2\text{O}_3||\text{Ni}_3\text{Al}$ surface @93 eV. The unit cell of $\text{Al}_2\text{O}_3||\text{Ni}_3\text{Al}$ is marked with green lines, the unit cell of the network structure with blue lines and the unit cell of the dot structure with white lines. Since the LEED pattern is a reciprocal representation of the real space, the unit cell in STM measurement is reciprocal to the unit cell in the LEED image. (b) Top left: Model of the surface of $\text{Ni}_3\text{Al}(111)$ based on [65]. (b) Top right: Model of $\text{Al}_2\text{O}_3||\text{Ni}_3\text{Al}$ based on [66]. White hexagons represent the dot structure, black triangles the network structure. (b) Bottom: Vertical slice of the model of $\text{Al}_2\text{O}_3||\text{Ni}_3\text{Al}$ proposed by [67]. Vertical layer spacing are taken from [66].

For the support of C_{60} molecules and Bi metal clusters, an ultra thin aluminum oxide (Al_2O_3) layer on the surface of $\text{Ni}_3\text{Al}(111)$ was chosen. Long range superstructure is formed only after a special preparation recipe which was developed in the group of Conrad Becker¹. The formation and quality of the oxides layer superstructure can be verified, up to a certain degree, by LEED (see Figure 3.1).

¹ORCID: 0000-0002-7035-6083

The unit cell of the Ni₃Al(111) surface is 0.51 nm in length, as stated in the work of Degen [64]. Additionally, Degen's STM measurements reveal two distinct structures on the Al₂O₃ surface: by adjusting the STM to a gap voltage of 3.2 V, the so-called network structure with a lattice constant of 2.35 nm becomes visible. By reducing the gap voltage to 2 V, the dot structure emerges, characterized by a lattice constant of 4.16 nm. This latter structure is likely the true superstructure of Al₂O₃, exhibiting a $\sqrt{67} \times \sqrt{67}R47.784^\circ$ relationship to the Ni₃Al(111) substrate lattice, as proposed by Degen [64].

In the LEED image, two rings consisting of 12 spots each are visible around the Ni₃Al(111) diffraction spot. The larger outer ring corresponds to the network structure, while the inner ring represents the dot structure. These 12 spots originate from two hexagonal rotation domains within the Al₂O₃ film, with an angle of 24° between them (refer to the enlarged section of the LEED image in Figure 3.1(a)). The 18° angle shown in the same figure, represents the angle between the substrate and the network structure [64].

Schmidt et al. [66] proposed a plausible explanation for the appearance of the dot and network structures by combining STM observations with density functional theory (DFT) calculations. They suggested that holes form (dot structure) on the surface of the oxide layer, extending down to the underlying metal surface (upper right corner of Figure 3.1(b)), serving as templates for nucleation. However, this mechanism occurs only for metals that weakly react with oxygen, such as Pb. For other metals like Fe, the absorption energy in the hole is higher, creating a barrier that impedes nucleation in an ordered manner.

For completeness, Figure 3.1(b) also includes the structure of the Ni₃Al(111) surface (based on Rosenhahn et al. [65]) and a vertical cross-section of the Ni₃Al(111) and Al₂O₃ layer system (based on Schmid et al. [66]).

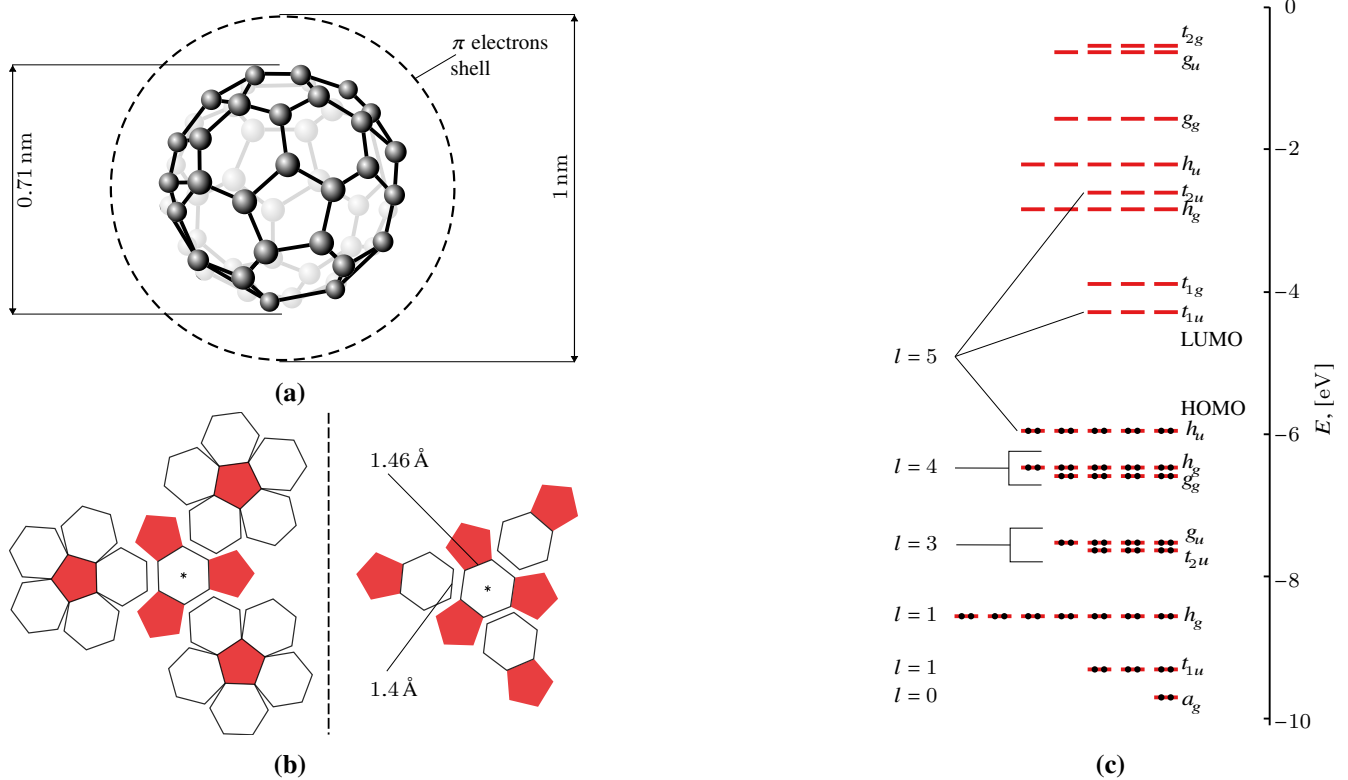


Figure 3.2.: (a) Representation of the cage of the C₆₀ molecule with carbon atoms located at the vertices of pentagons and hexagons and the region of π electrons. Based on the work of Mineyuki Arikawa [68]. (b) Geometric structure of the C₆₀ molecule with 20 hexagons (white) and 12 pentagons (red). For better visibility, the tree-dimensional truncated icosahedron is cut along a random path so that two groups form two halves of the structure (separated by the dashed line). Two hexagons marked with an asterisk represent two parallel faces on an imaginary axis in tree-dimensional space. (c) Energy levels of the free C₆₀ molecule, calculated with the Hubbard model [69].

3.2. Fullerene C₆₀

The discovery of C₆₀ took place in 1985 in the Chemistry Department of Rice University in Houston, Texas in the USA in a collaboration group of U.S. and U.K. researchers. The discovery was so important for the world of chemistry and physics that its discoverers Curl, Kroto and Smalley were awarded the Nobel Prize in Chemistry in 1996. The name Buckminsterfullerene (often abbreviated to fullerene or buckyballs) was chosen in reference to American architect Richard Buckminster Fuller's Biosphere building in Canada, Montreal, which provided the first clue to the molecule's structure [70].

The Fullerene molecule is composed of 60 carbon atoms in a very stable spherical configuration and has no dangling bonds like any other complex carbon molecule (refer to Figure 3.2(a)). The valence electrons of each carbon atom are in a sp^2 hybridized state and three of them form stable σ bonds between neighboring atoms. The fourth valence electron is called the π electron and it is located in the p orbital, which is much more spread out around the C₆₀ molecule than the σ electrons [69].

The geometric structure of C₆₀ has been described by Kroto, Smalley and their colleagues as "a truncated icosahedron, a polygon with 60 vertices and 32 faces, of which 12 are pentagonal and 20 are hexagonal" [71]. There are two different lengths of bonds between carbon atoms: the bond between two hexagons is about 1.4 Å and between a hexagon and a pentagon about 1.46 Å, therefore the shape of icosahedron of C₆₀ molecule is irregular [72] (see Figure 3.2(b)).

The energy levels of C₆₀ calculated using the Hubbard model in the mean-field approximation [69] are shown in Figure 3.2(c).

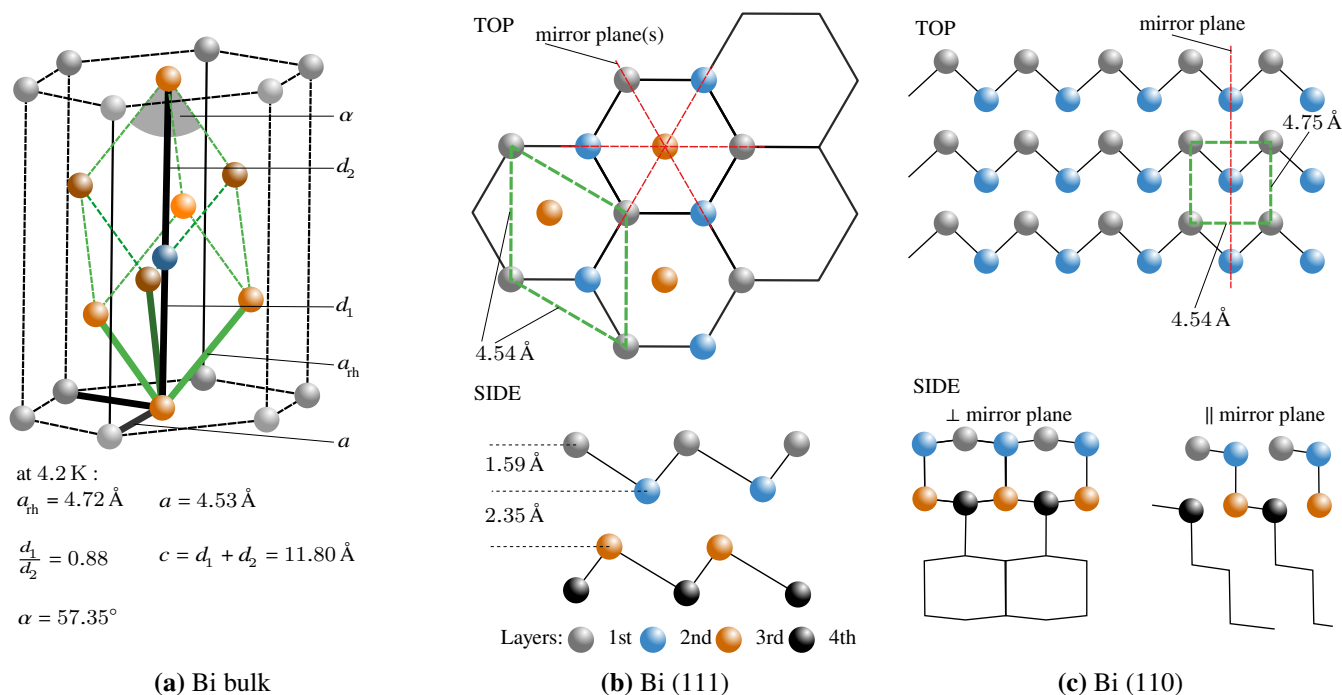


Figure 3.3.: (a) Crystal lattice structure of the bulk of Bi. The rhombohedral structure is indicated by primitive vectors as solid green lines. Hexagonal lattice vectors are indicated by solid black lines. Based on the work of Hofmann [73] (b) Top: Surface of Bi(111). (b) Bottom: Side view of the surface of Bi(111) - virtual slice through one of the mirror planes. Based on the work of Mönig et. al. [74] (c) Top: Surface of Bi(110). (c) Bottom: Side views of the slice perpendicular to the mirror plane (left) and parallel to the mirror plane (right). Based on the work of Sun and coworkers [75].

3.3. Bismuth

Bismuth (Bi) is a heavy metal with atomic number 83. Unlike its Periodic Table neighbors such as Thallium, Lead and Polonium, it is not toxic and almost not radioactive, the half life time of ^{209}Bi is $(1.9 \pm 0.2) \times 10^{19} \text{ yr}$ [76]².

Bismuth's non-toxicity has a huge potential in medicine, for example, its compounds are already used as gastroprotective agents and in the treatment of a *Helicobacter pylori* infection [78]. Bi also has potential to be an excellent antimicrobial [79, 80], anti-leishmanial [81] and anticancer agent [82]. Besides its medical use, Bi could be a good substitute for the very toxic Pb in the perovskite photovoltaic cells [83] or in chalcogenides-based solar cells [84]. Also from a chemical point of view, Bi is a very promising candidate for new discoveries. Since it has a wide range of oxidation states in compounds from -3 to +5 and the ability to form compounds with a wide range of elements and complexes [85], allowing new discoveries for example in catalysis [86].

The crystal structure of Bi is rhombohedral with equal lattice vectors a_{rh} , denoted by solid green lines in Figure 3.3(a). The angle between the primitive vectors is denoted by α . An example of lattice parameter values at 4.2 K [73] is given in Figure 3.3(a). In the same figure the hexagonal vectors a and c are shown. The reason for this notation and the relation to the rhombohedral primitive lattice vectors can be found in the work of Hofmann [73].

²Just for comparison: the age of the universe is approximated to $(13.801 \pm 0.024) \times 10^{12} \text{ yr}$ [77]

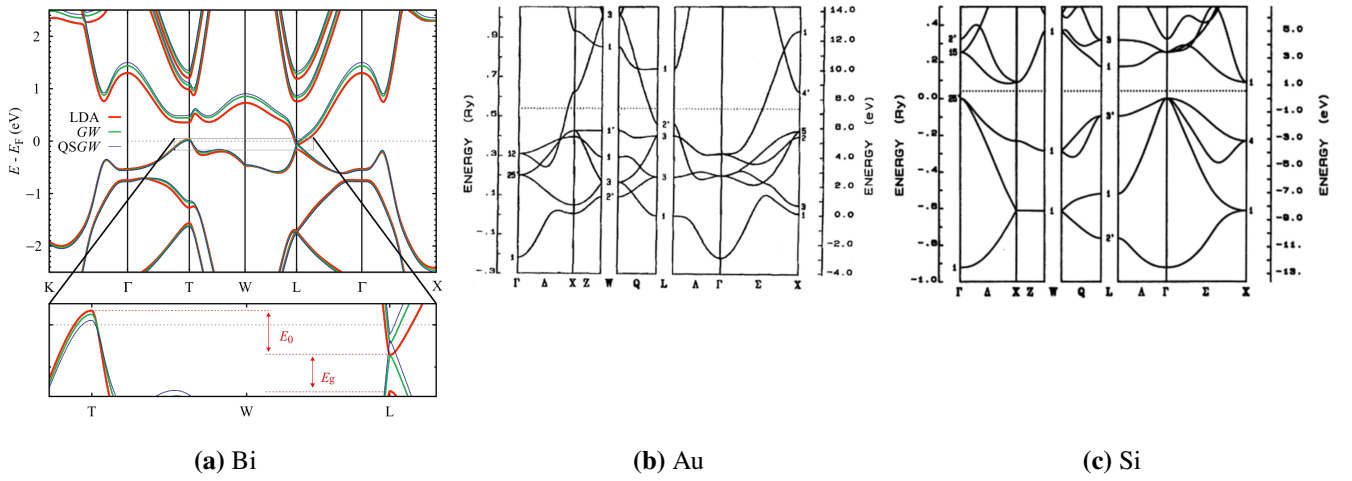


Figure 3.4.: (a) Electronic band structure of Bi theoretical calculations with 3 different approximations of DFT: local density approximation (LDA), generalized gradient approximation (GGA) and quasi-single particle self-consistent GW (QSGW) approximation, where GW stands for the single-particle Green's function (G) and the screened Coulomb interaction (W) [88]. The enlarged portion of the figure shows direct (E_g) and indirect (E_0) band gaps. (b) Electronic band structure of Au and (c) of Si calculated with the tight-binding approximation [89].

In Figures 3.3(b) and 3.3(c) the schematics of the surface of Bi(111) and Bi(110) are given.

Because of its very low free electron density of about $3 \times 10^{17} \text{ cm}^{-3}$ [73], Bi is classified as a semimetal³. This can also be seen in the band structure of Bi, where so-called direct (E_g) and indirect (E_0) band gaps are formed (see Figure 3.4(a)) in comparison to classical metals such as Au (Figure 3.4(b)) where no gap is formed or a typical semiconductor as silicon (Figure 3.4(c)) where a gap is clearly seen.

³In comparison, the free electron density of Au is about $5.9 \times 10^{22} \text{ cm}^{-3}$ [87]

4. Results

In this chapter the results of the UPS and STM measurements are presented and discussed.

In the first part, we discuss the binding of C_{60} molecules to different surfaces (gold, silver, aluminum oxide layer) and the effect of the surface on the HOMO level of C_{60} . Additionally the change of the binding energy of the C_{60} molecules on the surface of $Al_2O_3||Ni_3Al$ in dependence of the annealing temperature is presented.

In the second part of the chapter, the studies of the self-organized bismuth clusters on the surface of $Al_2O_3||Ni_3Al$ as a function of the annealing temperature are discussed. Furthermore, an electrostatic model is provided for describing the observed effects.

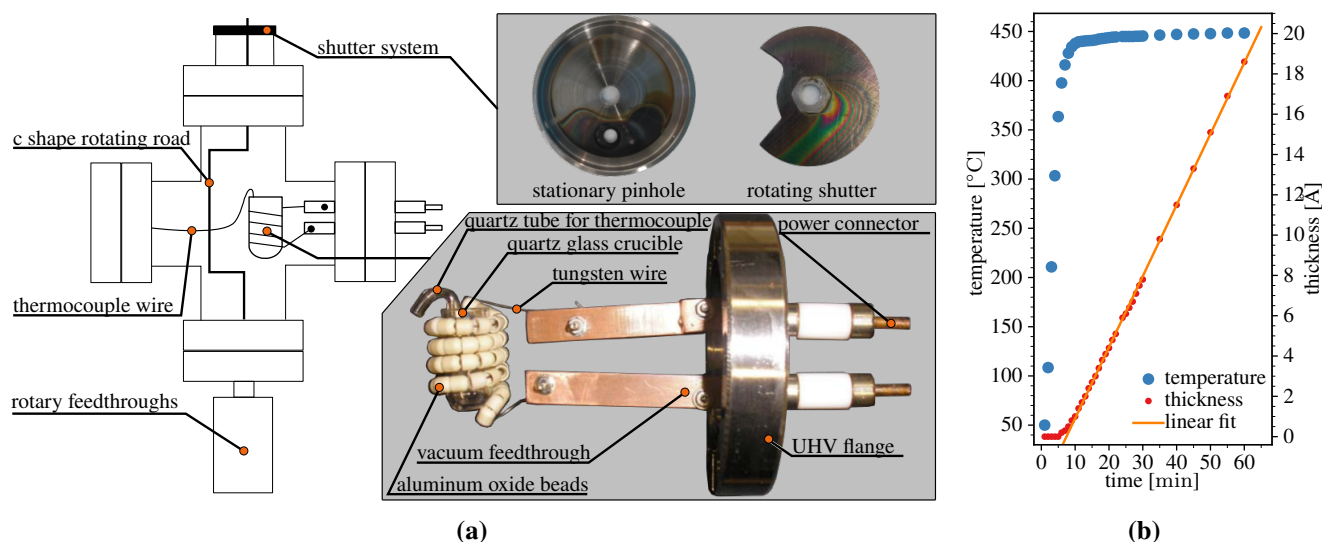


Figure 4.1.: (a) Schematic view of the C₆₀ evaporator unit. Photograph of the vacuum feedthrough was taken from [90]. (b) Calibration curves of the C₆₀ evaporator, see text for explanation. The data for the plot were taken from Richter's work [90].

4.1. Fullerene C₆₀

In the subsequent sections, the deposition of C₆₀ using a custom-built evaporator is outlined and the results of STM and UPS measurements following C₆₀ deposition at low temperatures and subsequent tempering steps at higher temperatures are presented.

In the discussion section, the electrostatic model illustrating the influence of nearest neighbors on the charge energy is introduced and compared with the shift observed in the UPS spectra of the HOMO level of C₆₀.

4.1.1. Deposition

Commercially available C₆₀ molecules with a manufacturer-specified¹ purity of 99.9% were utilized for the experiments. A specially designed evaporator, developed in the work of Richter [90], was employed for the high-vacuum deposition of the C₆₀ molecules. The evaporator consists of a fused silica (SiO₂) crucible that measures 2.5 cm in height and 1.2 cm in width, with a thin glass tube incorporated for a thermocouple (see figure 4.1(a)). The use of fused silica prevents catalysis, thereby preventing the conversion of C₆₀ to carbon nanotubes, as would occur in a metallic crucible [92]. The tungsten wire that surrounds the crucible is threaded through aluminum oxide beads, providing insulation and ensuring even heating of the crucible [90].

Calibration of the C₆₀ evaporator was done by Richter [90] using a quartz crystal microbalance (QCM) in a separate UHV chamber. Figure 4.1(b) shows a typical calibration curve with a heating current of 8.25 A, resulting in a temperature of (450 ± 3) °C in the crucible². The data was taken from the work of Richter [90].

¹The C₆₀ used in this study was originally purchased in the late 1990s from Materials and Electrochemical Research (MER) Corporation (1985) (MER is also mentioned in [91]). It has been utilized in several previous works within Heinz Hövel's group. Since C₆₀ was stored in a sealed container and in a controlled environment, its quality and purity remain unquestionable due to its inherent inertness.

²The error for the measured temperature was estimated based on the error margin for a K-type thermocouple, which is ±0.75% of the measured temperature value [93].

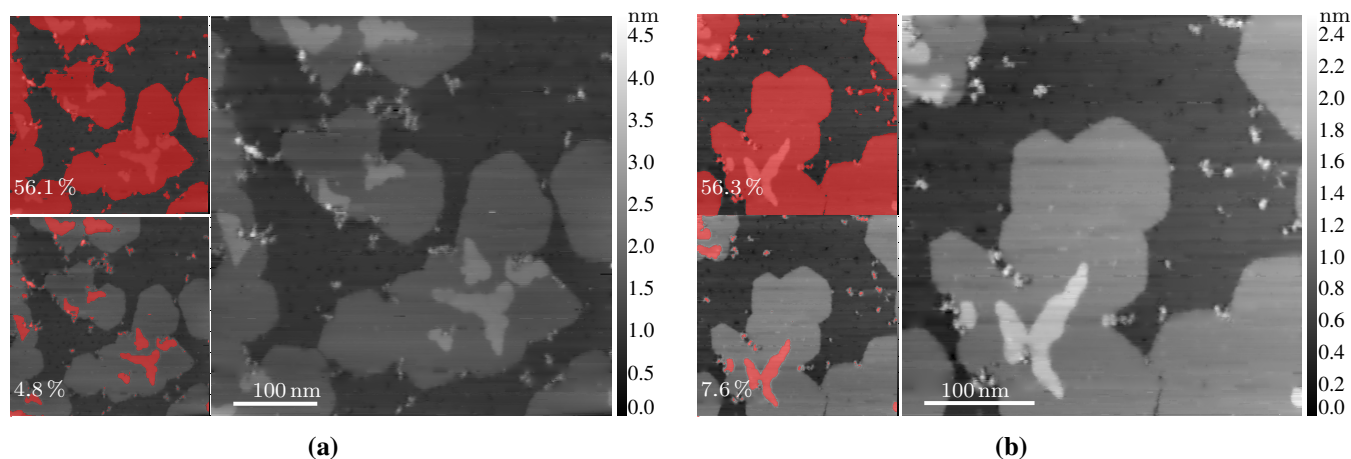


Figure 4.2.: STM measurements for the determination of the evaporation rate of the C₆₀ evaporator. The inset pictures on the left side represent the counted areas of the first (top) and second (bottom) ML. STM parameters: $U = 7.5$ V, $I = 120$ pA. Image resolution of (a) is 500×500 nm² and (b) is 371.5×371.5 nm².

A linear fit to the QCM data (see figure 4.1(b)) gives, according to Richter, an optimal C₆₀ evaporation rate of about $2.0 \text{ \AA}/\text{min}$, resulting in a total time of about 5 min for the evaporation of 1 ML [90]. Here Richter assumes that 1 ML is about 10 \AA high.

Due to technical difficulties, we have not been able to reproduce the QCM experiment. For this reason the experimental results of Richter [90] were used as a starting point, in particular the temperature inside the crucible, which is more reliable than the current and voltage values of the heating filament. The latter can vary over time due to degradation or simply because the filament has been replaced and the length is not exactly the same, leading to a change in resistance.

Two experiments were carried out to verify the calibration of the C₆₀ evaporator. The first experiment was done directly in the main UHV chamber (see Chapter 2.4). We used HOPG as a substrate and deposited C₆₀ at room temperature (RT) aiming for a low coverage of about 1 ML in total. After deposition, STM measurements at LN₂ temperature were performed in order to estimate the coverage. In the course of the current work, the filament of the C₆₀ evaporator broke due to degradation. In order to verify that the evaporation rate did not change when the filament was replaced, the second experiment was carried out in a separate UHV chamber.

A glass slide with a thin strip of stainless steel sheet of 1 mm width was placed in front of the C₆₀ evaporator. A long evaporation time was chosen to achieve a larger film thickness. After deposition, the glass slide was removed from the UHV chamber and, after removing the stainless steel strip, an atomic force microscope (AFM) measurement was made in ambient conditions for the estimation of the coverage of C₆₀ at the step profile created by the stainless steel strip (see Figure 4.3(c)).

In the following, the results of the different calibrations are presented and discussed.

4.1.1.1. Calibration with STM

A HOPG substrate was cleaned by heating it to $600 \text{ }^\circ\text{C}$ for 1 h. After cooling to RT, C₆₀ was evaporated in three steps with a filament voltage $U_{\text{evap}} = 4.4$ V, a filament current of $I_{\text{evap}} = 8.25$ A and an evaporation

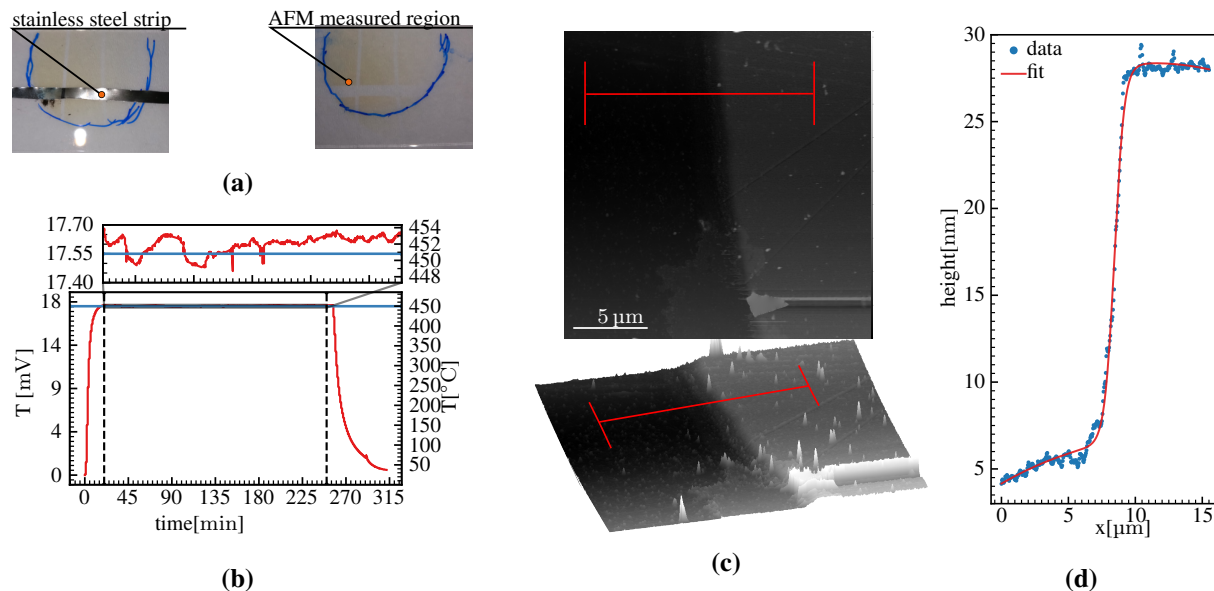


Figure 4.3.: (a) Photographs of large amounts of vapor deposited C₆₀ molecules on a microscope slide. (a) Left: with the stainless steel strip. (a) Right: the area of AFM measurement is marked. The Vertical stripes result from copper wire attachments. (b) The temperature curve of the temperature inside the C₆₀ evaporator crucible. (c) AFM measurement of the C₆₀ step, formed after 60 minutes of evaporation. The red marked area was averaged for the fit of the Boltzmann bent steps profile shown in (d).

temperature of $T_{\text{evap}} = (451 \pm 3) ^\circ\text{C}$. The evaporation times t_{evap} were 1.4 min, 1.4 min and 2.8 min (see table 4.1). Between each evaporation step, UPS measurements³ were taken at RT and, after the last step, STM images were taken at LN₂ temperature. Figure 4.2 shows two of these STM measurements of C₆₀ on the HOPG surface. The first and second ML of C₆₀ have been masked using the Gwyddion software [94] with different height thresholds. The average of the projected area of the first and second ML of C₆₀ in both images is $(62 \pm 2) \%$. So we can say that in about 5.6 min about 62 % of a ML is deposited on the surface using the evaporation parameters mentioned above. A more practical value is the time it takes to deposit 1 ML of C₆₀ on to a surface t_{ML} . For the evaporator parameters presented here, the deposition time is $t_{\text{ML}} = 7.7 \text{ min/ML}$.

4.1.1.2. Calibration with AFM

The C₆₀ evaporator was first operated for about 20 minutes with the shutter closed to allow the evaporator to reach a stable temperature. A heating current of 9.123 A and a heating voltage of 4.56 V were used to keep the temperature at a constant level of $(451 \pm 3) ^\circ\text{C}$. The shutter was then opened for $230 \text{ min} \pm 1 \text{ s}$ and C₆₀ was evaporated on to a microscope glass slide with a stainless steel strip (see Figure 4.3(a)). The temperature was also recorded (see Figure 4.3(b)). After removing the stainless steel strip, the resulting edge was measured with an ambient AFM. We chose the point on the surface of the microscope glass slide, that is likely to correspond to the center of the deposited spot. The layer thickness can be determined by fitting a Boltzmann bent step profile (equation 4.1) to the data (see figure 4.3(d)). This was done using built-in functionality of the Gwyddion software [94].

$$f(x) = y_0 + h/2 \tanh \xi + a\xi + \beta\xi^2, \text{ with } \xi = x - x_0 \quad (4.1)$$

³To compare the evaporation rate and intensity of UPS scans

The height of the step is (21.4 ± 0.4) nm. We can assume that with such a large amount of material deposited at RT, C₆₀ crystallizes in an fcc lattice with a lattice constant of $a_0 = (1.4052 \pm 0.0005)$ nm [95]. The plane distance in (111) direction is given by $a_0/\sqrt{(h^2 + k^2 + l^2)} = a_0/\sqrt{3} = 0.81$ nm, so that 1 ML in a C₆₀ bulk has a height of 0.81 nm [96]. Hence the deposition time for 1 ML of C₆₀ is about 8.71 min or 8 min and 42 s.

In conclusion, the C₆₀ evaporator is quite stable even after changing the filament. The main parameter is the temperature, which then determines the rate of the evaporator. Between the two calibrations discussed above, we have a discrepancy of about one minute in the time taken to evaporate 1 ML. This is probably due to the method of measurement, since the AFM measurement was made in ambient conditions. Adsorption of water and other molecules could have increased the height of the step. Furthermore, the choice of the area to be measured is important. The aim was to capture what was probably the most intense or central part of the evaporation spot.

If we additionally compare the initial calibration of Richter, which is about 5 min per ML (see table 4.1), by analyzing an STM image of C₆₀ on the Au(111) surface (see figure 4-1 in [90]), we can conclude that Richter achieved a coverage of about 56.5 %, which leads to an increase of t_{ML} from 5 min to about 7.2 min.

The STM calibration (see figure 4.2) is therefore the better method, and hence the evaporation time of $t_{ML} = 7.7$ min was used for all further experiments presented in the current work.

It should be noted that the definition of a ML is not a simple one. Especially when it comes to sub-monolayer evaporation rates. Here the adsorption effects, which depend on the local surface structure, substrate temperature and quality of the vacuum, become particularly important. In addition, different materials can generally adsorb differently on various surfaces, leading to variations in the spacing of individual particles and thereby affecting the definition of a ML.

The definition of a ML of C₆₀ in this work can be represented as the complete coverage of a unit area with C₆₀ molecules in a hexagonal close packed (HCP) lattice with a lattice constant of 1 nm.

Table 4.1.: C₆₀ evaporator parameters for different calibrations. U_{evap} is the voltage of the filament, I_{evap} represents the current of the filament, T_{evap} is the temperature inside of the C₆₀ crucible measured with a k-type thermocouple. t_{evap} is the total time used for the particular calibration of the evaporator. For STM three times are given, because the evaporation was done in three steps (see text for explanation). t_{ML} is the time it takes to deposit one ML.

Methods	U_{evap} [V]	I_{evap} [A]	T_{evap} [°C]	t_{evap} [min]	t_{ML} [min/ML]	source
STM	4.40	8.25	451	1.4; 1.4; 2.8	7.7	this work
AFM	4.56	9.11	451	230	8.7	this work
QCM	–	8.25	450	50	5.0	[90]

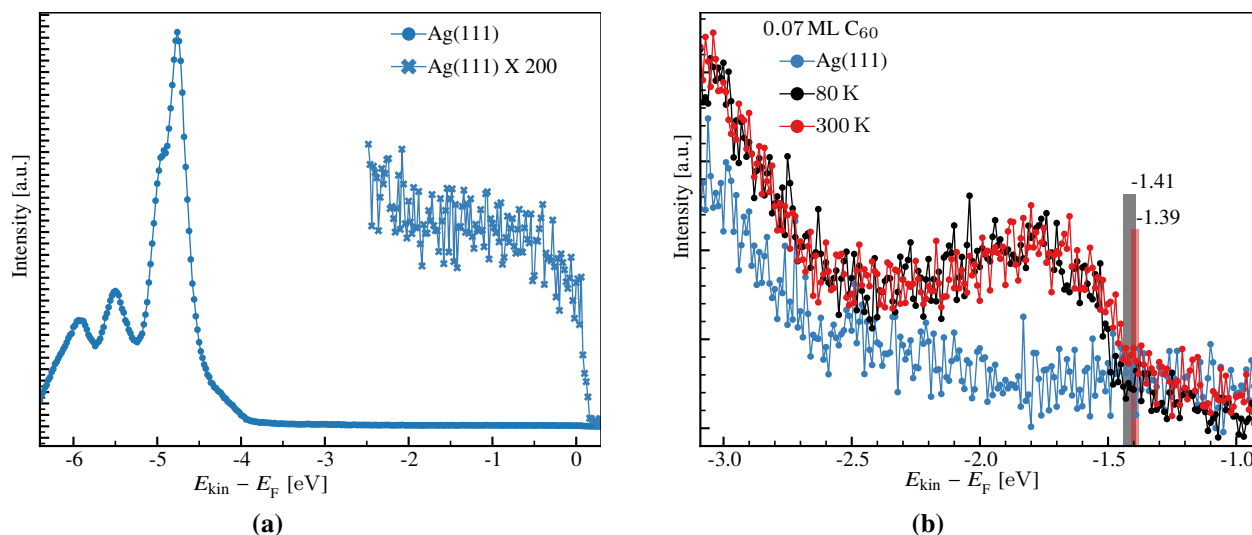


Figure 4.4.: (a) UPS spectrum of the surface of clean Ag(111). The data in the range between -2.5 eV and 0 eV has been scaled up by a factor of 200. Ag(111) is known to have a surface state just below the Fermi level [97]. The absence of the surface state in the spectrum is probably due to its extreme sensitivity to sample orientation with respect to the analyzer. (b) UPS spectra of 0.07 ML of C₆₀ on the surface of Ag(111). 80 K denotes the data taken immediately after deposition at low temperature. 300 K indicates the data taken after annealing at RT for about 60 min. The blue line marked with Ag(111) denotes the spectrum of clean surface of Ag(111). The vertical colored stripes denote the peak onset position (PoP) (see appendix A.1.2) of HOMO of C₆₀. The gray stripe indicates the PoP direct after deposition and red stripe marks the PoP after annealing at RT (see text). The width of the stripes represents the errors of PoP. All spectra were measured in normal emission with an excitation energy E_{exc} of 21.22 eV (HeI α line).

4.1.2. C₆₀ on Ag(111)

Ag(111) is known to have a very low signal in UPS spectra [98] in the vicinity of the HOMO of the C₆₀ molecule[99]. It is therefore suitable for the study of UPS spectra of C₆₀ especially in the sub-monolayer regime. In addition, the preparation of Ag(111) is relatively simple, making it ideal for rapid adjustment of, for example, the amount of evaporated material.

First, the surface of the Ag(111) was cleaned by sputtering (ion bombardment) it for 60 min with argon ions (Ag⁺) at an energy of 1 keV and an Ag⁺ current on the surface I_{sput} of the Ag(111) of $3 \mu\text{A}$. In the second step the annealing process was achieved by resistance heating⁴ of the Ag(111) surface to about 430°C for 60 min.

In the next step the substrate was cooled down to the LN₂ temperature which, due to some losses at the joints connecting the cryostat to the sample holder, resulted in a temperature on the surface of the Ag(111) of about 80 K.

After these preparation steps, a UPS spectrum of the clean substrate was recorded (see Figure 4.4(a) denoted with Ag(111)). Then, about 0.07 ML of C₆₀ was evaporated⁵ onto the surface of Ag(111), followed by a UPS measurement (Figure 4.4(b) denoted with 80 K).

In the next step the sample was heated to room temperature (about 293 K) for about 60 min in the sample holder with the LN₂ cooling still on. Finally, the heating was switched off and, after the sample had been thermalized at 80 K, another UPS spectrum was recorded (see Figure 4.4(b) with label 300 K).

⁴The heating of the surface results in the segregation of impurities from the bulk of the material closer to the surface and the simultaneous desorption of contaminations on the surface, such as residual gases e.g. H₂, H₂O, CO, CO₂. The subsequent sputtering process leads to erosion of the top layer of the surface, which contains most of the impurities. Therefore, the interplay of heating and sputtering improves the quality of the surface [100].

⁵Using the C₆₀ evaporator parameters given in Table 4.1 for STM calibration with $t_{\text{evap}} = 0.56$ min

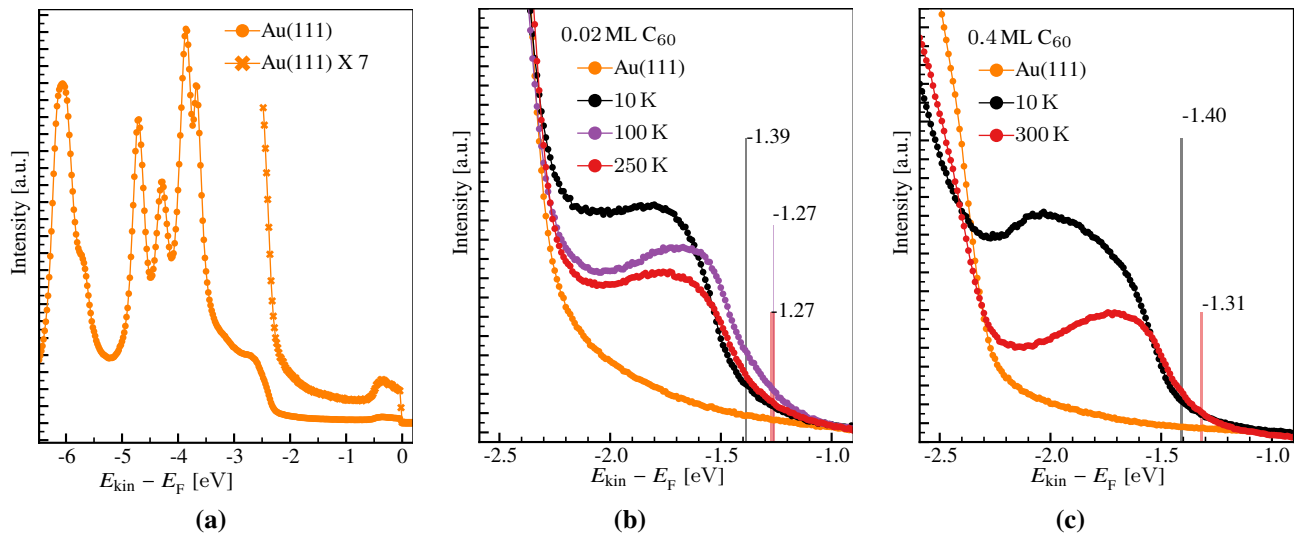


Figure 4.5.: (a) UPS spectrum of the surface of clean Au(111). The data in the range between -2.5 eV and 0 eV has been scaled up by a factor of 7. (b) UPS spectra of 0.02 ML of C_{60} on the surface of Au(111). 10 K denotes the data taken immediately after deposition at low temperature. 100 K and 250 K indicates the data taken at low temperature but after annealing at the corresponding temperature. The vertical colored stripes denote the peak onset position of the HOMO of C_{60} . The width of the stripes represents the errors. All spectra were measured in normal emission with an excitation energy E_{exc} of 21.22 eV (HeI α line).

The HOMO peak of C_{60} on the surface of Ag(111) appears in the range of -2.5 eV to -1 eV. To determine the HOMO, the so-called peak onset position (PoP) was chosen (the discussion and the method of determination can be found in Appendix A.1 and A.1.2). The peak onset positions of C_{60} after deposition and after annealing are almost identical. For the HOMO measured directly after deposition the energy of the PoP is $E_{\text{onset}} = -1.41^{+0.02}_{-0.03}$ eV and the energy of the inflection point is $E_{\text{infl}} = -1.59^{+0.01}_{-0.02}$ eV. Annealing of the sample leads to a minimal shift: $E_{\text{onset}} = -1.39^{+0.01}_{-0.02}$ eV and $E_{\text{infl}} = -1.55^{+0.01}_{-0.02}$ eV.

Unfortunately, no STM images could be recorded for this measurement.

4.1.3. C₆₀ on Au(111)

In order to broaden the study of the HOMO shift or its absence on the surface of metals, Au(111) was used in addition to Ag(111), which was described above.

First the Au(111) was cleaned by heating it to 600 °C for 60 min with subsequent sputtering with Ar^+ with an energy of 1 keV and $I_{\text{sput}} = 2.5$ μ A for another 60 min. The second and final heating cycle was

Table 4.2.: Peak onset position of C_{60} on Au(111) after deposition and after annealing at higher temperatures (T_{ani} [K]), see Figure 4.5. E_{infl} describes position of the inflection point and E_{onset} the position of peak onset (see Appendix A.1.2). ΔE_{infl} and ΔE_{onset} describe the corresponding difference between inflection points and between peak onset positions after deposition and after annealing.

ML	T_{ani} [K]	E_{infl} [eV]	E_{onset} [eV]	ΔE_{infl} [eV]	ΔE_{onset} [eV]
0.02	10	$-1.54^{+0.02}_{-0.01}$	$-1.39^{+0.0}_{-0.01}$		
	100	$-1.45^{+0.03}_{-0.01}$	$-1.265^{+0.003}_{-0.0}$		
	250	$-1.42^{+0.04}_{-0.01}$	$-1.27^{+0.02}_{-0.0}$	$0.12^{+0.05}_{-0.02}$	$0.11^{+0.02}_{-0.01}$
0.4	10	$-1.57^{+0.01}_{-0.03}$	$-1.40^{+0.0}_{-0.01}$		
	300	$-1.48^{+0.02}_{-0.01}$	$-1.31^{+0.0}_{-0.01}$	$0.09^{+0.02}_{-0.03}$	$0.09^{+0.0}_{-0.01}$

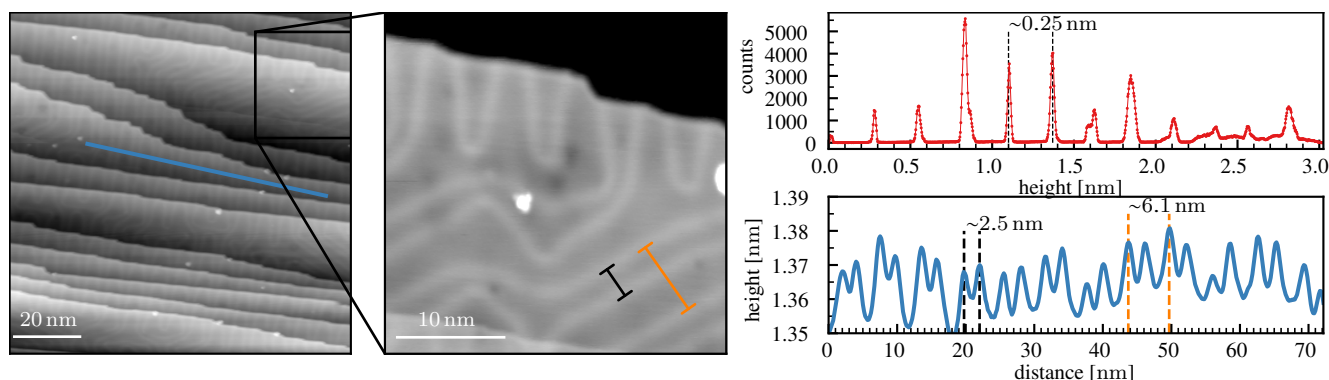


Figure 4.6.: STM image of clean Au(111). Left side: 100x100 nm² image with several terraces. For presentation purposes, the image is flattened so that the superstructure is visible on each terrace. The blue line represents the height profile shown on the right side (bottom). Middle: 31x31 nm² image, zoom on one of the terraces. The black line with end caps indicates the distance between two neighboring soliton walls enclosing the HCP of the Au(111) atoms. The orange line with end caps denotes the periodicity of herringbone structure of the surface of Au(111). Both images were recorded with $U = 2.0$ V, $I = 90$ pA. The red profile in the right upper corner represents binned data from the image on the left side. The bin width is 3 pm.

carried out at 475 °C for a further 60 min.

In the next step, the surface of the Au(111) was cooled to liquid helium temperature, which, due to losses at the joints of the manipulator and sample holder, corresponds to about 10 K on the surface of the Au(111) substrate. Immediately afterwards 0.02 ML of C₆₀ was deposited on to the surface of Au(111) by opening the evaporator shutter for about 10 seconds with the evaporator parameters given in chapter 4.1.1.1. The UPS and STM measurements were then carried out, followed by tempering at about 100 K inside the STM cryostat for about two days, followed again by UPS and STM measurements at liquid helium (LHe) temperature. The final tempering cycle was carried out at 250 K in the sample holder of the manipulator for about 60 min with subsequent STM and UPS measurements at LHe temperature. Additionally, a second experiment was conducted for the sake of reproduction, proceeding as described above, but with a higher coverage of C₆₀ of about 0.4 ML and only one tempering step at 300 K. The following describes the obtained results.

Figure 4.5(a) shows the UPS spectrum of the clean surface of Au(111), where the region between -2.5 eV and the Fermi level has been multiplied by a factor of 7. It can be seen that the d-band of gold is at a lower binding energy than that of silver, so the spectrum of C₆₀ is strongly altered by the d-band of gold in this region. The HOMO peak of C₆₀ on Au(111) is in almost the same range as on Ag(111): -2.5 eV to 1 eV. The peaks onset and inflection point positions are also similar (see table 4.2) Figure 4.6 shows STM measurements on a clean surface of an Au(111) crystal. To characterize the clean surface an average atomic step height was estimated by binning the height data in the Figure 4.6 (left side) with a bin size of 3 pm. By plotting the frequency of height against height, as depicted in the upper right corner of Figure 4.6 (red curve), a Gaussian profile can be fitted to each peak (which represent atomic steps) to estimate an average atomic step height of (0.25 ± 0.02) nm. The fit parameters can be found in Appendix B.1.1 and in Table B.1. The blue curve in the lower right corner of Figure 4.6 represents the profile of the superstructure of the Au(111) surface. The distance between the herringbone structures, as indicated in Figure 4.6 (center) with an orange line with end caps, was also estimated by fitting a Gaussian to each peak to give an average distance of (6.1 ± 0.3) nm. The average distance between neighboring soliton walls (see Figure 4.6 black line with end caps) enclosing the HCP atomic

arrangement is determined to be (2.5 ± 0.2) nm.

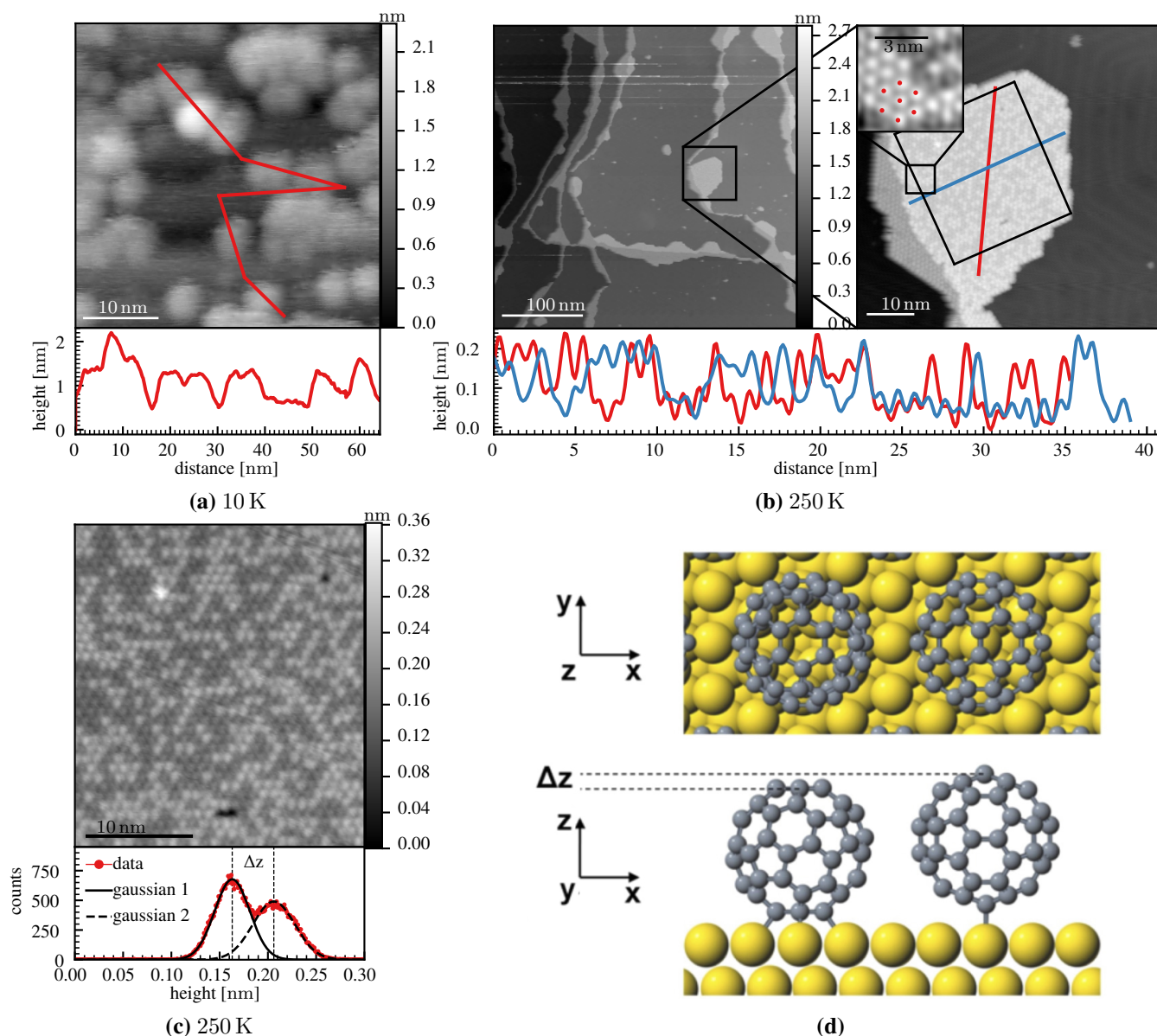


Figure 4.7.: STM of 0.02 ML C₆₀ on Au(111), measured at 10 K. (a) Measured immediately after deposition. Top: 40x40 nm². U = 2.0 V, I = 250 pA. Bottom: Height profile of the red path shown in the top image. (b) Measured after annealing at 250 K. Top left: 374x374 nm². Top right: 64x64 nm² zoom of the black square in the top left image, both recorded with U = 2.0 V, I = 90 pA. The 6x6 nm² slice of the top right image (small black square) represents HCP structure of the C₆₀ island. Bottom: Height profiles of the red and blue paths in the center of the top right image. (c) Top: 27x30 nm² slice of (b) (big black square in the top right image). Bottom: Binned height data of the top image with a bin width of 0.8 pm. Parameters for the Gaussian fits can be found in Table B.5 in Appendix B.1.2. (d) Illustration of different orientations of C₆₀ on the surface of Au(111) [101].

Fitting curves and parameters are given in Figure B.2 and Table B.2. Figure 4.7(a) shows an STM measurement of 0.2 ML C₆₀ on Au(111) directly after deposition at 10 K. The red line in the lower figure shows the height profile along the red line in the upper figure. This signifies one of the few stable images that were successfully obtained. It underscores the challenging nature of STM measurements without annealing, as the adsorbed material is often characterized by loose binding and high disorder.

After annealing, C₆₀ is found to be in an ordered state and mostly adsorbed at the atomic step edges as shown in the left side of Figure 4.7(b). By zooming in on one of the islands (see Figure 4.7(b) on the right), C₆₀ can be observed in a HCP structure (see the inset image of the enlarged section of the

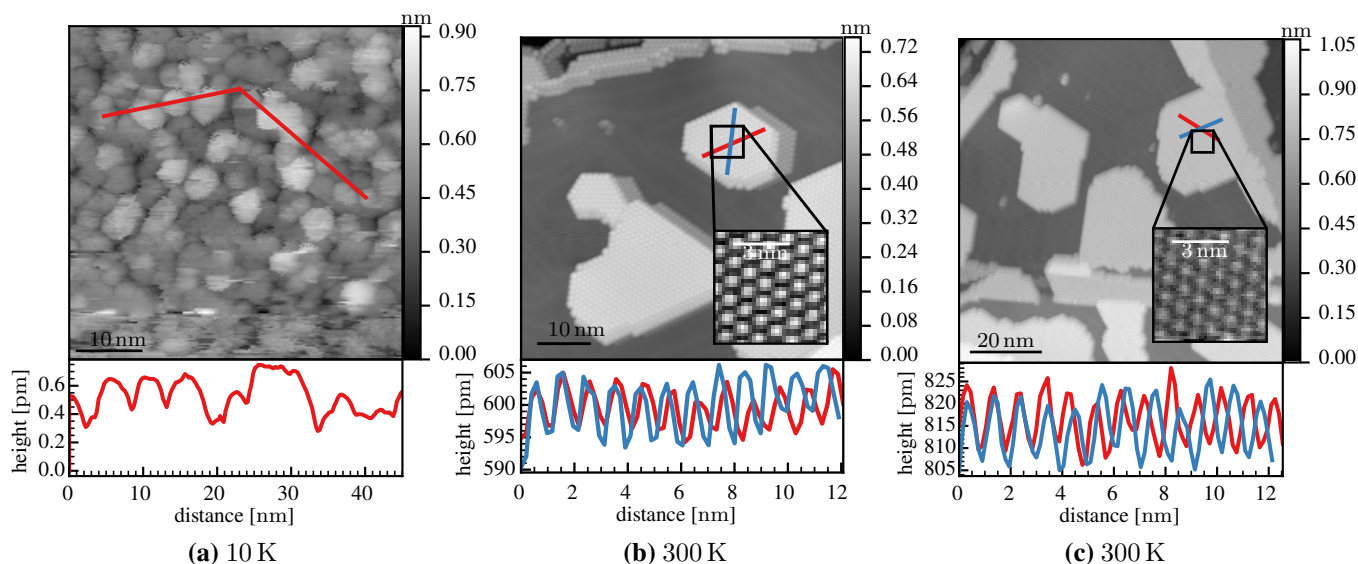


Figure 4.8.: STM on 0.4 ML C₆₀ (a) 50x50 nm² immediately after deposition U = 2.0 V, I = 250 pA (b) 60x60 nm² and (c) 90x90 nm² after annealing at 300 K U = 2.0 V, I = 90 pA

right image in the Figure 4.7(b)) with an average distance between the molecules of 1 nm. The average distance was estimated by fitting Gaussian functions to the red and blue profiles shown in Figure 4.7(b). Thereby the mean distance in the blue profile is (1.02 ± 0.09) nm and in the red profile (1.1 ± 0.3) nm. Fit parameters and fitting curves can be found in the Appendix (Figure B.3, Figure B.4, Table B.3 and Table B.4). The discrepancy in distance between these two estimates is probably due to the drift effect of the STM measurements, which is more pronounced in the slow scan direction, in this case the slow scan direction corresponds to the direction from the top to the bottom of the image.

Within an island, C₆₀ molecules have a different contrast/height in the image. Some of them appear brighter (higher) than others. This is due to the different orientations of the molecules on the surface, so that the brighter molecules are on average (0.0431 ± 0.0004) nm higher. To estimate the mean height difference between two orientations of C₆₀ molecules, height data from a slice of Figure 4.7(b) (marked with a big black square) was binned with a bin width of 0.8 pm and the resulting peaks fitted with Gaussian profiles (see Table B.5 in the Appendix B.1.2). This result correlates with the value of 0.04 nm given in [102], where the authors investigate the orientation of C₆₀ molecules with STM and verify the results with LEED measurements and DFT calculations. According to [101] the brighter (higher) molecules face the surface with a carbon-carbon bond down and bind directly to a gold atom (top side), as depicted in Figure 4.7(d). The darker (lower) appearing C₆₀ molecules face the surface with one of the hexagons and are located above a surface vacancy that allows them to sink deeper (see Figures 4.7(d)).

Figure 4.8 shows the results of measurements of 0.4 ML of C₆₀ on Au(111). As in the previous measurement (see Figure 4.7(a)), the STM results measured immediately after the deposition of C₆₀ are not very reliable and represent a disordered state (see Figure 4.8(a)). Figures 4.8(b) and 4.8(c) show measurements of the sample after annealing at 300 K.

Figure 4.8(b) contains an artifact described in Figure 2.11, which is sometimes referred to as the double-tip artifact. Islands in the image “cast shadows” that appear to be lower than the islands themselves. However the imaging of the top of the island’s surface is not affected because the height difference is lower than the height difference of the double tip.

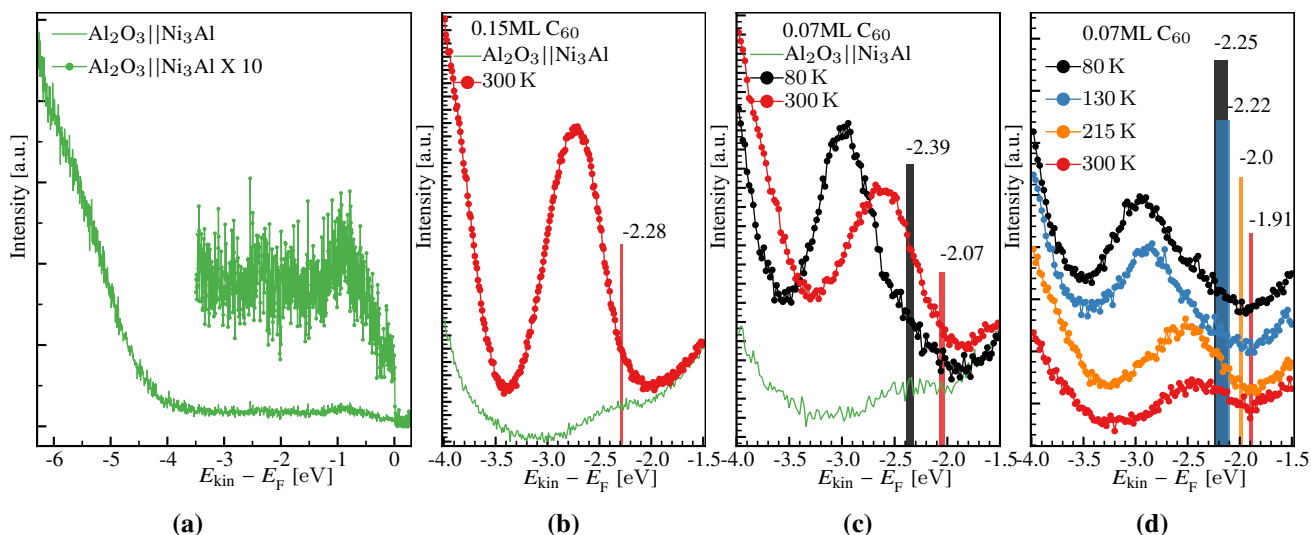


Figure 4.9.: (a) UPS spectrum of the bare surface of Al₂O₃||Ni₃Al(111). The data in the range between -3.5 eV and 0 eV have been scaled up by a factor of 10 (b) UPS spectrum of 0.15 ML of C₆₀ on the surface of Al₂O₃||Ni₃Al(111) deposited at RT. The green curve represents the UPS spectrum of the clean Al₂O₃||Ni₃Al surface. (c) UPS spectrum of 0.07 ML of C₆₀ on the surface of Al₂O₃||Ni₃Al(111) deposited at LN₂ temperature and annealed at RT. (d) Similar experiment as in (c) but with two additional annealing steps. Vertical line represents the position of E_{HOMO}. The width of the stripes represent the errors. All spectra were measured under the angel of 30° to normal emission with an excitation energy E_{exc} of 21.22 eV (HeI α line).

The resolution of the STM measurements⁶ after annealing at 300 K is low and it is not feasible to fit Gaussian profiles to the peaks shown in the Figures 4.8(b) and 4.8(c) (at the bottom). However, it is possible to estimate the distance roughly by counting the number of C₆₀ molecules imaged within the profiles⁷ and dividing the result by the distance between the first and the last molecule. For all four profiles shown in Figure 4.8(b) and Figure 4.8(c), the average distance between the molecules is (0.9 ± 0.2) nm.

4.1.4. C₆₀ on Al₂O₃||Ni₃Al(111)

Before depositing C₆₀ on the surface of Al₂O₃||Ni₃Al, the oxide layer must be built up on the clean surface of Ni₃Al(111).

Six cycles were used for the cleaning process of Ni₃Al(111). Each cycle consists of one sputtering sub-cycle and two heating sub-cycles of the Ni₃Al(111) surface. The sputtering time is 60 min for the first cycle and is decreased for each subsequent cycle. The sputtering parameters remain constant: $I_{\text{sput}} = 5 \mu\text{A}$ and $E_{\text{Ar}^+} = 1.5$ keV. The two heating sub-cycles are at 1150 K and 1000 K for a duration of 7 min each. The heating time remains constant for every subsequent cycle.

Two oxidation cycles are then carried out, consisting of a heating sub-cycle at 1000 K in a thin oxygen atmosphere for 40 Langmuir, which corresponds to 3.0×10^{-8} mbar of oxygen pressure for 30 min exposure, and a flashing sub-cycle of heating the sample at 1050 K for 5 min in UHV.

The final cycle is the cooling of the sample for 30 min in UHV followed by 10 min of flashing at 1050 K. This recipe was developed in the group of Conrad Becker⁸ and was kindly provided to us along with the Ni₃Al(111) crystal. A tabular description of the cleaning and oxidation procedure is given in the Appendix (see Table B.6).

⁶300X300 points for Figure 4.8(b) and 600X600 points for Figure 4.8(c).

⁷Basically by counting all maxima in the profile.

⁸<https://orcid.org/0000-0002-7035-6083>

Three separate experiments were carried out to investigate the behavior of C₆₀ on Al₂O₃||Ni₃Al.

In the first experiment 0.15 ML of C₆₀ was evaporated on the surface of freshly prepared Al₂O₃||Ni₃Al at RT. The evaporation time t_{evap} was 67 s with the same evaporator parameters as given in the chapter 4.1.1.1. A UPS measurement at RT and an STM measurement at LN₂ temperature were then carried out.

In the second experiment, deposition of C₆₀ was performed at LN₂ temperature and the amount of material was reduced to 0.07 ML by reducing the t_{evap} to 33 s. UPS spectra and STM images were both recorded at LN₂ temperature. Then an annealing step at RT with a duration of 60 min with subsequent additional UPS and STM measurements at LN₂ temperature were carried out.

The third experiment reproduced the second experiment with two additional annealing steps at 130 K and 250 K before annealing at RT temperature.

All UPS spectra in the experiments with Al₂O₃||Ni₃Al were taken at an emission angle of 30° with respect to normal emission. This reduces the signal from the substrate and allows better evaluation of the HOMO peak of C₆₀ (see Appendix B.2, Figure B.5). Figure 4.9(a) shows the UPS spectrum of a clean Al₂O₃||Ni₃Al surface. The relatively featureless region between -3.5 eV and 0 eV is up-scaled by the factor of 10.

Figure 4.9(b) shows UPS data from the first experiment with 0.15 ML, where deposition was carried out at RT without tempering. The peak onset is at $E_{\text{onset}} = -2.28_{-0.03}^{+0.00}$ eV and the corresponding inflection point at $E_{\text{infl}} = -2.47_{-0.01}^{+0.01}$ eV.

Figures 4.9(c) and 4.9(d) show UPS spectra from the second and third experiments where the deposition was carried out at low temperature followed by annealing at higher temperature. The peak onset positions for the deposition of both experiments are $E_{\text{onset}} = -2.39_{-0.0}^{+0.07}$ eV and $E_{\text{onset}} = -2.25_{-0.00}^{+0.13}$ eV respectively. After annealing up to RT, both curves show an onset shift of about 0.35 eV. The summarized results of the evaluation of the peak onset positions as well as the positions of the inflection points can be found in Table 4.3. For the reasons given in Appendix A.1.2, only the peak onset shift will be discussed. The inflection point shift is given for comparison and is consistent with the peak onset shift.

The results of the STM measurement for the first experiment are presented in Figure 4.10. Figure 4.10(a) shows a large scan with a few relatively large islands of C₆₀ molecules. Additionally, there are many small islands, as well as separated C₆₀ molecules.

Table 4.3.: Peak onset position of C₆₀ on Al₂O₃||Ni₃Al after deposition at low temperature and after annealing at higher temperature (T_{anl} [K]). Except for the first line denoted with # I, where 0.15 ML C₆₀ was deposited and measured at RT. The corresponding plots are shown in Figure 4.9. # denotes the number of the experiment. E_{infl} describes the position of the inflection point and E_{onset} the position of the peak onset (see Appendix A.1.2). ΔE_{infl} and ΔE_{onset} describe the corresponding difference between inflection points and between peak onset positions after deposition and after annealing.

#	ML	T_{anl} [K]	E_{infl} [eV]	E_{onset} [eV]	ΔE_{infl} [eV]	ΔE_{onset} [eV]
I	0.15	300	$-2.28_{-0.03}^{+0.0}$	$-2.47_{-0.01}^{+0.01}$		
II	0.07	80	$-2.39_{-0.0}^{+0.07}$	$-2.72_{-0.02}^{+0.04}$		
		300	$-2.07_{-0.01}^{+0.04}$	$-2.32_{-0.02}^{+0.04}$	$0.40_{-0.03}^{+0.06}$	$0.32_{-0.01}^{+0.08}$
III	0.07	80	$-2.25_{-0.00}^{+0.13}$	$-2.60_{-0.02}^{+0.07}$		
		130	$-2.22_{-0.00}^{+0.13}$	$-2.54_{-0.02}^{+0.11}$		
		215	$-2.00_{-0.00}^{+0.03}$	$-2.20_{-0.04}^{+0.02}$		
		300	$-1.89_{-0.00}^{+0.04}$	$-2.14_{-0.04}^{+0.02}$	$0.46_{-0.05}^{+0.08}$	$0.36_{-0.00}^{+0.13}$

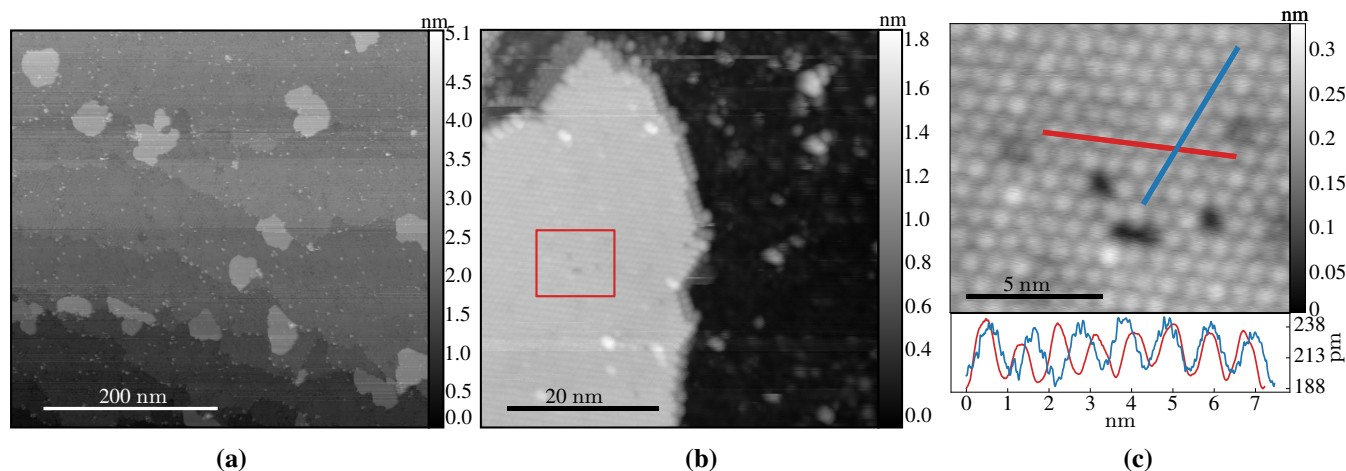


Figure 4.10.: STM measurement at LN₂ temperature of 0.15 ML C₆₀ after deposition at 300 K on Al₂O₃||Ni₃Al. Corresponding UPS data are shown in Figure 4.9(b). (a) A large scan with several C₆₀ island 500x474 nm². (b) 55x55 nm² zoom in on an arbitrary island. (c) 12.5x10.6 nm² slice of the data in (b) denoted by the red square. The blue and red lines in the upper section represent height profiles, each averaged over 16 pixels, with their thickness denoting the averaging, and they are plotted at the bottom. All STM measurements were carried out at liquid nitrogen temperature with STM parameters: U = 3.2 V, I = 90 pA.

Separated C₆₀ molecules, dimers, trimers or small islands consisting of only a few molecules are almost indistinguishable due to the STM tip broadening, caused by the relative high structures (C₆₀ molecules/islands) on surfaces as described in Section 2.3.2, Figure 2.11.

By using the same method as in chapter 4.1.1 (see Figure 4.2) it is possible to estimate the area occupied by C₆₀ molecules on the surface. To accomplish this, all large islands were isolated using Gwyddion [94]. By applying a height threshold to each isolated image (see Appendix B.2, Figure B.6 right side), the total area of large islands in Figure 4.10(a) was estimated to be 21 800 nm². Subsequently, background subtraction was performed on the entire image shown in Figure 4.10(a) by fitting a suitable polynomial⁹. This allowed for the estimation of the area occupied by large islands, small islands, and separated C₆₀ molecules, totaling 47 477 nm² through the same threshold marking¹⁰. The total area of the STM image can be extracted from the metadata and is 237 000 nm².

Given this information of surface coverage in nm² and assuming that C₆₀ forms only two-dimensional islands, as supported by all STM measurements on the 0.15 ML C₆₀ sample, by additionally assuming that one ML of C₆₀ corresponds to complete coverage of the substrate surface in the HCP structure, all large islands occupy about 0.092 ML, while the small islands and separated C₆₀ molecules occupy about 0.11 ML of the total surface area.

No error was estimated for these values. The main error originates from the structure broadening caused by the STM tip. This broadening occurs mostly on the edges of islands. For small islands or separated C₆₀ molecules, this effect is even more pronounced, leading to an overestimation of the total coverage of small islands.

Also thermal drift as well as piezoelectric actuator nonlinearities (creep and hysteresis)¹¹ are effects which could effect the measurements. If we assume that these effects influence the measurements in the same way within an image, then the ratios between the coverage of the large islands and separated

⁹Considering only the area of the islands and not the height, background subtraction does not affect the result.

¹⁰These steps are vital because using only threshold masking can't accurately estimate the areas of islands and smaller particles separately due to intervening atomic steps.

¹¹For detailed explanation and possible correction methods see for example the work of M. P. Yothers et al. [103]

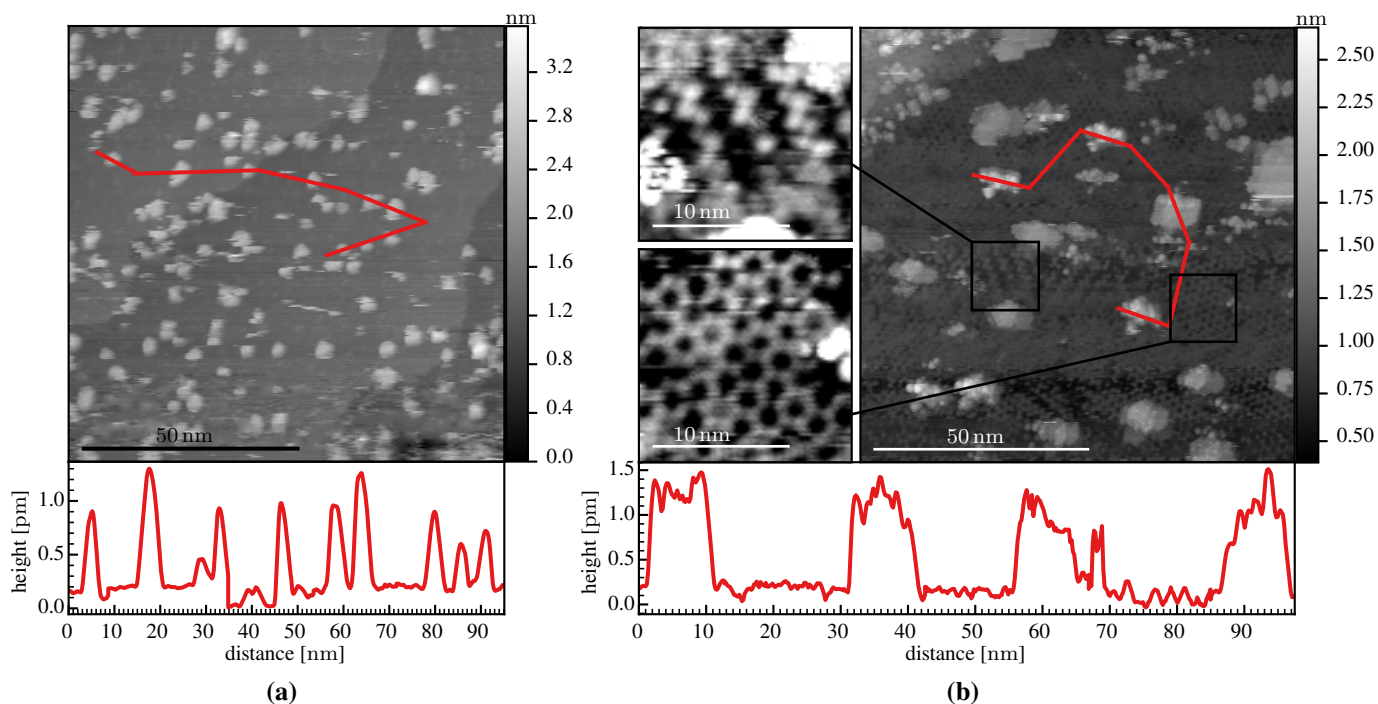


Figure 4.11.: 100x100 nm² STM images of 0.07 ML of C₆₀ deposited at 80 K on Al₂O₃||Ni₃Al with one annealing step at 300 K. The corresponding UPS data is shown in Figure 4.9(c). (a) STM measurement taken directly after deposition at LN₂ temperature. The red curve at the bottom represents the height profile of the red path shown in the upper part of the figure. (b) STM measurement taken after annealing at 300 K for 60 min. The red curve at the bottom represents the height profile of the red path shown in the upper right part of the figure. Top left side: 15.5x15.5 nm² zoom in on the stripe phase. Bottom left side: 15.5x15.5 nm² zoom in on the network structure. All STM measurements were carried out at liquid nitrogen temperature with STM parameters: U = 3.2 V, I = 90 pA.

C₆₀ molecules remain the same, except for the already mentioned overestimation by the broadening of the small aggregates. So it is feasible to say that by vapor deposition of 0.15 ML of C₆₀ at RT onto the surface of Al₂O₃||Ni₃Al(111), about 0.1 ML of C₆₀ forms large islands while the remaining C₆₀ molecules adsorb separately or in significantly smaller islands.

Figure 4.10(b) shows an STM image of a large island. The edge of the island appears double in the image. This effect originates from the STM tip, which probably accumulated an adsorbate on the side. However, this only affects high structures, so the surface of the C₆₀ island, where height differences are on the order of a few tens of picometres, remains unaffected, as shown in Figure 4.10(c). The figure provides a zoomed-in view of the region marked by the red square in Figure 4.10(b). Thereby the red and blue lines represent height profiles and are shown in the bottom part of Figure 4.10(c). By fitting each peak of C₆₀ molecules with Gaussian profile it is possible to calculate the average distance between the molecules (see Figure B.7 and Tables B.7 and B.8 in the appendix). The average distance between C₆₀ molecules in the red profile is (0.898 ± 0.007) nm and in blue profile (1.06 ± 0.02) nm. This discrepancy originates from the thermal drift, which is still present at this low temperature (about 80 K), especially because this image was recorded at a relatively low speed¹² of 20 nm/s. STM measurements are known to sometimes be sensitive if an image is taken at a different scanning speed or with a different frame size compared to the calibration settings. It is possible to correct this drift by calculating the drift vector (e.g. Gwyddion [94] has several tools for such operations) and subtract it from every pixel in the image. Such corrections can sometimes distort the image and produce incorrect results. Therefore in the course of the

¹²The operation at higher speed showed instabilities in this particular measurement.

present work as few corrections as possible have been applied to the STM data¹³.

There is also a lot of research on adsorbed C₆₀ layers on the surface of densely packed metals such as Au, Ag, Pt, Al or even graphite, where the C₆₀-C₆₀ distance is almost always found to be around 1 nm or slightly higher (an overview can be found in Table 1 in the work of J. A. Smerdon et al. [104]). Therefore, the distance between C₆₀ molecules represented in Figure 4.10(c) is likely around 1 nm, rather than the measured value of (0.898 ± 0.007) nm extracted from the line parallel to the fast scanning direction¹⁴ of the STM (refer to Figure 4.10(c)). The angle between the red and blue profiles is about 63.5°, which deviates from the ideal HCP structure with an angle of 60° and is also caused by thermal drift and/or possible sub-optimal calibration.

In conclusion, it can be claimed that the C₆₀ rearranges itself in the HCP structure on the surface of the Al₂O₃||Ni₃Al after deposition at RT. The thermal energy of the system is sufficient to form large islands. Therefore, each C₆₀ molecule has 6 neighbors, except for the molecules at the edges of the islands and those that are bound to the surface individually or in dimers, trimers and other smaller islands.

Figure 4.11 shows the results of the second experiment with the deposition of C₆₀ at LN₂ temperature with an additional annealing step at 300 K. The corresponding UPS measurement can be found in Figure 4.9(c). The quality of the STM data is not good enough to analyze it quantitatively. The STM image taken immediately after deposition is quite unstable, probably due to the loose material on the surface which disturbs the measurement and has a tendency to bind to the tip, causing additional broadening or double structures in the image, especially for such high structures as C₆₀. The post-annealing images are also very unstable, probably because the annealing temperature was not high enough to bind all the material to the surface.

However, comparing the profiles in Figures 4.11(a) and 4.11(b) and the corresponding images, one can say that the C₆₀ molecules form larger islands after annealing. In consequence, the surface of the substrate can be imaged better to reveal the network structure and the so called stripe phase with the zigzag structure [105] of the Al₂O₃||Ni₃Al surface (see enlarged parts of Figure 4.11).

Before annealing, the C₆₀ molecules are likely to be mostly single molecules or very small aggregates such as dimers or trimers, since each peak width in the profile in Figure 4.11(a) is less than 2 nm and all other structures in the image appear to be very similar in shape.

Figure 4.12 shows the STM results of the third experiment with the deposition of 0.07 ML C₆₀ at low temperature (80 K) and after the last annealing step at 300 K. A total of three annealing steps were applied at 130 K, 215 K and 300 K each for 60 min. However, only STM data for the deposition and after the final annealing step is reliable enough for analysis. The corresponding UPS measurement is shown in Figure 4.9(d).

As in the second experiment, the data for the STM measurement after the last annealing step at 300 K (see Figure 4.12(b)) cannot be quantitatively evaluated due to the image quality, but it can be stated that C₆₀ is mostly aggregated into large islands, which are probably rearranged in the HCP structure.

¹³Mostly plane correction was applied because the surface plane is often tilted relative to the STM tip, causing the surface slope to overshadow the surface structure. Subtracting a simple plane fit from the data greatly aids interpretation.

¹⁴The fast scanning direction is typically more reliable for distance measurements in STM images.

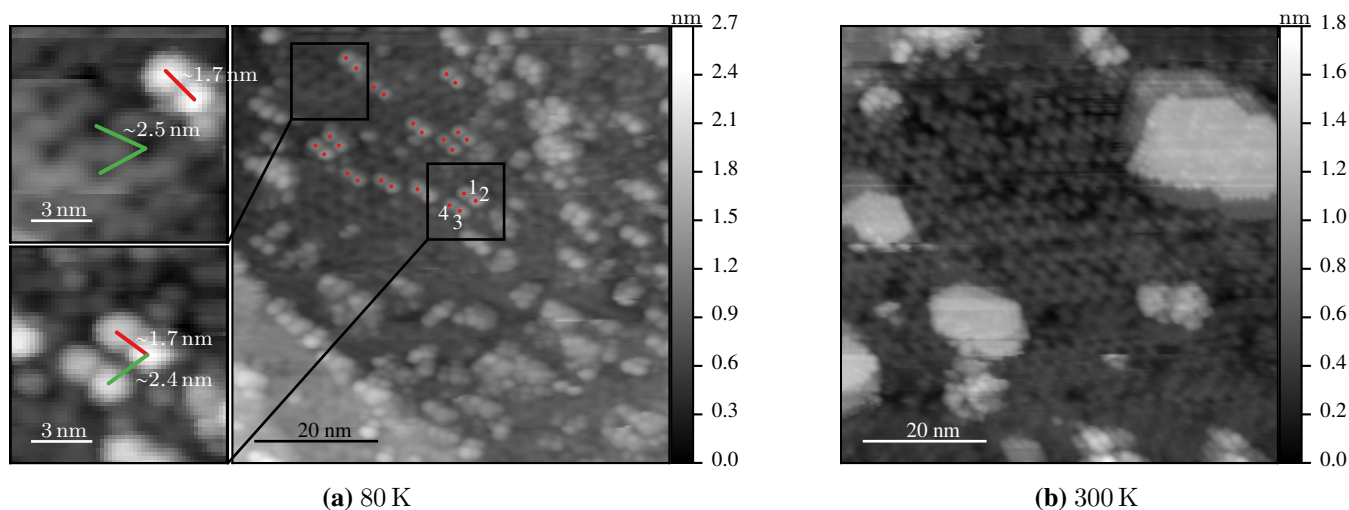


Figure 4.12.: STM measurements of 0.07 ML of C₆₀ on Al₂O₃||Ni₃Al. The corresponding UPS data is shown in Figure 4.9(d). (a) 60x60 nm² after deposition at 80 K. The numbers 1,2 and 3,4 denote two adjacent pairs. The enlarged sections of the image represent 10.6x10.6 nm² zooms marked by the black squares. The red lines represent average distance between molecules. The green lines in the upper enlarged image represent the lattice vectors of the network structure. The green line in the lower enlarged image denotes the distance between adjacent pairs. (b) 60x60 nm² after the third annealing step at 300 K.

Figure 4.12(a), taken immediately after deposition at 80 K, shows the network structure of the Al₂O₃||Ni₃Al, which is shown in the enlarged section of the image. By measuring the distance between several dark appearing spots of the network structure¹⁵ and averaging them, the network structure lattice factor is found to be (2.5 ± 0.2) nm. The average angle between the lattice vectors is determined to $(56 \pm 4)^\circ$. Compared to the literature values of 2.4 nm and 60° [64], these results are within an acceptable range of error.

In Figure 4.12(a) one can also find a pattern of C₆₀ molecule pairs, indicated by red dots. One of the pairs is marked by the red connecting line in the upper enlarged part of Figure 4.12(a) and another pair is visible in the lower enlarged part. The average distance between two C₆₀ molecules within a pair is¹⁶ (1.7 ± 0.1) nm.

Another prominent structure in the image is two adjacent pairs, shown in one of the black rectangles in Figure 4.12(a) with the respective C₆₀ molecules labeled 1 - 4. The average distance between adjacent pairs (distance between molecules 2 and 3 or 1 and 4 in Figure 4.12(a)) is (2.4 ± 0.1) nm (there are three adjacent pairs in total visible in Figure 4.12(a)).

Figure 4.13(a) shows a schematic representation of the network structure, with the six high points marked with blue circles. For better visibility, the high points are replaced by red hexagons, with each corner representing a high point (see Figure 4.13(b)). The distance between the adjacent pairs in Figure 4.12(a) corresponds to the lattice constant of the network structure a_{net} . However, the distance a_{pair} between two C₆₀ molecules within a pair (1.7 nm, red line in Figure 4.12(a)) is much smaller than the lattice constant $a_{\text{net}} = 2.4$ nm. So a_{pair} is probably the distance between every second high point of the red hexagons along the direction denoted with the blue arrow in Figure 4.13(b). This could also explain the slight angle between the lattice vector (green line) and the vector along the distance between two C₆₀ molecules within a pair (red line) in the enlarged part of Figure 4.12(a) in the upper left corner.

Another noticeable feature of Figure 4.12(a) is the orientation of all the pairs in one direction. This could be an indicator of a different underlying structure. One potential candidate could be the stripe phase with

¹⁵Black dots connected with green lines in the upper enlarged section of Figure 4.12(a).

¹⁶The distance of the C₆₀ molecules was determined using an algorithm described in Appendix A.4.

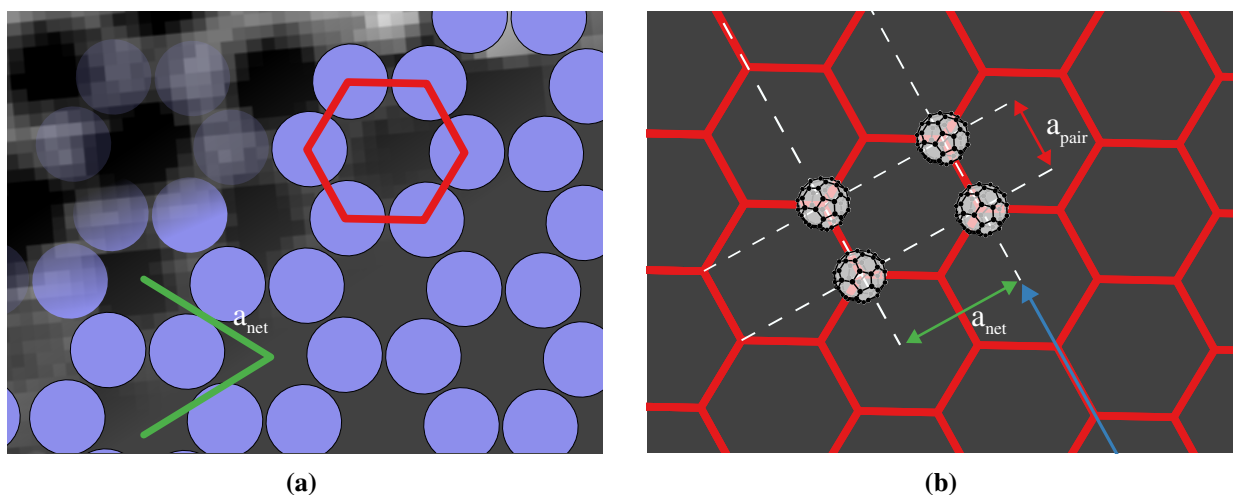


Figure 4.13.: Network structure model. (a) The blue circles represent the high points of the network structure in the STM image, see the enlarged section of Figure 4.12(a) in the upper left corner. The green lines denote the lattice constants of the network structure $a_{\text{net}} = 2.4 \text{ nm}$ [64]. (b) Possible adsorption of C₆₀ on the network structure. The intersections of the red lines represent the high points of the network structure as indicated with a red hexagon in (a). a_{pair} and a_{net} represent the distance between two C₆₀ molecules within a pair and between adjacent pairs, respectively, as described in the text.

its zigzag shape, which aligns in a specific direction on the surface (see Figure 4.11(b) left upper corner). It is either that C₆₀ adsorbs on the surface of Al₂O₃||Ni₃Al only in areas where the zigzag structure appears, or the presence of C₆₀ induces local rearrangement on the surface of Al₂O₃||Ni₃Al, making the zigzag structure more favorable but existing only locally beneath C₆₀.

The adsorption scheme, as shown in Figure 4.13(b), is based solely on the STM data. Therefore, another verification method, such as LEED or AFM, is still necessary. It is known that the dot and network structure of the Al₂O₃||Ni₃Al act as nucleation points, at least for the metal clusters, such as Cu, Ag, Au, and V [106].

However, there is currently no literature on the nucleation of clusters or molecules at shorter distances, as the lattice constant of both superstructures of Al₂O₃||Ni₃Al. Therefore, it is possible that the electronic structure properties of C₆₀ molecules, combined with low-temperature and low-coverage deposition, cause the molecules adhere to the grid of the network structure visible in STM (see Figure 4.12(a) and Figure 4.13(b)).

4.1.5. Discussion

Figure 4.14a shows the UPS spectra of the clean surfaces of Au(111), Ag(111) and Al₂O₃||Ni₃Al. The spectra in the region of the first 5 eV below the Fermi level are very different. For gold the d-band starts at about -2 eV in contrast to silver and the oxide layer where the spectrum is quite flat up to about -4 eV. As a result the signal from adsorbed C₆₀ molecules is affected in different ways. On the surface of Au(111) the d-band structure has a greater effect on the HOMO peak of C₆₀ than on the surface of Ag(111) and Al₂O₃||Ni₃Al. Fortunately, by considering the peak onset position of C₆₀, the influence of the substrate features can be neglected, especially for Ag(111) and Al₂O₃||Ni₃Al.

The position of the HOMO peak of C₆₀ is also quite different on the considered surfaces. Whereas on the surface of metals such as Ag(111) and Au(111) the HOMO peak appears at almost the same position, on the surface of Al₂O₃||Ni₃Al this position is strongly shifted to a higher binding energy (see

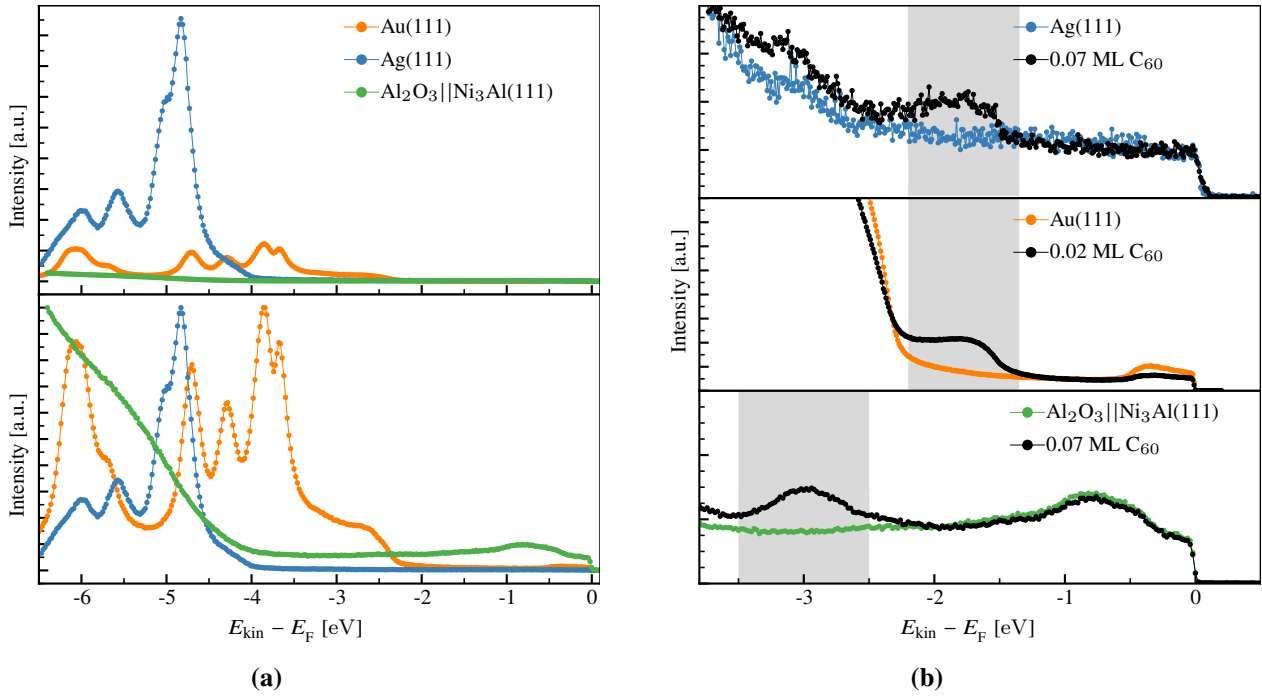


Figure 4.14.: UPS of different substrates. (a) Top panel: Au(111) at 10 K, Ag(111) at 80 K, and Al₂O₃||Ni₃Al(111) at 80 K. The spectra were normalized to minimize differences in the featureless region below the Fermi edge. (a) Bottom panel: The same spectra as shown in the top panel, normalized to their respective maximum value. (b) Locations of HOMO peaks of C₆₀ on different surfaces. Data for Ag(111) was taken from Figure 4.4, for Au(111) was taken from Figure 4.5(b) and the data for Al₂O₃||Ni₃Al was taken from Figure 4.9(c).

Figure 4.14(b)). One might think that C₆₀ binds differently to Al₂O₃||Ni₃Al than to the two noble metals. However, we suggest that this effect is due to the charging of the C₆₀ molecules rather than the chemical binding to the substrate. During the photoelectric effect, C₆₀ molecules are positively charged by the emission of an electron. Here we define the energy of the positively charged C₆₀ as U_0 . This energy leads to a change in the kinetic energy of the electron flying towards the detector, often referred to as the binding energy in UPS. On the surface of the two noble metals U_0 is probably minimal, hence we observe very small to no shift in the HOMO peaks of C₆₀ on the surface of Au(111) and Ag(111). Al₂O₃||Ni₃Al however is a poor electrical conductor (the band gap is about 7 eV [107]) so it cannot balance the positive charge of C₆₀ fast enough. This results in a much larger shift of the HOMO level of C₆₀.

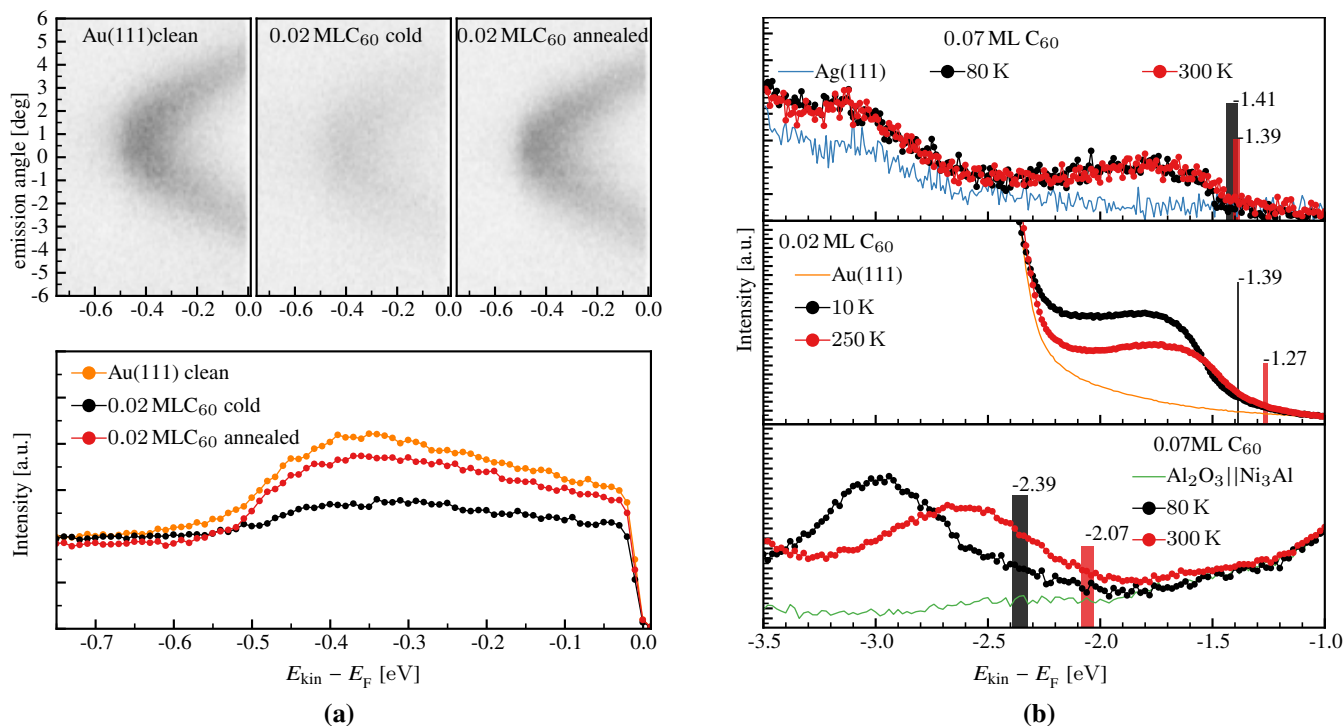


Figure 4.15.: (a) Influence of C₆₀ on the surface state of Au(111) as described in text. (b) Shift of the HOMO peak of C₆₀ observed on different surfaces. The data was taken from the same UPS measurement as shown in Figure 4.14(b).

Evidence for a weak interaction of C₆₀ with Au(111) can be seen in Figure 4.15(a), which shows one of the experiments with C₆₀ on Au(111) (see also Figure 4.5(b)). The upper part of the figure shows angle resolved photoelectron spectroscopy (ARPES) data of the region of the surface state of Au(111) before deposition of C₆₀, after deposition and after annealing at 250 K. The lower part of the figure shows the same data but integrated along the emission angles.

As can be seen, the intensity of the surface state of Au(111) is strongly reduced after deposition of C₆₀, but heals almost completely after annealing. Energetically it remains at the same position. The surface state is known to be sensitive to the adsorbates. Sometimes the interaction between the adsorbate and the substrate leads to an energetic shift [108] or even to the complete extinction of the surface state by the chemisorption [109]. This behavior indicates that C₆₀ molecules have little to no chemical bonding to the substrate and are probably physisorbed.

Additional information can be obtained from UPS data of annealing experiments. Figure 4.15(b) shows a comparison of the HOMO peak shift of C₆₀ after deposition on different substrates and additional **Table 4.4.:** Overview of experimental results of HOMO shifts in UPS measurements of C₆₀ on different substrates. Data taken from section 4.1.2 and tables 4.2 and 4.3

Substrate	ML	Exp. #	ΔE_{inf} [eV]	ΔE_{onset} [eV]
Ag(111)	0.07	I	$0.04^{+0.01}_{-0.02}$	$0.02^{+0.02}_{-0.03}$
Au(111)	0.02	I	$0.12^{+0.05}_{-0.02}$	$0.11^{+0.02}_{-0.01}$
	0.4	II	$0.09^{+0.02}_{-0.03}$	$0.09^{+0.0}_{-0.01}$
Al ₂ O ₃ Ni ₃ Al	0.07	I	$0.40^{+0.06}_{-0.03}$	$0.32^{+0.08}_{-0.01}$
	0.07	II	$0.46^{+0.08}_{-0.05}$	$0.36^{+0.13}_{-0.00}$

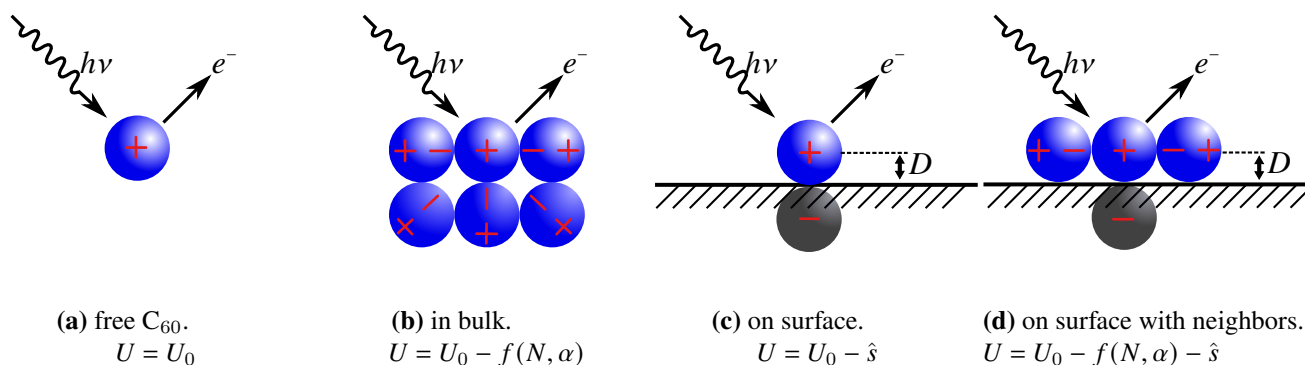


Figure 4.16.: Simple picture of the charge screening caused by next neighbors in the UPS process.

annealing at RT. The data is taken from sections 4.1.2, 4.1.3 and 4.1.4. Thereby C₆₀ on Ag(111) shows almost no shift of the peak onset position of HOMO, on Au(111) the shift is around 0.1 eV, where the shift on the surface of Al₂O₃||Ni₃Al is greater than 0.3 eV (see table 4.4). In the case of Au(111) the shift could be affected by the vicinity of the d-band structure of gold as mentioned above. This result therefore requires further investigation, preferably with an additional method that is not influenced by the d-band structure of Au(111).

Considering all the STM results, it can be said that directly after deposition at LN₂ temperature on the surface of Au(111) or Al₂O₃||Ni₃Al, the C₆₀ molecules are distributed amorphously and no long range ordered structure could be found. In the case of Al₂O₃||Ni₃Al, STM results taken directly after deposition lead to the conclusion that the minimum distance of C₆₀ molecules is about 1.7 nm and the network structure of Al₂O₃||Ni₃Al could serve as a template for nucleation (see section 4.1.4). After annealing up to 300 K, C₆₀ rearranges to a HCP structure on both substrates. The majority of the C₆₀ molecules are contained in large islands where except for the edges each molecule almost always has six nearest neighbors and the distance between the molecules is about 1 nm.

In conclusion, according to the experimental data with UPS and STM on C₆₀ molecules deposited on different surfaces at low temperature, the molecules start as separate entities and aggregate into larger HCP islands after tempering. The HOMO peak shift after tempering on the surface of Al₂O₃||Ni₃Al is much larger than on the surface of Au(111) and almost disappears on the surface of Ag(111).

The HOMO shift observed can be explained by considering the difference in screening between the free C₆₀ molecule and the C₆₀ on the substrate surface surrounded by other C₆₀ molecules in electrostatic approximation. For solid C₆₀, screening is mostly due to its large polarizability [110], while the interaction between the molecules are non-covalent and weak and can be neglected [111]. So as discussed above, we can define U_0 as the charging energy of a free C₆₀ ion. Neighboring molecules reduce the charging energy due to dipole induction by a factor of¹⁷:

$$f(N, \alpha) = \frac{1}{2} N p E = \frac{1}{4\pi\epsilon_0} \frac{N e^2 \alpha'}{2R^4} \quad (4.2)$$

where N is the coordination number, $p = \alpha E$ the electric dipole moment, $\alpha' = \alpha(4\pi\epsilon_0)^{-1}$ the polarizability

¹⁷This energy originates from the consideration of the charge transfer in the molecule against the repulsive force $F = -kx = QE$ [112, p29]

volume and α the polarizability, e the elementary charge and $E = e(4\pi\epsilon_0 R^2)^{-1}$ the electric field of a point charge.

Proximity to the surface reduces the charging energy further by a factor defined here as \hat{s} . In the case of the metallic surface such as Au(111), this could be approximated by the mirror image model (see Chapter 2 in [113]), where the ionization potential increases and the electron affinity decreases by the same factor $e^2(16\pi\epsilon_0 D)^{-1}$ [110]. Thereby D is the distance from the C₆₀ molecule to the surface, so the surface factor becomes:

$$\hat{s} = \frac{e^2}{8\pi\epsilon_0 D} \quad (4.3)$$

This contribution originates from the consideration of the reduction of the HOMO-LUMO¹⁸ gap. Because in the present work no experimental data is available for LUMO peaks¹⁹ and because we focus on the difference between the arrangement of C₆₀ on surface as denoted in Figure 4.16(c) and Figure 4.16(d), \hat{s} eliminates and will not be discussed.

Using Expression 4.2, the total shift of the HOMO peak can be calculated. With a coordination number of 6 (which probably describes the most common arrangement of C₆₀ on the surface after annealing), the experimentally obtained polarizability volume of free C₆₀ of $(76.56 \pm 8.00) \text{ \AA}^3$ [114] and with the intermolecular distance of $R = 1 \text{ nm}$ for the case of the C₆₀ in the large HCP islands, Expression 4.2 yields a total shift of the HOMO peak of $(0.33 \pm 0.03) \text{ eV}$.

For C₆₀ distances of 1.7 nm or greater as observed in the case before aggregation (see Figure 4.12(a)), the shift is smaller by at least a factor of $(1.7)^4 \approx 8.35$.

Taking into account the HOMO shift of C₆₀ on the surface of Al₂O₃||Ni₃Al, which was experimentally determined in this work (see table 4.4 ΔE_{onset}), this model describes well the experimental results within the scope of error. The UPS results of the experiments on the surface of Au(111) and on the surface of Ag(111) show almost no shift after annealing up to RT

A possible explanation could be the different nature of the substrate: Ag(111) and Au(111) are metals, while Al₂O₃||Ni₃Al is a poor conductor. The reason for this may be that the charging energy U_0 disappears on metallic surfaces, as discussed for metallic clusters on HOPG in the work of Hövel et al. [115]. There is also evidence for a shift of the LUMO peak of C₆₀ on the surface of Au(111) [111], which was determined by STS measurements and is in good agreement with the model at around 0.4 eV ²⁰.

¹⁸Lowest unoccupied molecular orbital (LUMO)

¹⁹Experimental data of the LUMO can be collected by methods like inverse PES or scanning tunneling spectroscopy (STS).

²⁰Authors of [111] could not observe the shift in HOMO with STS. They also did not specify at which specific position within C₆₀ molecule the measurements were made. However, there is evidence that the HOMO peak of the C₆₀ disappears on specific parts of the molecule in STS measurements [116].

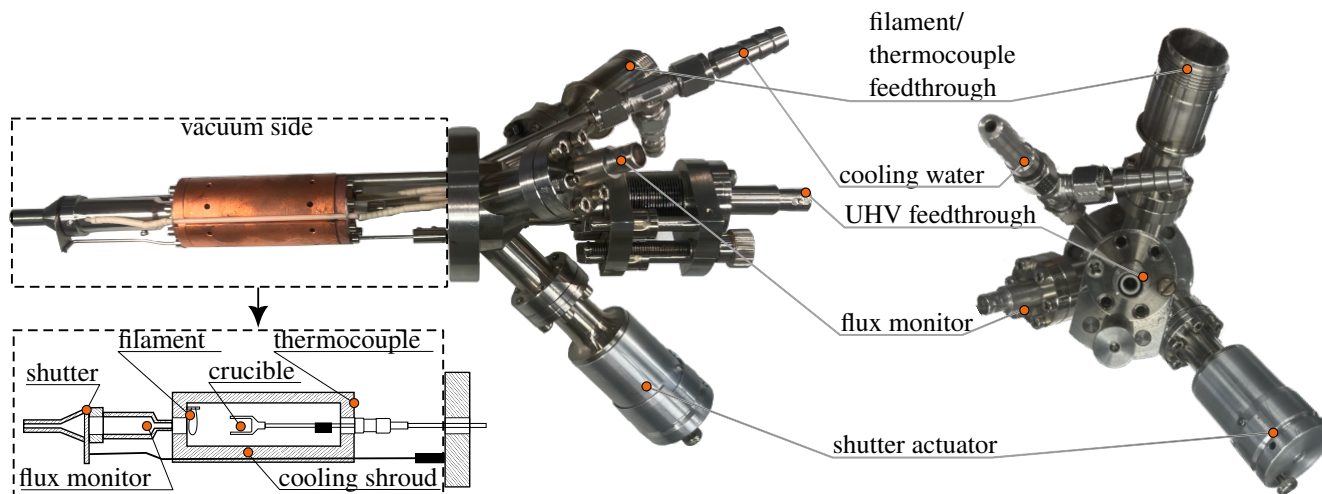


Figure 4.17.: UHV evaporator EFM 3. Left side: Photo of the evaporator from the side. Dashed box indicates the vacuum side. Right side: Photo of the evaporator from behind, along the evaporation axis. Only the non-vacuum side is visible.

4.2. Bismuth

In this section, the calibration of commercially available evaporators with flux control and an automatic shutter actuator for Bi is described. Additionally, a special high-precision calibration technique is detailed, based on LEED measurements of Bi on the surface of Au(111). These measurements are compared to STM measurements taken from the literature in order to obtain precise Bi coverage.

UPS and STM experiments with Bi on the surface of Au(111) and $\text{Al}_2\text{O}_3||\text{Ni}_3\text{Al}$ from deposition at low temperature to annealing at high temperature are then presented and discussed in the context of electrostatic approximation.

4.2.1. Deposition

For the Bi experiments, commercially available material was used in the form of beads with a size between 1 and 4 mm. The purity specified by the manufacturer [117] is 99.999 %.

According to the data sheet, inductively coupled plasma optical emission spectroscopy (ICP-OES) and inductively coupled plasma mass spectrometry (ICP-MS) were used by the manufacturer to identify the purity. The major impurity originates from Fe with 0.3 ppm, Ni, Cu, Zn, As, Ag, Cd, Sn, Sb, Hg, Pb only contribute to the impurity with <0.1 ppm.

As already mentioned in Chapter 2.2, to bring the material in UHV on the surface of the crystal, PVD was used.

Within the scope of this work, an EFM 3 from the company Focus was used which has two additional features worth mentioning: First, a flux monitor, which measures the ion flux of the material and if a certain set point is defined, adjusts the high voltage of the e-beam heater to keep the flux constant. Second, a stepper motor control unit can open and close the shutter actuator very precisely. These two features are crucial to increase the precision of the material deposition, especially in the sub-monolayer regime.

The basic principle of EFM 3 operation is as follows. A current is applied to the filament, electrons

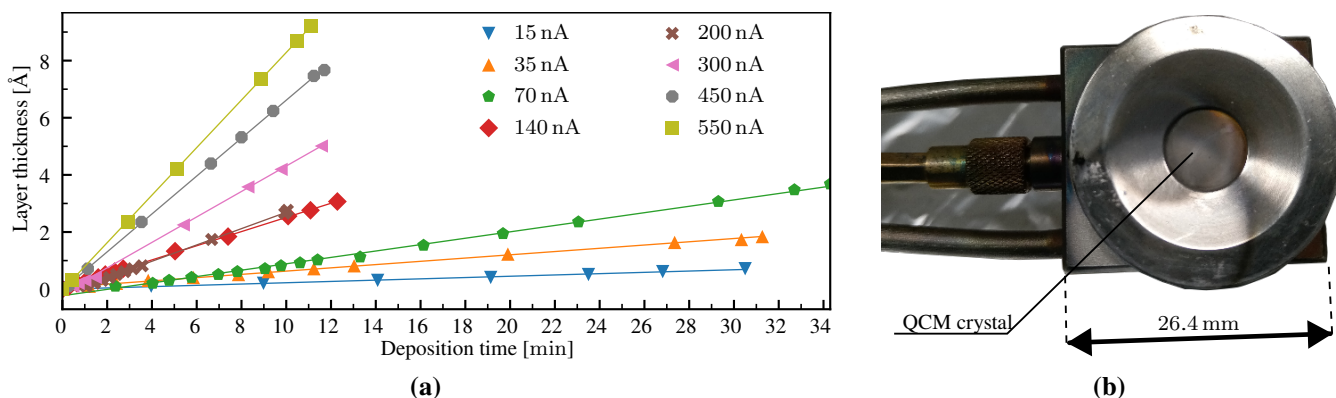


Figure 4.18.: Deposition of bismuth. (a) Deposition amount versus deposition time. Error bars are not shown for clarity (see text). Straight lines are fitted to the data and are only indicative. (b) Photograph of the QCM head.

are emitted and accelerated by the high voltage towards the material (bismuth in this case) which is in a crucible. The material is heated and the atoms are emitted. Then the atoms fly through the flux monitor, the shutter opening, the nozzle and finally onto the surface of the sample. Figure 4.17 shows a photo with the designation of the important components of the EFM 3 evaporator that was used in the present work. At a certain electron emission current, the ion flux measured at the flux monitor is proportional to the flux of evaporated atoms. However, to determine the absolute amount of evaporated atoms, the EFM 3 must be calibrated. This can be done with the help of a QCM, which is often used to determine the thickness of evaporated layers.

4.2.1.1. Calibration with QCM

The QCM method is based on the measurement of the resonance frequency change of a quartz crystal by the change of the deposited layer thickness on the crystal. Since the frequency change can be measured very accurately, the weighing of the deposited material is thus possible in the range of ng/cm^2 and even below. However, the measurement with QCM is sensitive to the temperature variations on the surface of the crystal and, among other things, to the illumination area of the evaporation beam [118, 119]. This is getting worse when the evaporation rate is in the range below one ML/min . However, QCM is still a fast and relatively simple experimental method, which in combination with e.g. STM measurements provides an accurate calibration of an evaporator.

In order to determine the exact amount of bismuth to be deposited, the evaporation rate was first roughly determined with QCM in a separate UHV facility ²¹. Figure 4.18(b) shows a photograph of the QCM head. The film thickness was defined with $\rho = 9.78 \text{ g}/\text{cm}^3$ for bismuth.

To calibrate the EFM 3 loaded with Bi, a QCM and an XTC control unit 751-001-G1 from INFICON [120] was used.

Figure 4.18(a) shows several calibration runs. Thereby the emission current I_{emis} of the EFM 3 was kept at a constant value of 3 mA. The high voltage was set to 800 V in the heating phase and then left to regulation by the feedback loop of the proportional-integral-differential controller (PID), which then tries to keep the flux at a constant value by adjusting the high voltage (the PID parameters for this calibration

²¹Using the separate small volume UHV facility offers the advantage of more frequent vacuum breaks without requiring extensive baking of the large volume of the surface-science UHV facility.

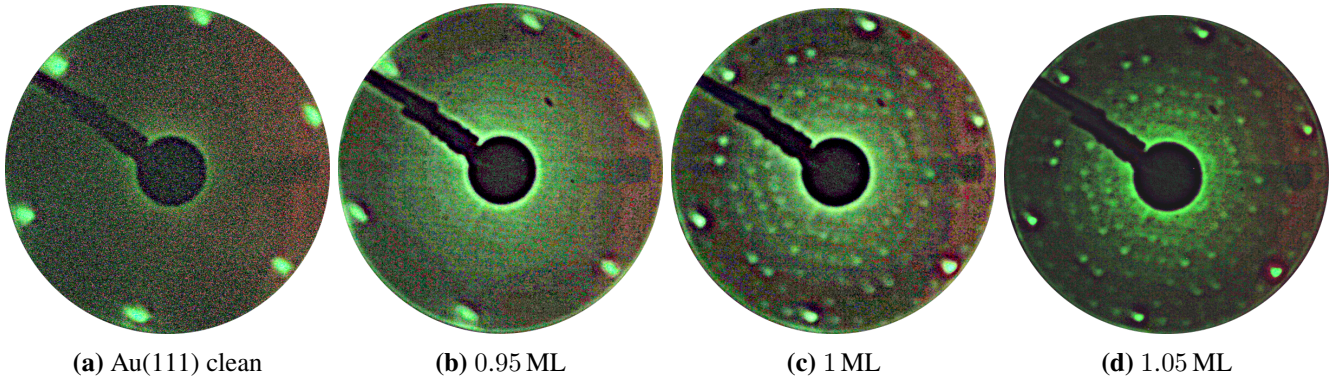


Figure 4.19.: LEED pattern for calibration of the evaporator. (a) Bare Au(111) surface. (b) Au(111) surface with 0.95 ML of Bi deposited. (c) Au(111) surface with 1 ML of Bi deposited. (d) Au(111) surface with 1.05 ML of Bi deposited. All images were taken at 50 eV.

are given in Table 4.6). The fluctuations of the high voltage are usually small (about 5 V to 10 V). The base pressure in the calibration UHV chamber has not exceeded 2.3×10^{-8} mbar in any run.

In all runs the layer growth has a linear characteristic. To determine the rate R_{calib} , the last value of each run is taken and divided by the total time. To estimate the accuracy, 3 s was assumed as an error for the time and the error for the layer thickness is $\pm 0.1 \text{ \AA}$ (results can be found in Table 4.5).

The distance from the QCM to the evaporator in the calibration UHV chamber is different from the distance between the sample and the EFM 3 evaporator in the main UHV chamber, which can be compensated by the inverse square law. This can be used to approximate the amount of deposit in the main UHV chamber as shown in Equation 4.4.

$$R_{\text{main}} \approx R_{\text{calib}} \left(\frac{D_{\text{calib}}}{D_{\text{main}}} \right)^2 = R_{\text{calib}} \left(\frac{84 \text{ mm}}{46.37 \text{ mm}} \right)^2 \approx 3.3 \cdot R_{\text{calib}} \quad (4.4)$$

The aim is to keep the deposition rate as low as possible in order to minimize the aggregation of Bi atoms into larger islands during the deposition process, but not so low that the long duration of deposition would increase the contamination risk. Hence an evaporation rate with a flux current of $I_{\text{flux}} = 70 \text{ nA}$ was chosen (see Table 4.5). The deposition rate in the main UHV chamber therefore is $R_{\text{main}} = (58.7 \pm 0.5) \times 10^{-4} \text{ \AA/s}$.

Table 4.5.: Results of the eight calibration runs (see Figure 4.18) for the estimation of the deposition rates R_{calib} and R_{main} of the EFM 3 evaporator using QCM.

I_{flux}	total time [s]	$R_{\text{calib}} [1 \times 10^{-4} \text{ \AA/s}]$	$R_{\text{main}} [1 \times 10^{-4} \text{ \AA/s}]$
15	1830	3.91 ± 0.55	12.8 ± 0.5
35	1876	9.81 ± 0.53	32.2 ± 0.5
70	2058	17.89 ± 0.49	58.7 ± 0.5
140	737	41.62 ± 1.37	136.6 ± 1.4
200	603	45.78 ± 1.67	150.2 ± 1.7
300	694	72.19 ± 1.47	236.9 ± 1.5
450	702	109.24 ± 1.5	358.5 ± 1.5
550	667	137.97 ± 1.62	452.8 ± 1.6

4.2.1.2. Precision calibration with LEED

In the case of a specific combination of evaporating material and substrate, where the evaporated material wets the surface of the substrate (without additional tempering), the following procedure can be used to refine the calibration:

As a first step, the evaporator is pre-calibrated using QCM to approximate the required amount of the desired material. In the second step, the desired amount of material is deposited using the EFM 3 parameters from the first step. In the final step, a STM measurement is performed and by counting the islands on the surface visible in the STM image, the exact amount evaporated can be determined. Finally, the evaporator parameters can be adjusted, if necessary, and the procedure described above is repeated until the desired amount of material is adsorbed on the surface of the substrate.

However, if the material does not wet the surface, but rather forms three-dimensional islands (as it is the case with $\text{Al}_2\text{O}_3||\text{Ni}_3\text{Al}$ and Bi), then this approach is not very reliable, because the exact distinction between the layers can not be made accurately. In this case, one of the ways to keep these inaccuracies within acceptable limits would be to find a substrate where the evaporating material wets the surface and then perform the deposition and as described above measure/calibrate with STM. However, the STM measurements are time consuming so we used a different approach in the deposition of bismuth, which allows sequential evaporation and fast LEED measurements for the deposited amount of material on the surface. Another reason for using this method is that it is more compatible with UPS. Because STM is a more local method, a large number of STM measurements are required for reliable compatibility with methods that average over microscopic areas.

In the surface-science UHV facility (see Section 2.4), an Au(111) crystal was prepared to have a clean surface. Then Bi was evaporated onto Au(111) in small steps of 0.05 ML using the calibration described in chapter 4.2.1.1. Between the evaporation steps, LEED images were recorded.

At certain points, the LEED image changes drastically (see Figure 4.19). This transition implies a certain coverage of the surface with a pronounced periodicity. After considering the results from several publications [121–123] where bismuth on Au(111) was studied using STM and LEED, this transition can be classified as a coverage of the surface of Au(111) with one ML of bismuth with a periodicity of $(\sqrt{37} \times \sqrt{37})\text{R}25.3^\circ$ in respect to the Au(111) surface. The atomic radius of Au is about 1.44 Å [124], so the interatomic distance is 2.88 Å. The unit vector of the Bi $(\sqrt{37} \times \sqrt{37})\text{R}25.3^\circ$ structure is therefore $\sqrt{37} \cdot 2.88$ Å. The unit cell contains 18 atoms and the angle between the lattice vectors is 60° [121], which is used in the current work to determine a ML as 6.77×10^{14} atoms/cm². Thus the evaporation rate in the main UHV chamber for the deposition of (1 ± 0.05) ML of Bi is $R_{\text{main}} = 12.166$ min/ML. All important parameters of the EFM 3 calibration are summarized in Table 4.6.

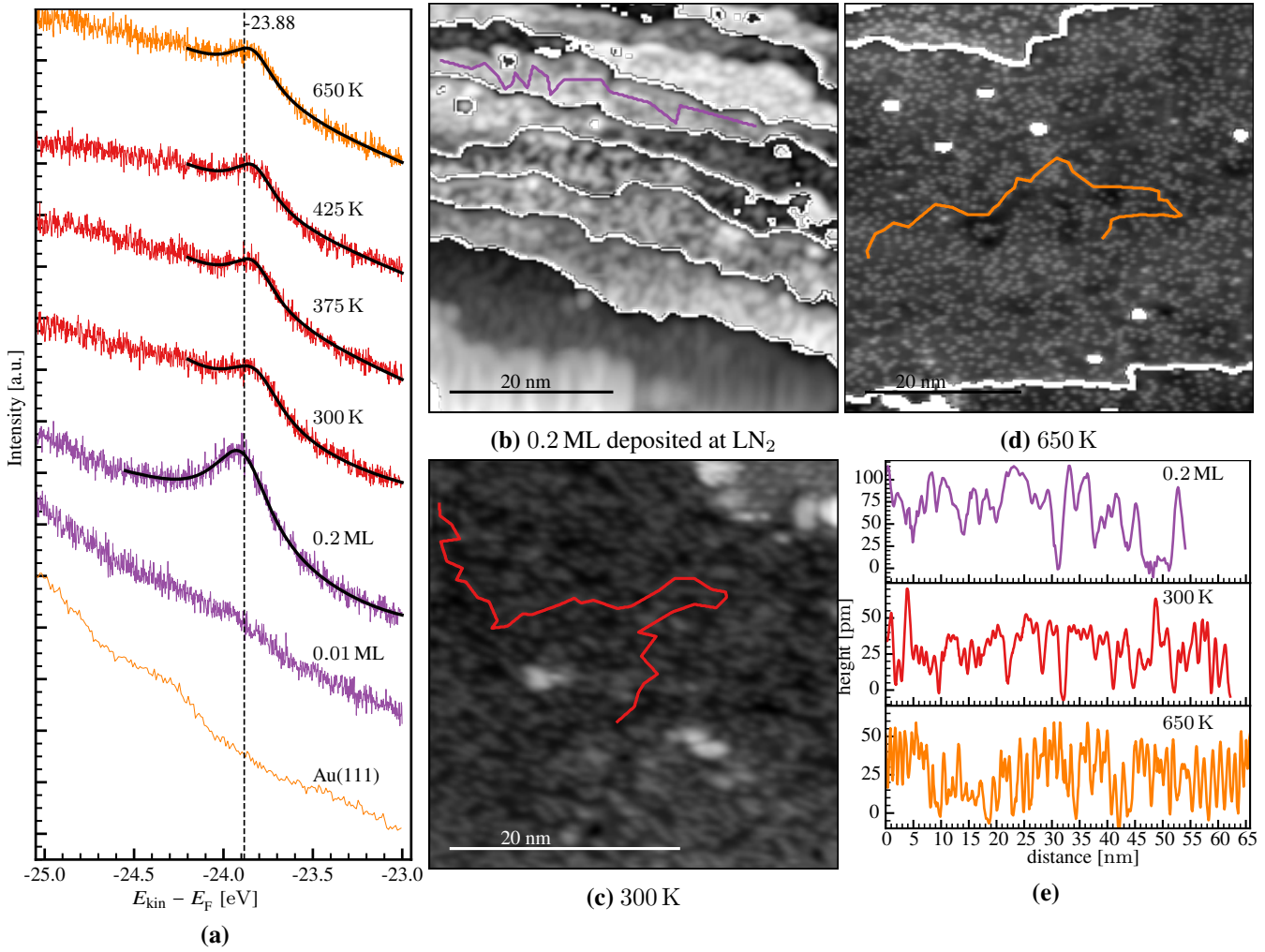


Figure 4.20.: (a) UPS data of the experiments with 0.2 ML Bi||Au(111). Black lines represent Doniach-Sunjić (DS) fits. The corresponding residuals can be found in Appendix B.6, Figure B.9. The fit parameters are shown in the table 4.7. (b), (c) and (d) show STM measurements of 0.2 ML: (b) immediately after deposition, $50 \times 50 \text{ nm}^2$, $U = 2.0 \text{ V}$, $I = 90 \text{ pA}$, (c) after tempering at 300 K, $35.5 \times 35.5 \text{ nm}^2$, $U = 1.65 \text{ V}$, $I = 90 \text{ pA}$ and (d) after last tempering step of 650 K, $52.3 \times 52.3 \text{ nm}^2$, $U = 1.65 \text{ V}$, $I = 90 \text{ pA}$. (e) Height profiles along colored lines shown in (b), (c) and (d).

4.2.2. Bi on Au(111)

With the energy of the HeII α line of 40.81 eV, both outer energy levels of Bi $5d_{3/2}$ at 26.9 eV and $5d_{5/2}$ at 23.8 eV [125] can be excited. In the submonolayer regime the $5d_{3/2}$ level is much weaker in intensity than the $5d_{5/2}$. Therefore, the main focus of the current chapter is on the evolution of the $5d_{5/2}$ core level during the annealing, after deposition of Bi at low temperature on the surface of Au(111).

In order to prepare for the experiments on Al₂O₃||Ni₃Al, several experiments were first carried out for Bi on the Au(111) substrate. Freshly prepared Au(111) was exposed to 0.01 ML of Bi in UHV at **Table 4.6.:** Parameter list of the EFM 3 calibration for bismuth. The upper two rows describe the parameters for the EFM 3 evaporator, where I_{emis} is emission current of the filament, I_{flux} is the flux current and t_{shutter} is the opening time of the shutter. The lower two rows show the parameters for the PID controller.

EFM 3	I_{emis} [mA]	I_{flux} [nA]	t_{shutter} [min]	
	3	70	12.166	
PID	Gain	Delay	Limit up	Limit down
	25	300	75	25

LN₂ temperature. Immediately afterwards, a UPS measurement was carried out. Thereby the HeII α transition line of helium was used for the incident light in UPS measurements. The aim is to study the core level shift of the 5d_{5/2} energy level of Bi, which occurs in bulk Bi at the binding energy of around (23.8 ± 0.2) eV [125] with respect to E_F .

As depicted in Figure 4.20(a), the intensity of the signal from the 5d_{5/2} level in the spectrum of 0.01 ML Bi coverage is notably weak, necessitating extended integration times for obtaining a reliable measurement. This will increase the experimental time and the risk of contamination, so we decided to increase the coverage to 0.2 ML instead.

Deposition and measurements were made at LN₂ temperature. The duration of tempering steps were about 30 min at 300 K, 375 K, 425 K, 550 K and 650 K. After each tempering step a LEED measurement was taken, no changes in the pattern were observed, so these data are not presented here. No UPS data were recorded after tempering at 550 K. Additional STM measurements were taken immediately after deposition and after 300 K and 650 K tempering steps.

Figure 4.20(a) shows the results of UPS measurements in the region of 5d_{5/2} of 0.2 ML of Bi||Au(111). The corresponding fit parameters are given in Table 4.7.

The 5d_{5/2} core level was fitted with the DS line shape convoluted with the Gaussian function²² to compensate for the instrumental broadening, so the width of the Gaussian function was set to a fixed value of the Fermi edge broadening at corresponding temperature of the sample (see Table A.1 in Appendix). Additionally, the α parameter²³ was constrained to the value obtained from the deposition fit (see Table 4.7).

For the background a second order polynomial was used.

The fitting is done simultaneously, so no background presubtraction was performed. This approach is common for analysis of the core levels in XPS [128].

The STM results of the annealing series of 0.2 ML of Bi||Au(111) are depicted in Figures 4.20(b), (c) and (d). For each image, a line profile was extracted along the protrusion structure. The poorly ordered protrusion structure of Bi on the surface of Au(111) is well described in the work of Bingchen He et al. [123]. The author proposed a model of the protrusion structure as $(3 \times 3)_{\text{Bi}}$ on $(5 \times 5)_{\text{Au}}$. The line path in each Figure (see Figure 4.20(b), (c) and (d)) was chosen to minimize the distance between the protrusion peaks. These paths describe the areas on the surface where the protrusion structure is more pronounced

Table 4.7.: Fit parameters of 5d_{5/2} of 0.2 ML Bi after deposition at LN₂ temperature on the surface of Au(111) and several annealing steps. Corresponding spectra are shown in Figure 4.20(a).

	E_B [eV]	α [eV]	2σ [eV]	FWHM [eV]
0.2 ML	-23.884 ± 0.008	0.13 ± 0.04	0.38 ± 0.02	0.45 ± 0.03
300 K	-23.815 ± 0.004		0.35 ± 0.04	0.41 ± 0.05
375 K	-23.825 ± 0.003		0.28 ± 0.02	0.34 ± 0.02
425 K	-23.821 ± 0.004		0.27 ± 0.02	0.32 ± 0.02
650 K	-23.828 ± 0.003		0.29 ± 0.02	0.35 ± 0.02

²²The implementation of the convolution of the DS profile with the Gaussian profile was taken from the “lmfitxps” package [126], which extends the “lmfit” package [127].

²³The α parameter is a component of the convolution of the DS profile with the Gaussian profile, detailed in Appendix A.3

(colored lines in Figures 4.20(b), (c) and (d), corresponding height profiles are shown in Figure 4.20(e)). Although the core level shift of $5d_{5/2}$ level is rather small of about 70 meV, the STM measurements show a drastic change in the form of the protrusion structure of Bi on the surface of Au(111). Immediately after the first annealing step this change is at most noticeable, after the last annealing step the protrusion structure becomes more distinct in the image. Additionally, the distance between the protrusions became shorter, as shown in Figure 4.20(e). For the STM data after the last annealing step (see Figure 4.20(d)), the average peak distance and the average corrected peak height of protrusion structures were calculated²⁴ to (0.8 ± 0.2) nm and (35 ± 11) pm, the results can be found in the Appendix, Figure B.10²⁵. This result, particularly regarding the distance between the protrusions, differs from the findings of Bingchen He and his colleagues, who reported a distance of (1.40 ± 0.05) nm and a height of 40 pm for the protrusions.

To investigate the electronic properties of the outer core level of Bi bulk in more detail, freshly prepared Au(111) was used. Subsequently, 0.5 ML, 1 ML and 11 MLs of Bi were deposited on the substrate at RT.

Figure 4.21(a) shows the results of UPS measurements. The fitting parameters are listed in the Table 4.8. The fitting was performed in the same way as above, but with an additional Voigt line shape component, which is necessary to obtain a good fit and can be related to so-called shake-up satellite. In Figure 4.21(a), the possible shake-up peak is located between $5d_{3/2}$ and $5d_{5/2}$ and is more prominent in the spectrum of 1 ML of Bi.

The shake-up peak may originate from interatomic electron excitation[129, p50] or from charge transfer between ligand and metal orbitals [129, p71]. The latter can be caused by interaction of Au surface atoms with Bi atoms, so the effect becomes weaker with increasing amount of Bi deposited, because the electrons originating from the Bi-Au ligand do not reach the detector.

²⁴With the help of algorithm describe in Appendix A.4

²⁵In fact, the distance distribution shows two peaks at 0.8 nm and 1.1 nm, although the first value is more pronounced.

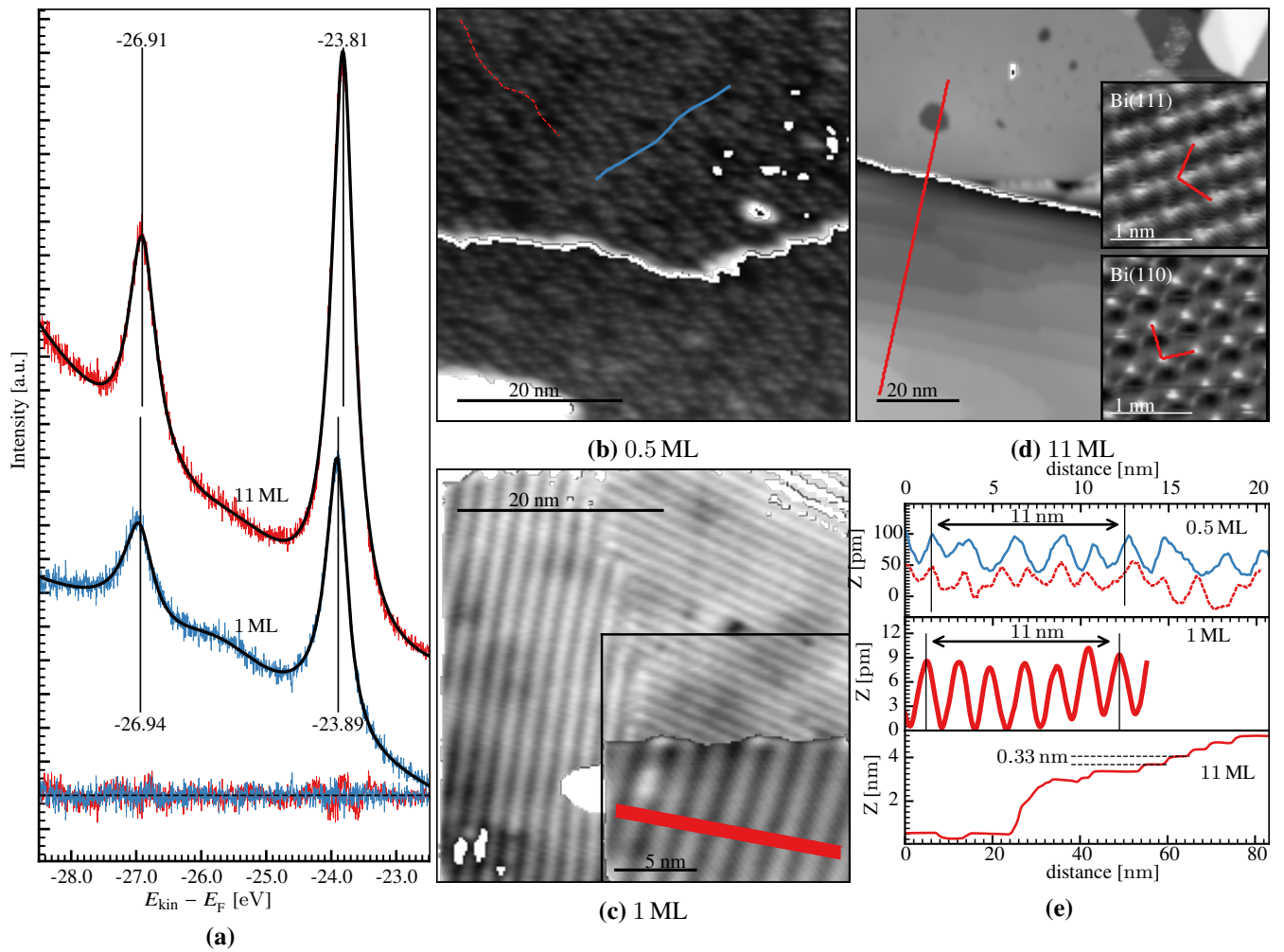


Figure 4.21.: (a) UPS data of the experiment with 1 ML and 11 ML Bi||Au(111). Black lines represent DS fits. The corresponding residuals of the fits are plotted at the bottom. The fit parameters are shown in the table 4.8. (b) 0.5 ML, $50 \times 50 \text{ nm}^2$, $U = 1.65 \text{ V}$, $I = 90 \text{ pA}$, Color maps of the image were manipulated so that the structure on both steps is visible. Average step height is $(0.280 \pm 0.001) \text{ nm}$ (estimated as in Figure 4.5(a)). (c) 1 ML $40 \times 40 \text{ nm}^2$, $U = 1.65 \text{ V}$, $I = 90 \text{ pA}$. (d) 11 ML $100 \times 100 \text{ nm}^2$, $U = 3.2 \text{ V}$, $I = 90 \text{ pA}$. Inset images are bot $2 \times 2 \text{ nm}^2$ with $U = 0.08 \text{ V}$, $I = 140 \text{ pA}$. (e) Collection of profiles shown in (b), (c), (d).

Figures 4.21(b) to 4.21(d) show STM measurements of the subsequent deposition of 0.5 ML, 1 ML and 11 ML of Bi on Au(111) (deposited at RT, measured at LN₂ temperature). Figure 4.21(e) shows a collection of profiles taken from the corresponding STM measurements.

The stripe structure is already evident in the data of 0.5 ML (Figure 4.21(b)). The distance between the peaks along the stripes is about $(1.7 \pm 0.3) \text{ nm}$ for 0.5 ML (indicated by the red dashed line in Figure 4.21(b)), while the spacing between the stripes is about $(2.1 \pm 0.3) \text{ nm}$ (shown by the blue line in Figure 4.21(b)). This is further supported by corresponding line profiles in Figure 4.21(e).

Table 4.8.: Fit parameters of $5d_{5/2}$ of 1 ML and 11 ML of Bi on Au(111). Corresponding spectra are shown in Figure 4.21(a).

1ML	E_B [eV]	α [eV]	2σ [eV]	FWHM [eV]
$5d_{5/2}$	-23.893 ± 0.002	0.12 ± 0.01	0.36 ± 0.01	0.42 ± 0.01
$5d_{3/2}$	-26.936 ± 0.008	0.15 ± 0.03	0.50 ± 0.02	0.62 ± 0.02
11ML	E_B [eV]	α [eV]	2σ [eV]	FWHM [eV]
$5d_{5/2}$	-23.814 ± 0.002	0.04 ± 0.01	0.42 ± 0.01	0.44 ± 0.01
$5d_{3/2}$	-26.908 ± 0.004	0.01 ± 0.01	0.52 ± 0.01	0.52 ± 0.01

With additional deposition of 0.5 ML, leading to a total amount of 1 ML Bi||Au(111), the stripes become more distinct, and the distance between the stripes decreases to (1.6 ± 0.3) nm (see inset in Figure 4.21(c)). The distances between stripes were determined by measuring the distance between several peaks in the line profile (see Figure 4.21(e)) and dividing by the number of peaks in between, with a peak position estimation error of approximately 0.2 nm.

The stripe structure corresponds very well to the $(\sqrt{37} \times \sqrt{37})R25.3^\circ$ structure described in the works of Naoya Kawakami et al. [122] and Bingchen He et al. [123]. The latter reported a distance between the stripes of about (1.42 ± 0.01) nm.

Figure 4.21(d) shows a STM image of the 11 ML of Bi. The red line profile is plotted at the bottom of Figure 4.21(e). The average step height is (0.33 ± 0.04) nm, which is in good agreement with the interlayer spacing of Bi(110) (0.328 nm) [73]. After scanning several terraces across the sample, we were able to find Bi(111) and Bi(110) surfaces, as can be seen from the inset images in Figure 4.21(d), which shows the atomically resolved surface of Bi. In the case of Bi(111), the surface lattice vectors are measured to be 4.604 and 4.589 Å, which are in good agreement with the values of Mönig et al. (4.538 and 4.538 Å) [74].

Unfortunately, the STM data for Bi(110) were strongly drifted, so that a reliable measurement of the lattice vectors is not possible. However, by close analysis of the inset image in Figure 4.21(d), the faint (lower) structures between the brighter (higher) spots can be classified as the second layer of the Bi(110) surface. For this purpose, the data were corrected so that the length of the vectors is equal to 4.731 and 4.538 Å [75]. Raw data, before drift correction, can be found in the Figure B.11 in the Appendix.

In conclusion, after the deposition of Bi on the surface of Au(111), only a minimal shift of the $5d_{5/2}$ core level in the UPS spectra was observed. The center position of $5d_{5/2}$ remains nearly unchanged immediately after deposition, aligning closely with its position in bulk. Here, we assume that the UPS measurement of 11 ML Bi presented in Figure 4.21(a) corresponds to the signal of $5d_{5/2}$ in bulk.

The STM measurements of submonolayer coverage of Au(111) with Bi reveal its unusual electronic configuration on the surface, where we were not able to resolve any separate entities directly after deposition. The surface appears without long-range order. This may be due to the formation of an alloy between Bi and Au atoms.

The STM measurements with 1 ML Bi deposited at RT correspond quite well to the literature and give us confidence that the evaporator calibration (described in Section 4.2.1.2) produces reliable vapor deposition amounts of 1 ML.

While the multilayer data (see Figure 4.21(d)) reveal a mixed state of the Bi atomic arrangement on the surface, predominantly represented by Bi(110) layers. The identification of Bi(110) was achieved through the measured step edges. The clear identification of Bi(111) surfaces is challenging. This difficulty arises due to strong drift in the atomically resolved images, making them potentially unreliable.

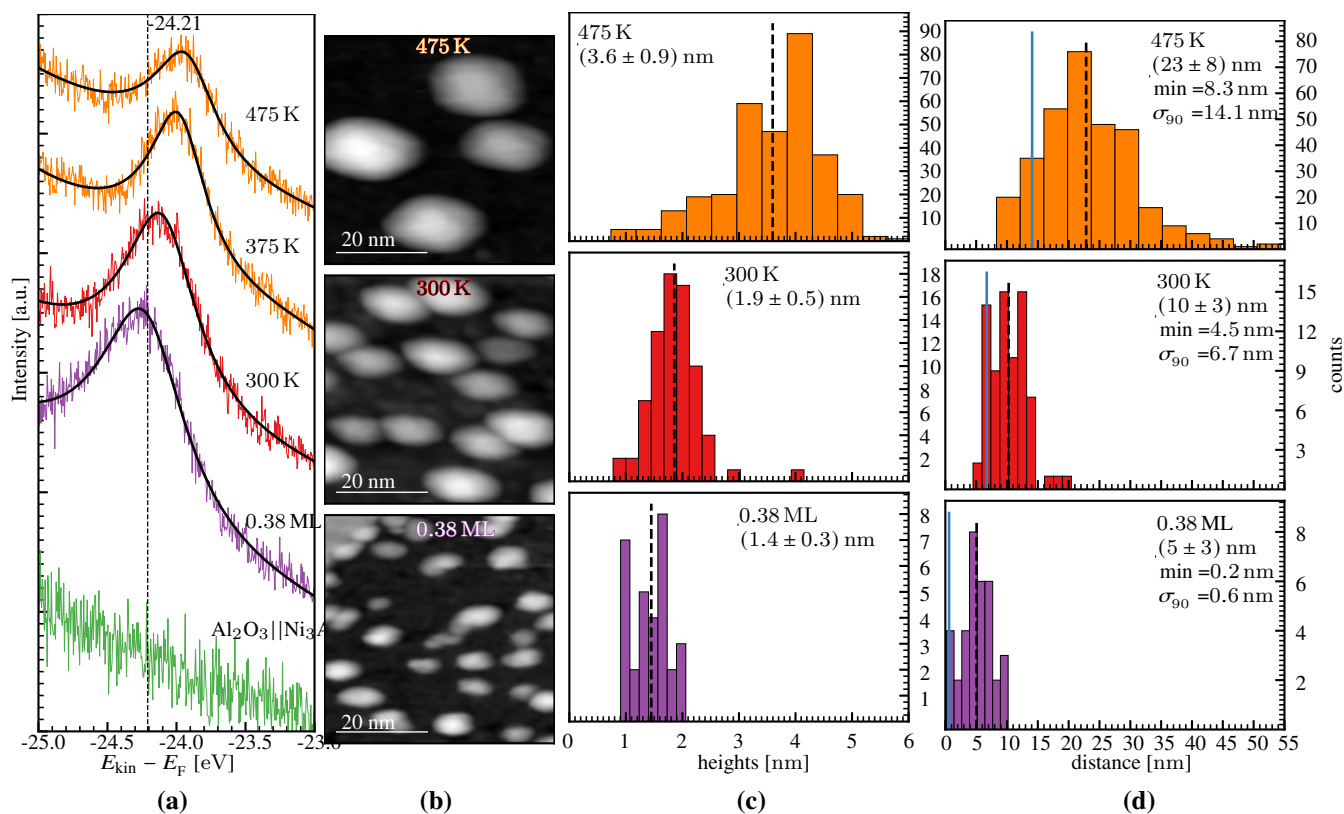


Figure 4.22.: Experimental results of 0.38 ML of Bi deposited on the surface of $\text{Al}_2\text{O}_3||\text{Ni}_3\text{Al}$. Both UPS and STM measurements were conducted at low temperature (LN_2). (a) UPS data show the clean surface of $\text{Al}_2\text{O}_3||\text{Ni}_3\text{Al}$ (bottom green curve), followed by measurements after Bi deposition (labeled as 0.38 ML) and subsequent annealing steps (each denoted with corresponding annealing temperature). The vertical black dashed line indicates the position of the $5d_{5/2}$ peak immediately after deposition at LN_2 . Solid black lines represent the best fit of the DS profile convoluted with Gaussian functions (see Appendix A.3). Fit parameters are detailed in Table 4.9, while residuals of the fits are shown in the Appendix B.7, Figure B.12. (b) Examples for the STM data, with a resolution of 300×300 points and an image size of $50 \times 50 \text{ nm}^2$, depict surfaces after 0.38 ML deposition, as well as after annealing at 300 K and 475 K. All data were recorded with $U = 3.2 \text{ V}$, $I = 90 \text{ pA}$. (c) Height distribution of clusters in the STM data. Heights were determined and corrected to the local environment as described in Appendix A.4. The vertical black dashed line represents the mean of the height distribution, also shown inside the image along with the standard deviation after \pm . The bin width of the histograms is half the standard deviation of each plot. (d) Distance distribution of nearest neighbors. Vertical blue line denotes σ_{90} . 90% of all distances are greater than the σ_{90} value.

4.2.3. Bi on $\text{Al}_2\text{O}_3||\text{Ni}_3\text{Al}$

For the investigation of the aggregation processes of Bi on the surface of $\text{Al}_2\text{O}_3||\text{Ni}_3\text{Al}$ the following two separate experiments were carried out. In both cases the surface of $\text{Ni}_3\text{Al}(111)$ crystal was freshly prepared and Al_2O_3 was built up as described in Chapter 4.1.4.

In the first experiment, 0.38 ML were deposited at LN_2 temperature and gradually annealed at temperatures of 300 K, 375 K and 475 K with the duration of 60 min each. Between the tempering steps UPS and STM measurements were made.

To test whether the core level position of the $5d_{5/2}$ behavior depends on the aggregation process during annealing or on the amount of material deposited, a second experiment was performed. The amount of Bi deposited on the surface of the $\text{Al}_2\text{O}_3||\text{Ni}_3\text{Al}$ at LN_2 temperature was gradually increased from 0.06 ML to 0.1 ML, 0.2 ML, 0.3 ML and 0.5 ML. After the last deposition step, two additional tempering steps were performed at 300 K and 475 K with a duration of about 60 min each. Between the deposition and tempering steps UPS and STM measurements were made²⁶.

²⁶No STM images were acquired after annealing at 375 K.

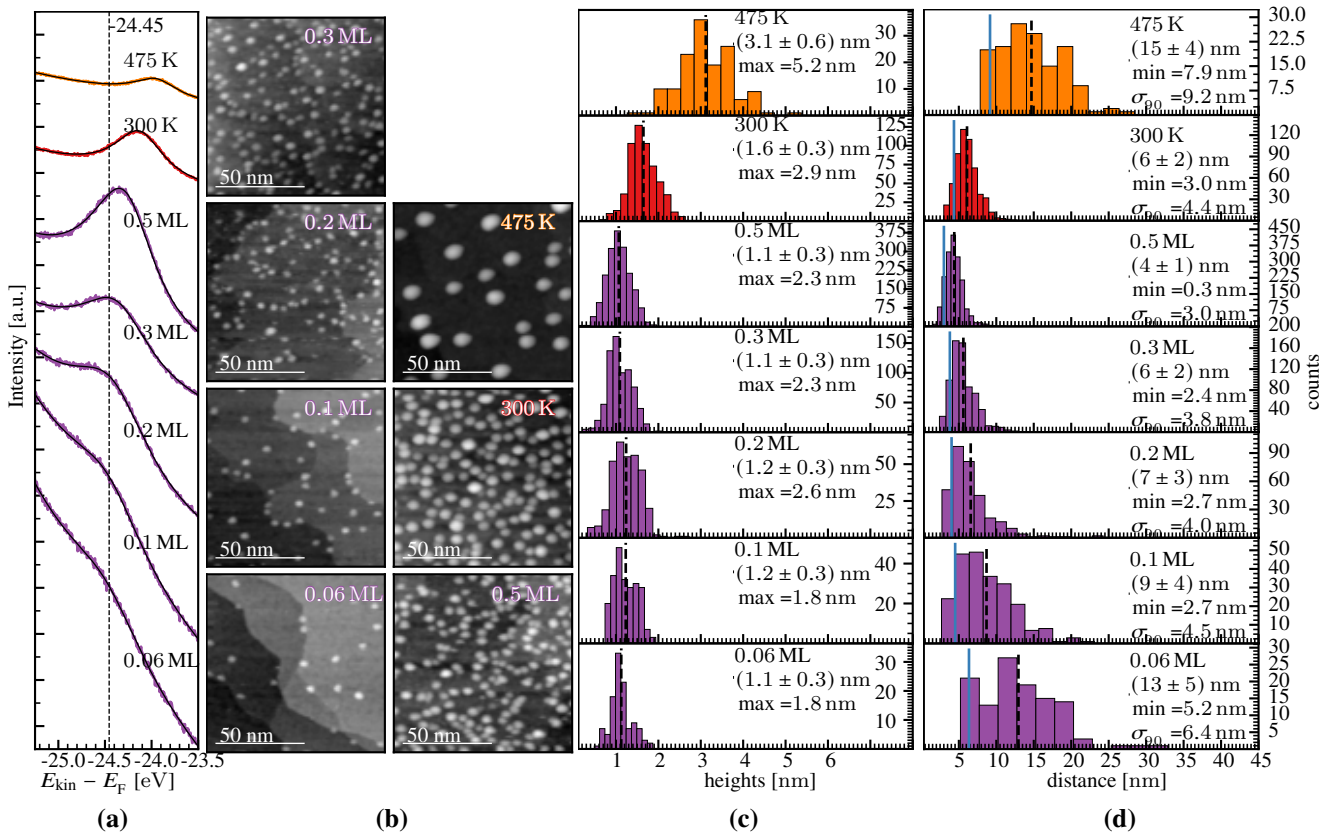


Figure 4.23.: Results of gradual deposition experiments from 0.06 ML to 0.5 ML. The legend is identical to that of Figure 4.22. Except for the resolution and parameters of the STM images in (b). All STM data was recorded with a resolution of 300x300 points and an image size of 100x100 nm². Before 0.3 ML the STM parameters were as in Figure 4.22 U = 3.2 V, I = 90 pA, after 0.3 ML the parameters have to be increased to get stable images up to U = 6.0 V, I = 90 pA (including data for 0.3 ML).

Figure 4.22 shows the results of the experiment with the 0.38 ML of Bi on the surface of Al₂O₃||Ni₃Al. The 5d_{5/2} core level shifts from the initial position of about -24.21 eV to about -23.92 eV during annealing to a higher temperature (Figure 4.22(a) and Table 4.9). The clusters also become larger during annealing, as shown by their height distribution (see Figures 4.22(b) and 4.22(c)). The average height after deposition is (1.4 ± 0.3) nm and after the last annealing step (3.6 ± 0.9) nm. Which means a total energy shift of about (0.294 ± 0.009) eV, while the height of the clusters increases by about 2.4 nm on average. The average distance between the clusters also increases from about (5 ± 3) nm to (23 ± 8) nm on average (see Figure 4.22(d)).

Figure 4.23 shows the results of the experiment with gradually increasing amount of Bi on the surface of Al₂O₃||Ni₃Al from 0.06 ML to 0.5 ML and two additional tempering steps of 300 K and 475 K for 0.5 ML of Bi.

The energy shift of the 5d_{5/2} level during the increase of the deposition amount is about (0.20 ± 0.02) eV

Table 4.9.: Fit parameters of 5d_{5/2} core level peaks of 0.38 ML Bi||Al₂O₃||Ni₃Al after deposition at LN₂ temperature and several annealing steps. Corresponding spectra are shown in Figure 4.22(a).

	E_B [eV]	α [eV]	2σ [eV]	FWHM [eV]
0.38 ML	-24.209 ± 0.008	0.14 ± 0.02	0.71 ± 0.02	0.85 ± 0.02
300 K	-24.082 ± 0.003		0.60 ± 0.02	0.72 ± 0.02
375 K	-23.967 ± 0.003		0.46 ± 0.01	0.55 ± 0.02
475 K	-23.915 ± 0.005		0.51 ± 0.02	0.61 ± 0.03

(from -24.45 eV to -24.25 eV), while between the last deposition step of 0.5 ML and the last annealing step the energy shift increases by (0.313 ± 0.006) eV (from -24.25 eV to -23.94 eV).

According to the STM data (Figure 4.23(b) and (c)), there is almost no increase in height between the deposition amounts of 0.06 ML and 0.5 ML. After annealing, the height increases from (1.1 ± 0.3) nm to (3.1 ± 0.6) nm. So the total height shift is about 2 nm on average.

Analysis of the distance between clusters (see Figure 4.23(d)) shows that as the amount of Bi deposited increases, the average distance between clusters decreases, indicating the formation of new clusters. As there is no significant increase in cluster heights, this could mean that Bi clusters on the surface of $\text{Al}_2\text{O}_3||\text{Ni}_3\text{Al}$ deposited at LN_2 temperature have a preferred stable height of about 1 nm to 1.2 nm during deposition, which then increases to about 3 nm, while the distance between clusters increases during annealing²⁷.

Another notable feature of the cluster distribution (see Figure 4.23(d)) is the absence of "short" distances between clusters. For each sample in Figure 4.23, the shortest distance between neighboring clusters is almost always greater than 2.6 nm. Except for the sample of 0.5 ML in Figure 4.23(d), where the shortest distance is about 0.3 nm and is very likely caused by the STM image artifacts that were misdetected by the algorithm. The distance distribution plot for the deposition of 0.38 ML at the bottom of the Figure 4.22(d) also shows no "gap" at short distances, which is almost certainly due to the quality of the STM measurement.

However, the "absence" of short distances in almost all STM measurements could indicate a preference for network structure sites, as described in the work of Becker et al. [130] where they examined the growth of Ag and Mn clusters on $\text{Al}_2\text{O}_3||\text{Ni}_3\text{Al}$ and were able to show the pinning of cluster growth to the network and dot structure.

Also in the work of Dominik Wolter [63] the mass selected Cu clusters show a tendency to organize along the ordered structure rather than distribute randomly on the surface of the $\text{Al}_2\text{O}_3||\text{Ni}_3\text{Al}$.

In conclusion, after the deposition of Bi on the surface of $\text{Al}_2\text{O}_3||\text{Ni}_3\text{Al}$ at LN_2 temperature and subsequent annealing at higher temperatures, the $5d_{5/2}$ level shifts by about 300 meV towards the E_F . Additionally, the clusters become larger, and the distance between clusters increases, indicating cluster growth caused by Ostwald ripening (see Section 2.2.2).

Table 4.10.: Fit parameters of $5d_{5/2}$ of 0.06 ML - 11 ML Bi after deposition at LN_2 temperature on the surface of $\text{Al}_2\text{O}_3||\text{Ni}_3\text{Al}$ and several annealing steps. Corresponding spectra are shown in Figure.

	E_B [eV]	α [eV]	2σ [eV]	FWHM [eV]
0.06 ML	-24.45 ± 0.02	0.17 ± 0.04	1.06 ± 0.04	1.37 ± 0.09
0.1 ML	-24.444 ± 0.003	0.15 ± 0.01	1.01 ± 0.01	1.25 ± 0.01
0.2 ML	-24.393 ± 0.006	0.18 ± 0.01	0.97 ± 0.02	1.28 ± 0.04
0.3 ML	-24.342 ± 0.005	0.17 ± 0.01	0.87 ± 0.01	1.12 ± 0.02
0.5 ML	-24.251 ± 0.004	0.20 ± 0.01	0.78 ± 0.01	1.09 ± 0.03
0.5 ML 300 K	-24.127 ± 0.003	0.05 ± 0.01	0.68 ± 0.01	0.72 ± 0.01
0.5 ML 475 K	-23.938 ± 0.004	0.11 ± 0.01	0.54 ± 0.01	0.62 ± 0.01

²⁷The difference in heights for 0.38 ML in the first experiment and 0.3/0.5 ML in the second experiment could be caused by the different tunneling parameters ($U = 3.2$ V vs. $U = 6.0$ V).

During the increase of the deposited amount, the energy position of $5d_{5/2}$ is shifted by almost the same amount as after annealing, but the height of the clusters does not change on average, at least not to the same extent as during annealing. This effect is likely caused by the STM probe's inability to resolve the lateral extent of the high clusters, as mentioned in Figure 2.11.

The energy shift of $5d_{5/2}$ could be explained (as we propose in Section 4.2.4) by a model describing an decrease in charging energy (as defined in Section 4.1.5 and in Figure 4.16) due to an increase in cluster size. This model will be presented and discussed in the following section.

4.2.4. Discussion

In section 4.1.5, when defining the charging energy of C_{60} , we utilized the fact that individual C_{60} molecules and C_{60} s within a monolayer share the same shape. Consequently, there is no energy shift of the HOMO originating directly from the C_{60} molecule or from the substrate, allowing us to study the energy shift based solely on the contribution from neighboring molecules.

Bi clusters undergo changes in size as they grow, necessitating an approximation of the energy shift originating directly from the clusters, where the volume of the clusters plays a crucial role. In addition, the varying sizes of the Bi clusters at different annealing stages make the surface contribution significant, in contrast to the case of C_{60} molecules.

As mentioned above, the STM probe usually provides false lateral resolution of high clusters on the surface in contrast to the flat surface (see Figure 2.11). Therefore, when discussing the size of clusters in the context of STM measurements, an appropriate lateral size correction should always be made.

In a first approximation, clusters can be considered as microscopic metallic droplets [131]. So in this scenario, classical electrostatics can be applied. The representation of clusters can be simplified by approximating them as perfect spheres with a radius R_{cl} equal to half their height h . Assuming that the density of these spherical clusters mirrors that of the bulk material (ρ_{Bi}), we can employ equation (4.5) to determine the number of atoms per spherical cluster²⁸ (N_{cl}^{sph}).

$$N_{cl}^{sph} = V_{sph} \frac{\rho_{Bi}}{M_{Bi}} = \frac{4}{3} \pi R_{cl}^3 \frac{\rho_{Bi}}{M_{Bi}} = \frac{4}{3} \pi \left(\frac{h}{2} \right)^3 \frac{\rho_{Bi}}{M_{Bi}} \quad (4.5)$$

Where M_{Bi} is the atomic mass of bismuth. By iterating over all cluster heights in a sample, and subsequently dividing by the total area (A_{tot}) measured across all STM images for that sample, we can derive an estimate for the average number of atoms per area unit (N_{cl}^{sph} / A_{tot}).

As described in section 4.2.1.2, the estimation of the deposited amount of Bi is relatively precise due to the used method of determination of 1 ML (the error is 5%). Therefore, by comparing this number with the average number of atoms per area (N_{cl}^{exp} / A_{tot}) estimated from the deposition time, it can be seen that the assumption of the clusters as spheres underestimates the number of deposited atoms (see Table 4.11). Note that the N_{cl}^{sph} number shows a "jump": the value of $N_{cl}^{sph} / N_{cl}^{exp}$ for 0.3 ML is equal to that for 0.06 ML coverage. This is due to STM measurements made at higher gap voltages, as indicated by the gray-marked rows in the table. The height value of the sample with 0.3 ML coverage is probably higher due to the underestimation of the cluster size by scanning with a higher gap voltage, as described in the work of Ingo Barke [132, p.7, fig. 4].

The value of N_{cl}^{sph} at 0.3 ML is more likely to be in the range of the value of the 0.38 ML sample, since the coverage is in a similar range.

In Section 4.2.2, where Bi has been deposited onto the surface of metal (Au(111)), it exhibits wetting behavior and forms a distinct structure. However, in the case of $Al_2O_3||Ni_3Al$, no evidence suggests

²⁸Since the ML definition was made by defining the atoms per area quantity, calculating the cluster volume in terms of atoms is more convenient.

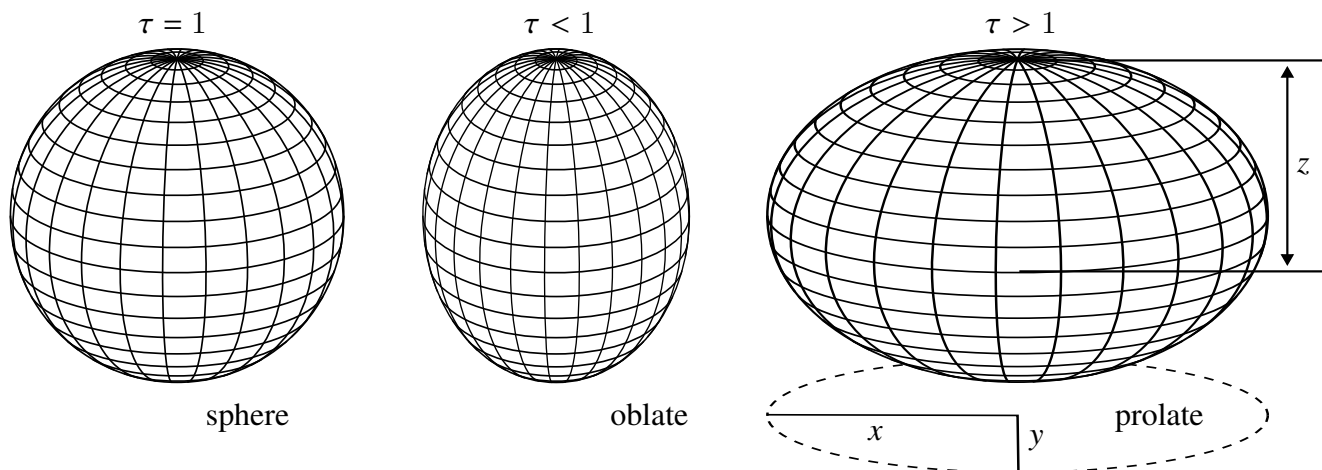


Figure 4.24.: Representation of the cluster as a sphere (left), as an oblate ellipsoid with $\tau < 1$ (middle), and as a prolate ellipsoid with $\tau > 1$ (right).

that Bi wets the surface. Consequently, it is reasonable to assume that Bi atoms aggregate into clusters rather than forming a continuous layer on the surface during deposition. Under this assumption, we can infer that the clusters likely adopt an ellipsoidal shape²⁹ [132]. Therefore, we can calculate the number of atoms inside the ellipsoid N_{cl}^{ell} in a manner analogous to equation (4.5):

$$N_{cl}^{ell} = V_{ell} \frac{\rho_{Bi}}{M_{Bi}} = \frac{4}{3} \pi \cdot x \cdot y \cdot z \cdot \frac{\rho_{Bi}}{M_{Bi}} \quad (4.6)$$

x , y and z are the half-axes of the ellipsoid (see Figure 4.24).

From STM images, the precise shape of clusters cannot be determined conclusively. Specifically, we cannot ascertain whether the clusters exhibit uniformity or if they are more distorted along one of the axis of the ellipsoid. Therefore, for the sake of simplification, we make the assumption that both axes of the ellipsoid, which are parallel to the surface, are of equal length. Furthermore, we introduce a distortion factor τ to scale between the half axes x , y and z as $x = y = \tau z$ with $z = h/2$, h represents cluster height.

Table 4.11.: Estimation of the number of atoms per area by assuming the clusters to be perfect spheres. Rows marked in gray indicate STM measurements with a higher gap voltage of 6.0 V.

sample	$N_{cl}^{sph} / A_{tot} \times 10^{14} [\text{cm}^{-2}]$	$N_{cl}^{exp} / A_{tot} \times 10^{14} [\text{cm}^{-2}]$	$N_{cl}^{sph} / N_{cl}^{exp}$
0.38 ML	0.49	2.53	0.19
300 K	0.4	2.53	0.16
475 K	0.51	2.53	0.2
0.06 ML	0.05	0.41	0.12
0.1 ML	0.13	0.68	0.19
0.2 ML	0.21	1.35	0.16
0.3 ML	0.24	2.02	0.12
0.5 ML	0.43	3.38	0.13
300 K	0.87	3.38	0.26
475 K	1.10	3.38	0.33

²⁹According to Barke [132], a truncated sphere model would be more appropriate in the case of wetting of the surface, but this is probably only applicable for the mass-selected or "preformed" clusters.

Therefore the equation (4.6) becomes:

$$N_{cl}^{ell} = \frac{1}{6} \pi \tau^2 h^3 \frac{\rho_{Bi}}{M_{Bi}} \quad (4.7)$$

To determine the average deformation τ , we have to solve equation (4.8) for each cluster with the height h_i in every sample.

$$N_{cl}^{exp} (t_{evap}) - \sum_{i=1}^N N_{cl}^{ell} (\tau, h_i) = 0 \quad (4.8)$$

Distortion factors τ for both experiments described in Sections 4.2.3 are shown in Table 4.12.

Table 4.12.: Results of the estimation of the deformation factor τ and the energy shifts of the core level for the spherical model ΔE_{cl}^{sph} and the ellipsoidal model ΔE_{cl}^{ell} . For better visibility, the error is displayed in brackets of the last digit: e.g. 1.2(2) means 1.2 ± 0.2 . Rows marked in gray indicate STM measurements with a higher gap voltage of 6.0 V. As mentioned above, the change in the gap voltage has an effect on the measurements for the sample of 0.3 ML, so that the value of τ is overestimated and is probably in the range of the value of the sample denoted with 0.38 ML.

sample	t_{evap}	τ	ΔE_{cl}^{sph}	ΔE_{cl}^{ell}	sample	t_{evap}	τ	ΔE_{cl}^{sph}	ΔE_{cl}^{ell}
					0.06 ML	00:44	2.57(1)	1.3(3)	0.6(1)
					0.1 ML	01:13	2.00(1)	1.2(4)	0.7(2)
					0.2 ML	02:26	2.15(1)	1.2(4)	0.7(2)
					0.3 ML	03:38	2.45(2)	1.3(4)	0.7(2)
0.38 ML	04:33	1.99(2)	1.1(3)	0.6(3)	0.5 ML	06:04	2.44(3)	1.1(3)	0.7(2)
300 K	04:33	2.19(2)	0.8(3)	0.5(3)	300 K	06:04	1.54(2)	0.8(2)	0.6(3)
475 K	04:33	1.94(2)	0.4(2)	0.3(2)	475 K	06:04	1.68(2)	0.4(1)	0.3(1)

4.2.4.1. Charging energy of Bi clusters

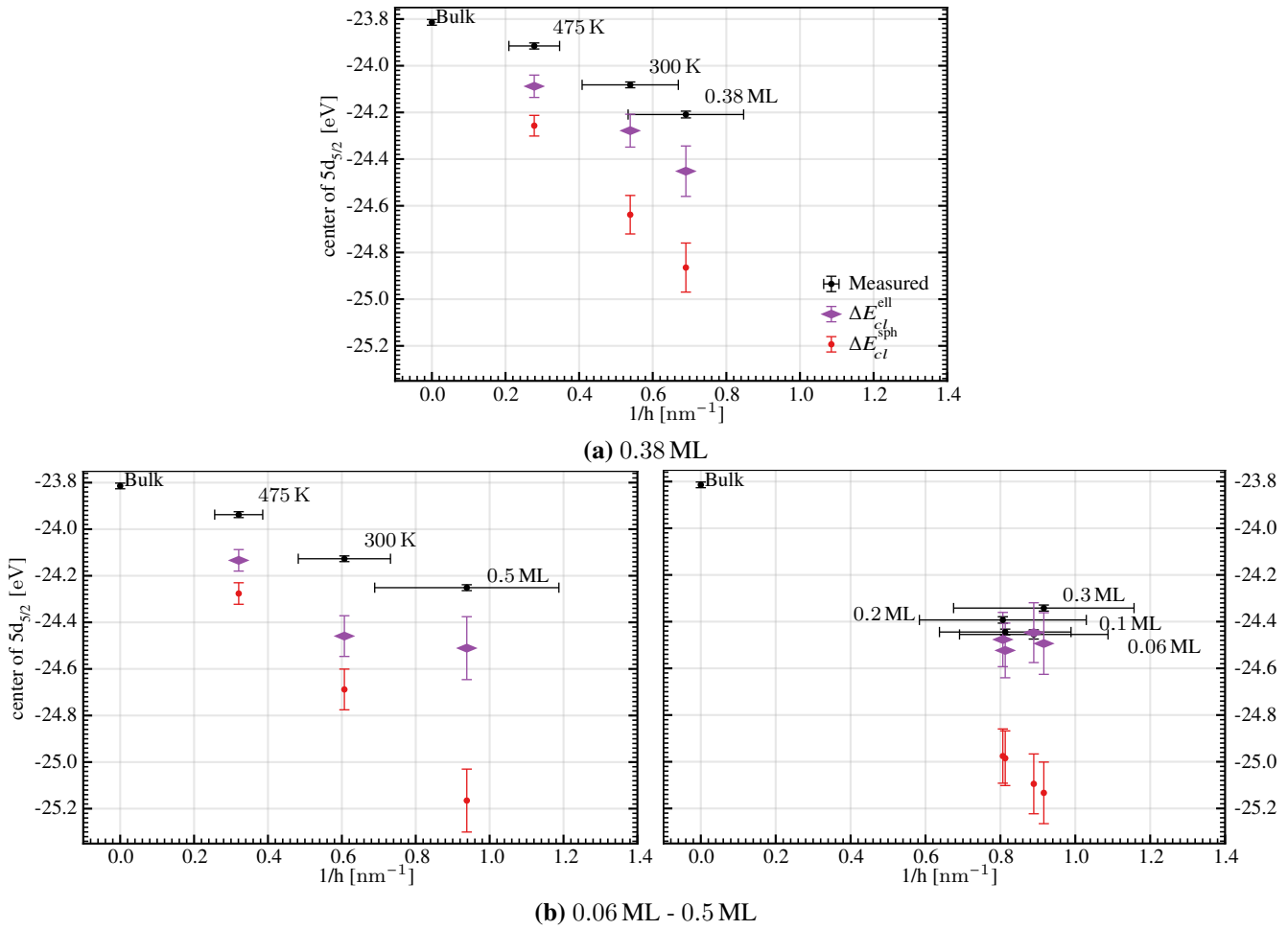


Figure 4.25.: Energy peak position of the Bi core level as a function of the reciprocal mean cluster height for each sample. ΔE_{cl}^{sph} and ΔE_{cl}^{ell} represent the energy shift of the core level with respect to the bulk value estimated from the spherical and ellipsoidal models. For clarity, the error of the mean heights is given only for the measured data and is exactly the same for all models. Also for the second experiment, the deposition steps from 0.06 ML to 0.3 ML are plotted separately for better clarity.

For the charging energy, we will consider the ionization potential of metal clusters as a function of their size [133], as commonly employed in the description of experiments in cluster physics [134].

Equation 4.9 describes the change in the ionization potential of spherical metal cluster relative to the bulk material in dependency of the cluster radius R_{cl} .

$$IP(R_{cl}) = W_{\infty} + \alpha \frac{e^2}{4\pi\epsilon_0 (R_{cl} + \delta)} \quad (4.9)$$

Here, W_{∞} describes the work function of the bulk, δ represents the radius correction due to the electron “spill-out” into the vacuum, and α stands for a quantum correction factor of the bulk work function for a spherical particle [134]. According to Seidel [133], the α and δ corrections are only valid for metals with r_s ³⁰ between 2 and 6. With the r_s of 2.25 for Bi, we are approaching the boundary of the validity range. Furthermore, we have not been able to find any theoretical calculations in the stabilized jellium model explicitly for Bi. Therefore, we will consider the classical case with $\delta = 0$ and $\alpha = 1/2$.

³⁰Here the r_s radius is normalized to the Bohr radius (a_0).

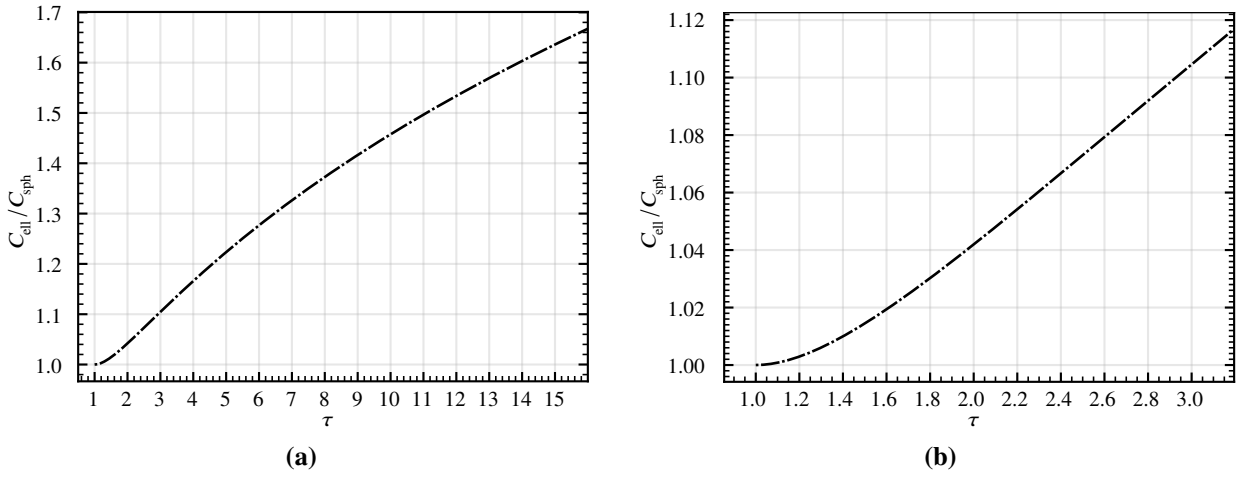


Figure 4.26.: Ratio of the capacity of ellipsoidal and spherical models as a function of the distortion factor τ (see Equation 4.17). (a) in the range between 0 and 15 and (b) in the corresponding range of the measured data.

By considering the difference in ionization potential to be uniformly transferable as a shift of the core level, at least in the first approximation, as it has already been used for the shift of the d-band structure of clusters [135], we can define³¹ ΔE_{cl} to be the shift of the core level due to the bulk value:

$$\Delta E_{cl}^{\text{sph}} := \text{IP}(R_{cl}) - W_{\infty} = \frac{1}{2} \cdot \frac{e^2}{4\pi\epsilon_0 R_{cl}} \quad (4.10)$$

In the classical case, the expression $4\pi\epsilon_0 R_{cl}$ represents the capacitance of the sphere C_{sph} ; to incorporate the deformation of spherical metallic Bi clusters into oblate ellipsoids, as discussed above, we can simply replace the capacitance of a sphere by the capacitance of an oblate ellipsoid C_{ell} [136, p.36]:

$$\Delta E_{cl}^{\text{ell}} = \frac{1}{2} \cdot \frac{e^2}{C_{\text{ell}}} \quad \text{with} \quad C_{\text{ell}} = 4\pi\epsilon_0 \frac{\sqrt{x^2 - z^2}}{\frac{\pi}{2} - \arctan\left(\frac{z}{\sqrt{x^2 - z^2}}\right)} \quad \text{and} \quad x = y = \tau z, \quad z = h/2. \quad (4.11)$$

With the help of τ from Table 4.12 ΔE_{cl} can be calculated and is also shown in Table 4.12.

Figure 4.25 shows the correlation between the reciprocal mean height of the clusters and the peak energy position of the core level. The corrections for the spherical (marked with $\Delta E_{cl}^{\text{sph}}$) and ellipsoidal ($\Delta E_{cl}^{\text{ell}}$) models are plotted and represent the energy shift in respect to the bulk value. As shown in Figure 123, the ellipsoidal model reproduces the energetic shifts of the core level more accurately than the spherical model. However, the deviations from the measured values are still larger than the uncertainties. Therefore, further adjustments are needed.

The volume of the clusters plays an important role; the deformation factor (τ) in Table 4.12 and Figure 4.25 is essentially related to the volume increase of the ellipsoidal clusters. However, τ is a relatively small number, which raises the question: how significant is the influence of the deformation factor on the capacity values of the clusters when comparing ellipsoidal clusters to spherical clusters of the same volume as the ellipsoidal ones?

³¹ ΔE_{cl} is the shift caused by charging energy U_0 of clusters.

The volume of the spherical cluster is given by the well-known formula for the volume of a sphere:

$$V_{\text{sph}} = \frac{4}{3}\pi z_{\text{sph}}^3. \quad (4.12)$$

The volume of the ellipsoidal cluster with the deformation factor τ is:

$$V_{\text{ell}} = \frac{4}{3}\pi\tau^2 z_{\text{ell}}^3. \quad (4.13)$$

Equal volume implies the following expression:

$$z_{\text{ell}} = \tau^{-\frac{2}{3}} z_{\text{sph}} \quad (4.14)$$

By inserting the capacitance of the sphere:

$$C_{\text{sph}} = 4\pi\epsilon_0 z_{\text{sph}} \quad (4.15)$$

and the capacity of the ellipsoid:

$$C_{\text{ell}} = 4\pi\epsilon_0 \frac{\sqrt{\tau^2 - 1}}{\pi/2 - \arctan\left(1/\sqrt{\tau^2 - 1}\right)} z_{\text{ell}} \quad (4.16)$$

in equation 4.14, the ratio of the capacitance can be expressed as:

$$\frac{C_{\text{ell}}}{C_{\text{sph}}} = \frac{\sqrt{\tau^2 - 1}}{\pi/2 - \arctan\left(1/\sqrt{\tau^2 - 1}\right)} \tau^{-\frac{2}{3}} \quad (4.17)$$

Figure 4.26 shows the evolution of the capacitance ratio with τ .

The increase of C_{ell} compared to the equal volume sphere is relatively small. Even for the extreme case of $\tau = 11$ it increases by less than 50%. The relevant range for the experiments discussed in the current work is between $\tau = 1$ and 3 (as shown in Figure 4.26(b)). Thus, the increase is < 12%. In terms of accuracy, this is probably in the range of the calibration error of STM, where we can approximate oblate clusters with the sphere of equal volume.

This is shown with the symbols $\Delta E_{cl}^{\text{sph,eq}}$ in Figure 4.28. Using $\Delta E_{cl}^{\text{sph,eq}}$ it is possible to include the conducting substrate into the model (see next section).

4.2.4.2. Substrate contribution

As in the previous chapter, the contribution of the substrate is considered here in the classical approximation. For the system of clusters on the surface of $\text{Al}_2\text{O}_3||\text{Ni}_3\text{Al}$ we extend this classical approach considering a sphere over a conducting surface. With the help of the image charges one can derive the expression for the capacitance of a sphere over a conducting surface (equation 4.18) as a function of the distance between the center of the sphere and surface d , and the sphere radius r [137] (see Figure 4.27(a)).

$$C_{\text{surf}}(d, r) = 4\pi\epsilon_0 r F \left[\cosh^{-1}(d/r) \right] \quad (4.18)$$

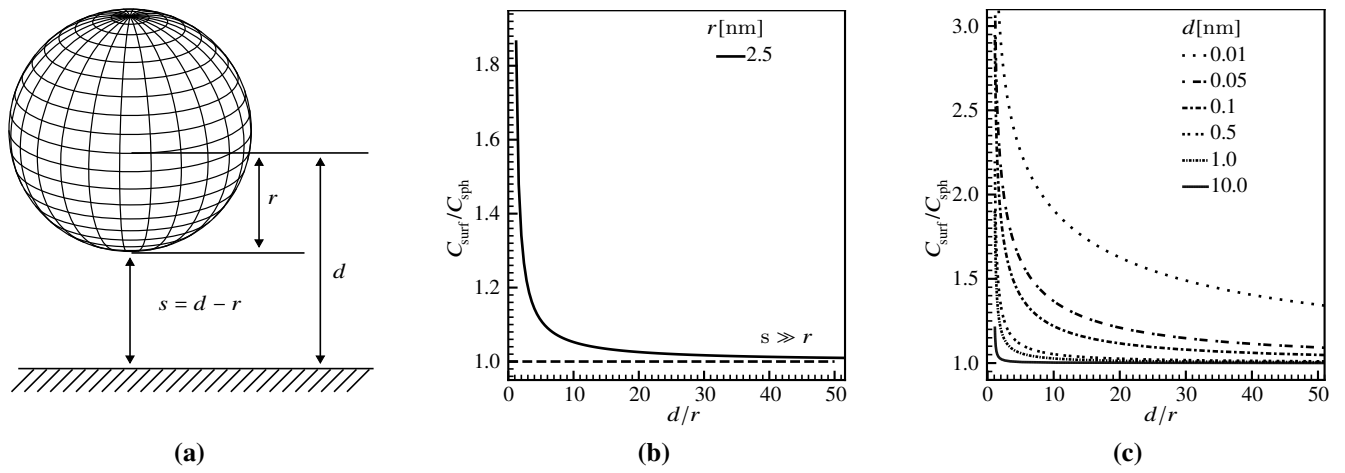


Figure 4.27.: (a) Model of the sphere over a conducting surface. (b) Dependence of the capacitance of the sphere over a conducting surface on the distance between the sphere and the surface. (c) Same as (b), but for very small distances.

with :

$$F(\xi) = \sinh(\xi) \sum_{n=0}^{\infty} \frac{1}{\sinh[(n+1)\xi]} \quad (4.19)$$

For very large distances (s) between the sphere and the surface ($s \gg r$), the capacitance C_{surf} became the capacitance of the isolated sphere (C_{sph}), as can be seen in Figure 4.27(b).

The capacitance exhibits a logarithmic relationship with distance as the gap between the sphere ($s = d - r$) and the surface diminishes [137]:

$$C_{\text{surf}}(d, r) \sim -\ln(s), \quad \text{for } s \rightarrow 0 \quad (4.20)$$

With this model, the approximation of the surface's contribution to the total core level energy shift in UPS spectra becomes feasible. To perform this estimation, the energy shift is calculated using Equation 4.21. The capacitance C_{surf} is computed following Equation 4.18, where the radius of the sphere is adjusted to match the volume of the corresponding ellipsoid. The distance between the cluster and the surface is estimated to be the thickness of the double layer of Al_2O_3 , which is approximately 0.5 nm ³². In this setup, the $\text{Ni}_3\text{Al}(111)$ serves as the conducting surface. Error analysis is conducted through error propagation, with the error propagation of $C_{\text{surf}}(d, r)$ detailed in the Appendix A.5.1.

$$\Delta E_{cl}^{\text{surf}} = \frac{1}{2} \cdot \frac{e^2}{\left(C_{\text{ell}}/C_{\text{sph}}\right) \cdot C_{\text{surf}}} \quad (4.21)$$

The factor $\left(C_{\text{ell}}/C_{\text{sph}}\right)$ corrects for the disparity in capacitances between the sphere and ellipsoid, as described above (refer to Equation 4.17).

³²An error margin of 10 % was considered to account for potential variations in the oxide layer thickness.

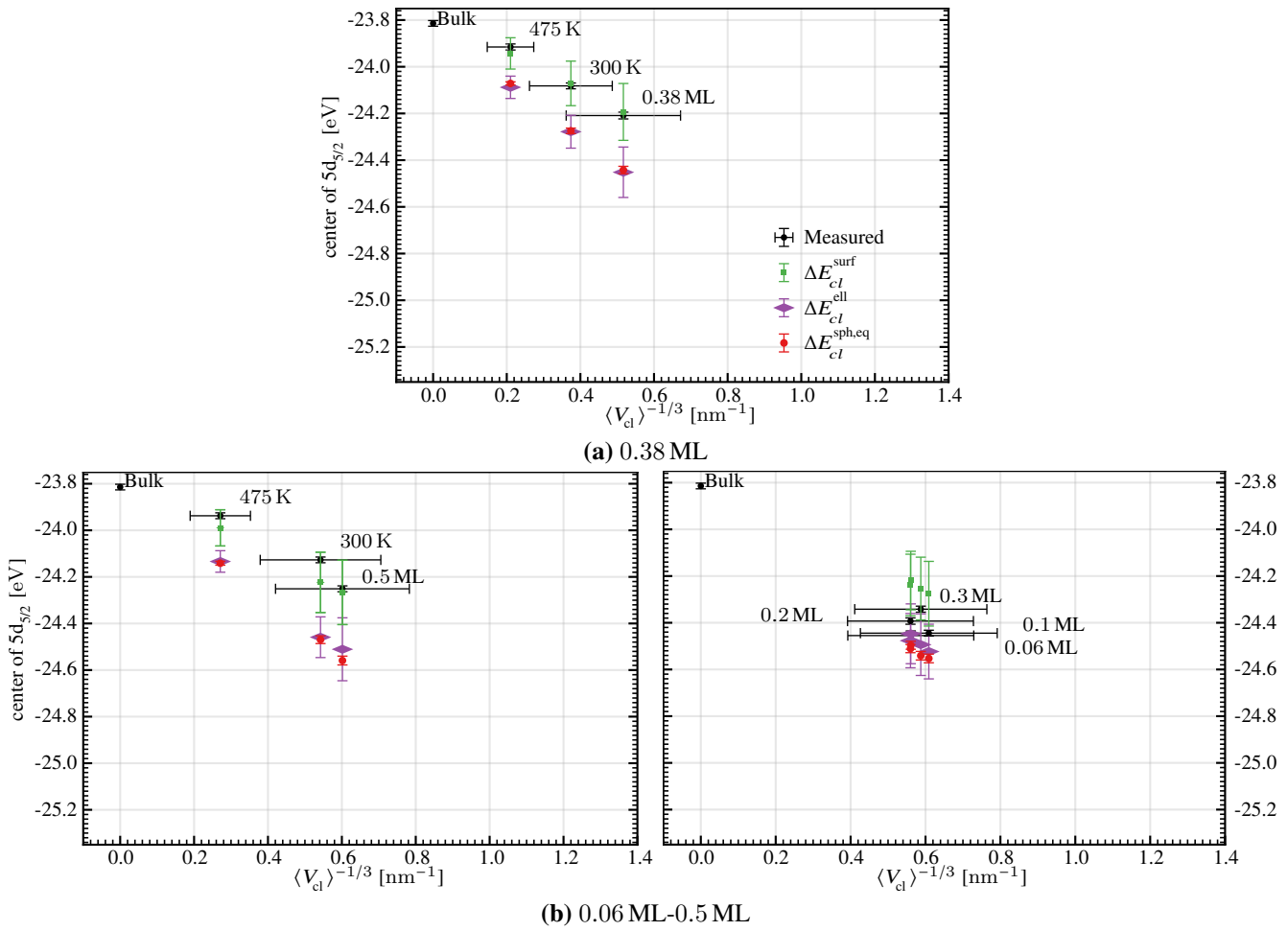


Figure 4.28.: Energy peak position of the Bi core level as a function of the reciprocal mean cluster volume $\langle V_{cl} \rangle^{-1/3}$ for each sample. ΔE_{cl}^{sph} and ΔE_{cl}^{ell} represent the energy shift of the core level with respect to the bulk value estimated from the spherical and ellipsoidal models and ΔE_{cl}^{surf} is the energy shift due to the approximation of clusters on the surface of $\text{Al}_2\text{O}_3||\text{Ni}_3\text{Al}$ by a metallic sphere over the conducting surface. For the second experiment, the deposition steps from 0.06 ML to 0.3 ML are plotted separately for better clarity.

The capacitance of the sphere, with the volume equated to the volume of the corresponding ellipsoid, is also determined. Corresponding energy shifts attributed to the core level energy peak of Bi are depicted in Figure 4.28 and in Table 4.13. The core level energies in the Figure 4.28 were plotted against the square root of the mean volume of the clusters $\langle V_{cl} \rangle^{-1/3}$, as this more accurately represents the size of the clusters than the height measured by STM.

Table 4.13.: Results of the estimation of the energy shifts of the spherical model with the volume equal to corresponding ellipsoid $\Delta E_{cl}^{sph,eq}$ and the spherical model in vicinity of surface ΔE_{cl}^{surf} of the core level. Rows marked in gray indicate STM measurements with a higher gap voltage of 6.0 V.

sample	$\langle V_{cl} \rangle^{-1/3}$ [nm ⁻¹]	ΔE_{cl}^{surf} [eV]	$\Delta E_{cl}^{sph,eq}$ [eV]	sample	$\langle V_{cl} \rangle^{-1/3}$ [nm ⁻¹]	ΔE_{cl}^{surf} [eV]	$\Delta E_{cl}^{sph,eq}$ [eV]
				0.1 ML	0.5(2)	0.5(1)	0.739(8)
				0.2 ML	0.6(2)	0.4(1)	0.696(7)
				0.3 ML	0.6(2)	0.5(1)	0.727(8)
0.38 ML	0.5(2)	0.4(1)	0.63(1)	0.5 ML	0.6(2)	0.5(1)	0.745(8)
300 K	0.4(1)	0.3(1)	0.460(1)	300 K	0.5(2)	0.4(1)	0.655(7)
475 K	0.21(6)	0.13(8)	0.257(1)	475 K	0.27(8)	0.18(7)	0.327(2)

As depicted in Figure 4.28, the shape correction due to cluster deformation results in an almost imperceptible difference between the energy shifts of ellipsoidal and spherical clusters of equivalent volume. Consequently, within the assumptions made earlier and within the range of cluster deformation ($\tau < 3$), the approximation of cluster volume is more important than their shapes. It can therefore be concluded that the assessment of the amount of material deposited and the distribution of clusters is more important than the precise determination of individual cluster heights.

However, the most significant impact arises from the proximity of the conducting surface. By employing a relatively simple model of the metal sphere within the electrostatic regime, we were able to comprehend the energy shift, which closely aligns with the measurements in the first experiment (refer to the Figure 4.28(a)).

The disparity observed in the second experiment (see Figure 4.28(b)) likely stems from the nature of the preparation process: the initial four steps involved a gradual material deposition without annealing. This could account for the inconsistency between the deposited material amount and the measured material within the clusters. It's conceivable that not all Bi atoms have aggregate into clusters, and some may remain loosely bound to the surface.

We also employed a classic approach that appears effective for relatively large clusters. As we approach cluster sizes where the electron spill-out (δ) and the quantum correction factor (α), as mentioned in Equation 4.9, become more significant, it may necessitate additional adjustments to the model.

Additionally, it's worth noting that the dielectric constant of the oxide layers likely differs from that of vacuum, as basically assumed in Equation 4.18. However, characterizing the dispersion of the dielectric function of the oxide is complex, as it may significantly diverge from that of the bulk material.

The contrast in aggregation processes between the sequential increase of deposition material (illustrated in Figure 4.23 from 0.06 ML to 0.5 ML) and the tempering procedure (depicted in the same Figure denoted by 0.5 ML at 300 K and 475 K and in Figure 4.22) is quite striking.

The height of the clusters remained relatively constant as the amount of material increased, while the distance between the clusters decreased. This suggests the formation of new clusters rather than the growth of existing ones. However, there seems to be a threshold in cluster distance below which no new clusters form. This minimum distance is significantly larger (Figure 4.23(d)) than the highest cluster (Figure 4.23(c)), especially at low coverage, ruling out the possibility of clusters simply rearranging side by side. It is more plausible that clusters formed at very short distances eventually merge into one.

Thus, it's reasonable to assume the existence of predefined nucleation positions on the surface, periodically distributed with a minimum distance between them. Additionally, these nucleation positions have a saturation limit. As the material increases, the size of clusters remains almost constant, indicating a preference for Bi atoms to form new clusters at unoccupied nucleation sites rather than contributing to the growth of already saturated clusters.

The saturation threshold can be surpassed by introducing additional energy into the system through tempering at higher temperatures. This increased energy prompts cluster aggregation, resulting in both an increase in the height of the clusters and the distance between them (refer to Figure 4.23(c) and (d)).

At the onset of the ongoing discussion, it was assumed that the proximity of neighboring Bi clusters would have negligible influence on the core level shift in UPS measurements. However, as the discussion progressed, it became evident that the primary effect arises from the proximity of the conducting surface of the Ni₃Al(111) beneath the thin oxide bilayer. The insignificance of the contribution from neighboring clusters to the core level shift in UPS spectra became apparent upon consideration of Equation 4.2.

Given that the UPS signal is additive, the contribution of the majority of clusters is reflected in the spectrum. In Figure 4.23(d), the parameter σ_{90} signifies the minimum distance between clusters for 90 % of the entire sample. This implies that almost all clusters maintain a minimum distance of σ_{90} . The smallest σ_{90} in Figure 4.23(d) is around 3 nm, and the largest is 9.2 nm, indicating that the change in the contribution from neighboring clusters to the charging energy diminishes by a factor of $3^4 = 81$ to $9.2^4 > 7000$ (see Equation 4.2), making the contribution of the neighboring clusters practically negligible.

5. Summary and outlook

In this study, C_{60} molecules and Bi clusters were investigated on the surfaces of two noble metals (Au(111) and Ag(111)) and on the surface of $Al_2O_3||Ni_3Al$, characterized by very low conductivity, using UPS and STM measurements.

On the $Al_2O_3||Ni_3Al$ surface, both C_{60} and Bi clusters exhibited a noticeable shift of the photoemission signal due to the influence of the charging energy: in the case of C_{60} , this shift was attributed to the energy shift of the HOMO, while for Bi clusters, it was visible for the shift of the core level. Conversely, minimal shifts were observed on metal surfaces.

For C_{60} , the shift stemmed from the reduction in charging energy induced by next-neighbor screening, whereas for Bi clusters, it was attributed to the increase in cluster size, with the influence of the $Ni_3Al(111)$ surface playing a significant role in the change of core level shift. Both effects could be explained within the electrostatic approximation, which overlooks quantum mechanical effects like local electron density distribution or electron spill-out, yet still yields excellent agreement with experimental results.

Furthermore, STM investigations revealed evidence of Bi cluster adsorption on the periodic superstructure of the $Al_2O_3||Ni_3Al$ surface, and potentially even adsorption of C_{60} molecules on the periodic structure of the $Al_2O_3||Ni_3Al$ network.

To further validate the model for C_{60} , STS measurements could prove invaluable. However, interpreting STS spectra might pose challenges due to its extremely local nature. As mentioned in the work of Xinghua Lu et al. [116], C_{60} spectra exhibit significant variation, with HOMO peaks appearing on certain parts of the molecule while absent on others.

For studies involving Bi, measurements with small clusters are crucial, ideally with clusters exhibiting a narrow size distribution, achievable through mass-selected clusters. This approach helps minimize model uncertainty. However, it comes with drawbacks such as reduced intensity in the UPS signal, leading to longer measurement times and increased contamination risks.

Additionally, the study of Pb clusters on the surface of $Al_2O_3||Ni_3Al$ could provide a deeper understanding of the process. Specifically because there is evidence that the Pb clusters undergo a metal-to-nonmetal transition (MTNT), as studied in the work of Senz et al. [15] on free metal clusters. The electrostatic effects used to model Bi clusters should also be applicable to Pb clusters. However, the size-dependent change in electronic structure, such as the MTNT (see Section 2.1), when progressing from larger to smaller clusters, might differ due to the different crystal lattice structures (rhombohedral for Bi bulk versus face centered cubic (fcc) for Pb) and band structure differences.

A potential enhancement lies in utilizing synchrotron radiation sources. Synchrotron radiation offers

a wide range of tunable incident light frequencies, facilitating deeper core-level analysis of Bi and overall improving the analysis process.

In studies involving both C_{60} and Bi clusters, the influence of oxide layer thickness may be significant. A systematic investigation into the dependence of charging energy shift on oxide layer thickness could be worthwhile.

A. Appendix

A.1. Energy position of HOMO in UPS

In literature, the energy position of the HOMO level of C₆₀ or inorganic semiconductors is determined either by taking the peak or peak onset positions in PES spectra. Krause and his colleagues have discussed this in detail in their work [138]. They suggest that peak broadening arises due to dynamic charge delocalization during the photoionization process. When the delocalization of the photoemission-generated hole is at its maximum, the C₆₀ molecule is completely screened and this state has the lowest binding energy. However, this happens statistically and so there are states where the molecule is only partially screened, resulting in a broader peak. Hence, the peak onset position is considered more appropriate for determining the HOMO level rather than the peak position.

In present work, we investigated systems with sub-monolayer coverage where C₆₀ molecules occur in small islands with a size distribution. This distribution may contribute to the peak broadening. Additionally, the substrate plays a larger role in our experiments than in Krause et al.'s, which also affects the peak broadening. Nevertheless, the maximally screened state should be less influenced by size distribution broadening and substrate contribution. Therefore, we evaluated the energy position of the HOMO level of C₆₀ as the peak onset. The following section describes the evaluation routine.

A.1.1. Smoothing

The Whittaker-Eilers smoother was utilized to smooth the data, employing a penalized least squares method. In this method (see equation A.1), S represents the lack of fit to the data, while R indicates the roughness. The data is represented by y , and the smooth series of the data is represented by z .

$$Q = S + \lambda R \quad (\text{A.1})$$

$$S = \sum_i w_i (y_i - z_i)^2 \quad (\text{A.2})$$

$$R = \sum_i (z_i - z_{i-1})^2 \quad (\text{A.3})$$

Where w_i denotes weights, so that $w_i = 0$ means the observation is missing and $w_i = 1$ otherwise [139]. The objective of the penalized least squares method is to minimize Q by selecting an appropriate value of λ [140]. One practical advantage of the Whittaker-Eilers smoother is that it allows for flexibility in selecting λ . One can either determine it manually or find the optimal value through an optimization process. To implement the smoother, we utilized the Python project `vam.whittaker` [141], which employs

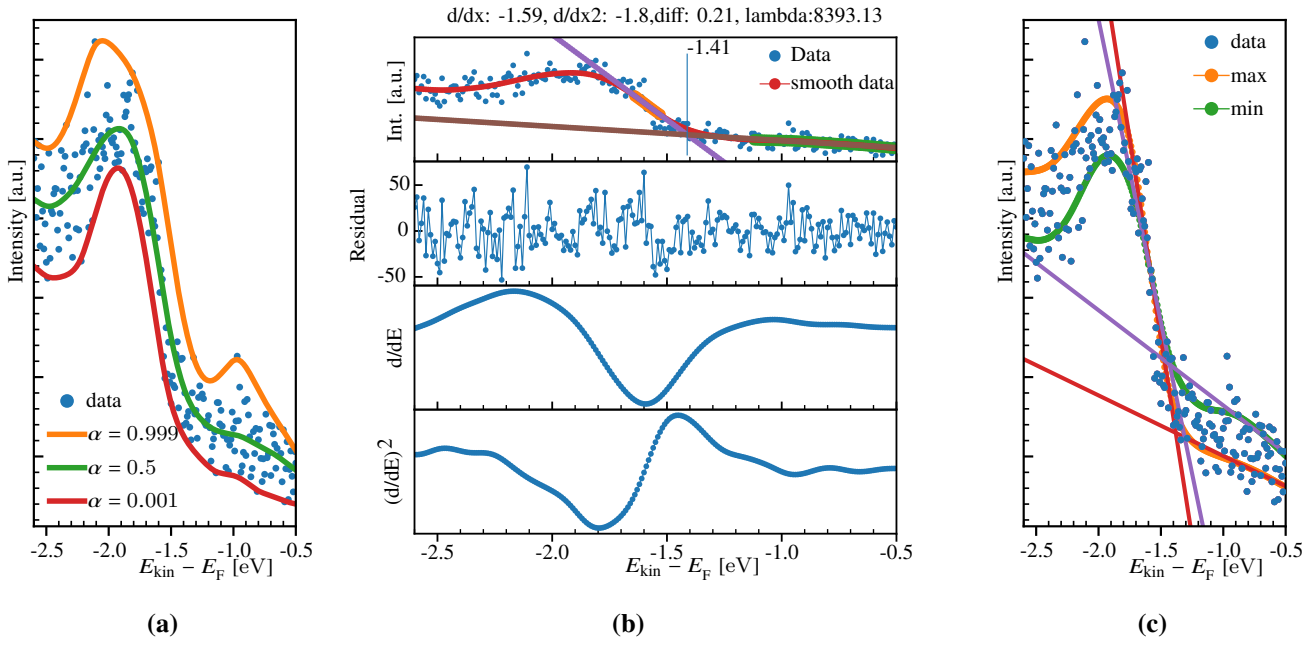


Figure A.1.: Peak onset method. (a) Expectile smoothing. (b) Top panel represents a data with smooth curve and area around the inflection point. Strait lines represents fits and the background and inflection point area. Second panel from top shows the residuals of the smooth curve and data. Third panel from top is the first derivative of smoothed data and in the last panel the second derivative. (c) Smoothing error estimation. Straight lines represent fits for inflection point and background areas on to maximal and minimal “twisted” data subsets. Explanation see text.

V-Curve optimization to search for the optimal lambda value [139].

A.1.2. Peak onset position

To determine the energy of the peak onset position E_{onset} , the inflection point E_{infl} on the energetically lower flank of the peak is identified by calculating the first derivative and determining the minimum. Due to the noise present in the spectra, the computer-assisted evaluation of inflection points can be difficult and inconsistent. To address this, we smoothed the spectra with the Whittaker-Eilers smoother [140]¹ before the evaluation. After the inflection point is found, a straight line is fitted to the area around it. Another linear fit is performed in the background area. The intersection of both straight lines represents the peak onset position.

The choice of the area for the linear fits around the inflection point and for the background should be made very carefully and depends on the experience and common sense of the user.

If the quality of the data or the choice of background leads to very few points for the fit, the error estimates from the fits are not very reliable. To determine the error, we use the entire data set and take advantage of the so-called expectile smoothing feature of the modified Whittaker-Eilers smoother.

In principle, we can rewrite the function given in equation A.2 by introducing a weighting factor α so

¹A brief discussion on why the Whittaker-Eilers smoother is superior to the commonly used Savitzky-Golay filter can be found in [142]

that the negative and positive values of $y - z$ are not weighted equally.

$$S = \sum_i v_i w_i (y_i - z_i)^2 \quad (\text{A.4})$$

with $v_i = \alpha$ when $y_i - z_i > 0$ and $v_i = 1 - \alpha$ when $y_i - z_i < 0$ ² [139]. By choosing a α we now have a direct influence on the smoothing behavior. Figure A.1(a) shows an example of a data set with a wide scatter of measured points. Here we choose the extreme example of $\lambda = 0.999$ and $\lambda = 0.001$. If $\alpha = 0.5$ the perfect smoother is calculated. The smoothed curves represent the envelopes of the data set. By using these envelopes to estimate the error, we would not be taking into account the maximum/minimum possible slope in the scattered data set. To solve this problem, the original data set without smoothing was divided into 2 data sets at the inflection point. The left-hand side was then smoothed with an appropriately large α and the right-hand side with an appropriately small α (i.e. in Figure A.1(c) $\alpha = 0.9$ for the left-hand side and $\alpha = 0.1$ for the right-hand side for the orange curve). The two smoothed curves were then merged and smoothed again to remove the discontinuity in the data at the inflection point. This process was repeated by swapping the α 's of two subsets of data ($\alpha = 0.1$ for the left side and $\alpha = 0.9$ for the right side). Finally, two curves were obtained showing the maximum possible deviation of the curves from the inflection point (see figure A.1(c)). So basically we rotated the smooth curve clockwise and anticlockwise around the inflection point within the scatter path of the data. The values of the two intersection points obtained in this way are then used in the error calculation. Depending on the shape of the curve, these two inflection points may end up on either side of the inflection point of the smoothed data with $\alpha = 0.5$. In this case we take the mean difference as the error, so sometimes we end up with asymmetric errors.

The implementation of this algorithm in Python can be found here [144].

A.2. UPS experimental resolution

The energy resolution of a PES experiment is influenced by various factors, including the energy resolution of the energy analyzer, thermal broadening, energy broadening of the light source and the monochromator, as well as the size of the capillary that focuses the light from the UV source onto the sample and the condition of the sample itself. To determine the resolution of the experiment, a Fermi function $f(E)$ convoluted with a Gaussian function $g(E)$ is used. This function is commonly known as the energy resolution function [146]. An additional constant background $bg(E)$ is also included, which is caused by inelastic-scattering of electrons and is approximately linear in the region of the Fermi edge. The fitting of the convoluted function and the background, as shown in equation A.5, allows us to obtain a fitting parameter, σ , which corresponds to the total experimental resolution $\Delta E_{\text{tot}} = 2\sigma$.

$$s(E) = bg(E) + \int_{-\infty}^{\infty} f(\varepsilon)g(E - \varepsilon)d\varepsilon \quad (\text{A.5})$$

²This is only a rough outline of the problem, in reality it is a bit more complex than presented here, interested readers are referred to the works of Eilers, Pesendorfer and Bonifacio [139] and of Atzberger and Eilers [143].

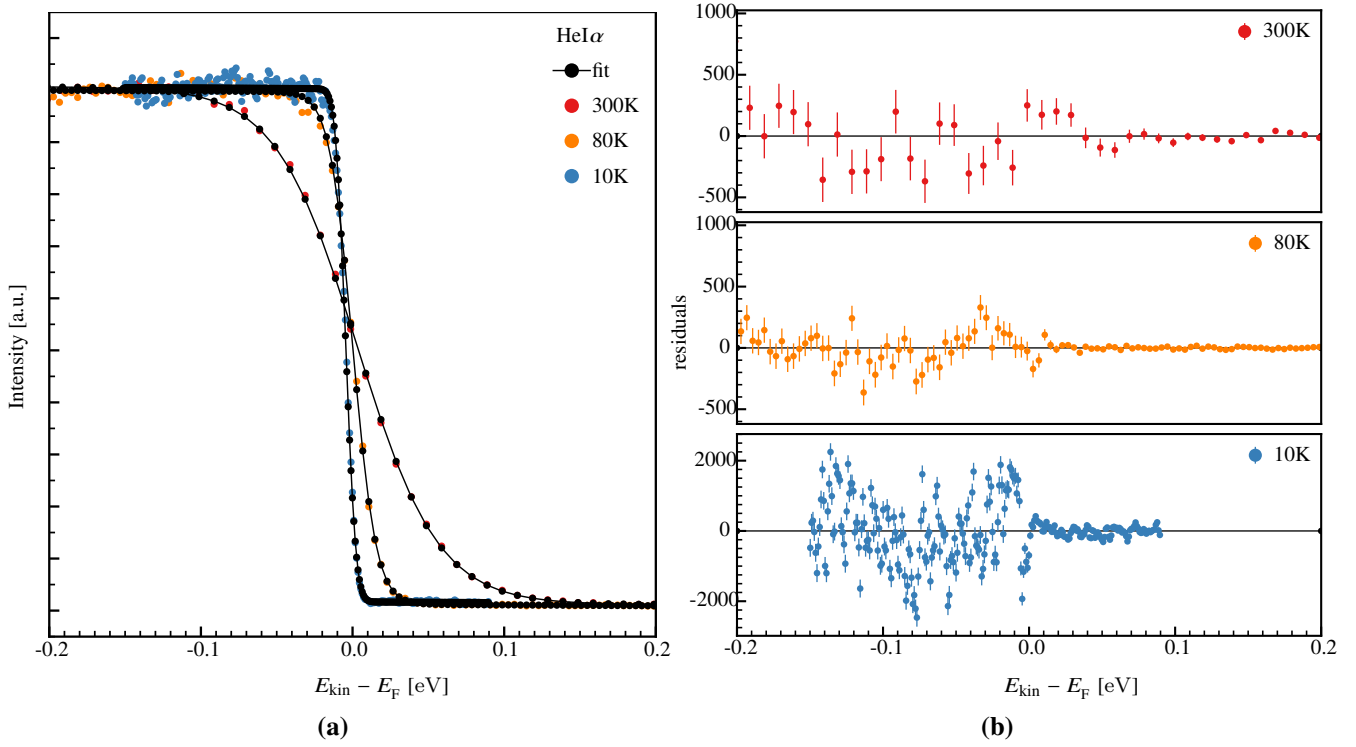


Figure A.2.: (a) UPS data of the Fermi edge at different temperatures (color dots) and corresponding fit (black line). Excitation energy is 21.22 eV (HeI α line). For the definition of the fit model see text. (b) Residual values for the fits from (a) produced by LMFIT more detailed description of estimation of residual can be found here [145]

$$bg(E) = a \cdot E + b \quad (\text{A.6})$$

$$f(E) = \frac{1}{A \exp\left(\frac{E-E_0}{k_B T}\right) + 1} \quad (\text{A.7})$$

$$g(E) = \frac{1}{\sigma\sqrt{2\pi}} \exp\left(-0.5 \frac{(E-\mu)^2}{\sigma^2}\right) \quad (\text{A.8})$$

The fitting of the convoluted function and background was performed using the python package "LMFIT" [145]. The model used for the convolution of the Fermi-Dirac function and Gaussian function was adapted from the python project of Hochhaus and Nakajima [147].

Experimental resolution in dependence of the temperature can be found in table A.1. Figures A.2 and A.3 show the data of the Fermi edge and the corresponding fits. The Fermi Edge for HeI α exiting energy is at $E_{kin} = (16.89728 \pm 0.00005)$ eV and for HeII α at $E_{kin} = (36.4768 \pm 0.0002)$ eV

Table A.1.: The experimental resolution of UPS experiments was determined by fitting the Fermi edge at the corresponding temperature (see Figure A.2). All measurements were taken with a pass energy of 2 eV

T [K]	300	80	10
HeI α ΔE_{tot} [meV]	(23 ± 2)	(10.8 ± 0.4)	(10.11 ± 0.08)
HeII α ΔE_{tot} [meV]	(18 ± 5)	(12 ± 2)	–

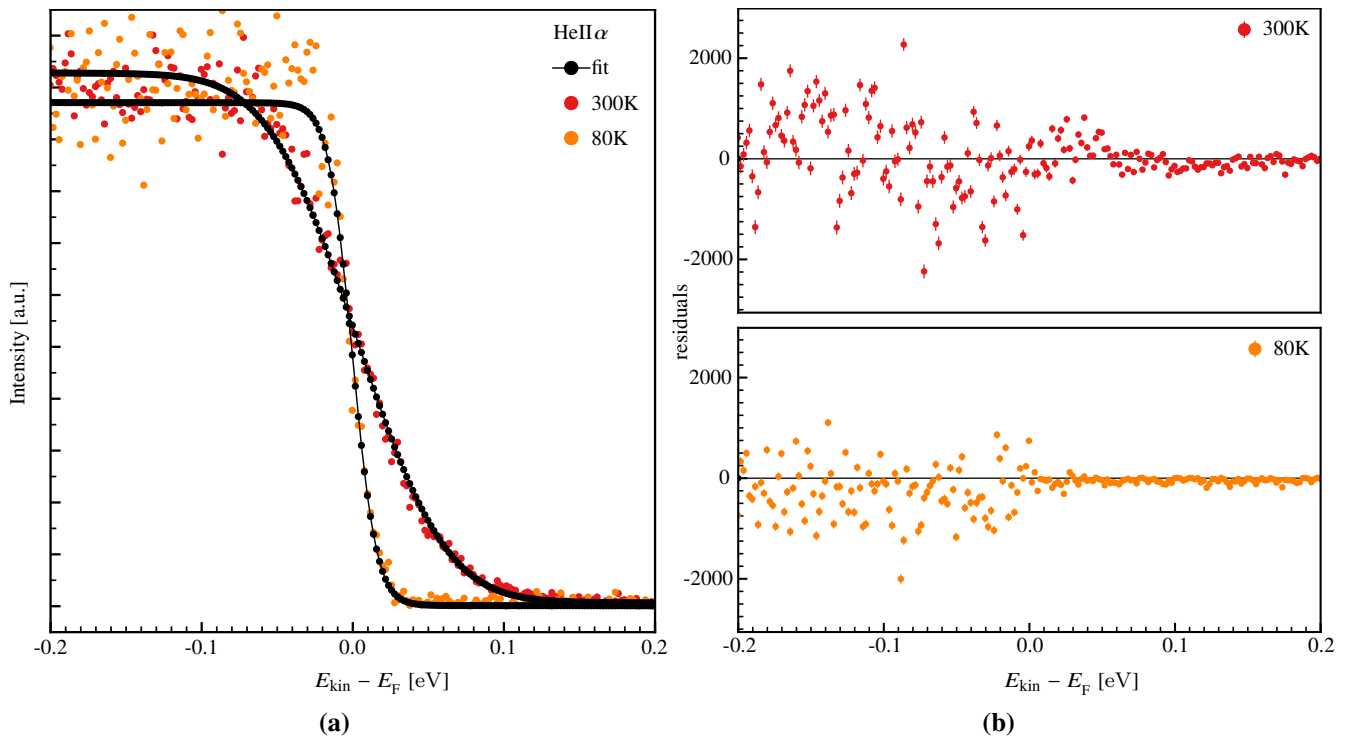


Figure A.3.: Same as in figure A.2 but with the excitation energy of 40.8 eV (HeII α line).

A.3. Line shape of core level in UPS

For the study of core levels of Bi in this work, a DS profile convolved with a Gaussian distribution was used (see Equation A.9). This specific profile is well known and widely accepted³ for handling asymmetric peaks in XPS spectroscopy. The theoretical justification for fitting with DS is provided to some extent in the work of Wertheim and Citrin [148].

$$I(E) = \int_{-\infty}^{\infty} DS(\varepsilon)g(E - \varepsilon)d\varepsilon \quad (\text{A.9})$$

With DS as Doniach-Sunjc line shape (see equation A.10) and $g(E)$ as Gaussian function as given in equation A.8

$$DS(E) = \frac{A}{\sigma^{1-\alpha}} \frac{\cos[\pi\alpha/2 + (1-\alpha)\arctan((E-\mu)/\sigma)]}{[1 + (E-\mu)/\sigma]^{(1-\alpha)/2}} \quad (\text{A.10})$$

α can be understood as asymmetry parameter. 2σ is equal to Lorentzian's FWHM for $\alpha = 0$ [128]

A.4. Cluster height determination in STM images

As already mentioned in the Figure 2.11, the broadening of clusters on surfaces caused by STM-tip broadening leads to a false representation of the lateral dimensions of small particles/clusters. However, the height information from STM measurements is very precise. By accurately determining the deposited amount of material onto a surface and using the height information, it is possible to calculate the amount of material per particle (see Chapter 4.2).

A typical STM image consists of various surface features such as defects and step edges. For the correct

³The original publication by Doniach and Šunjić [62] has received over 2.5 thousand citations.

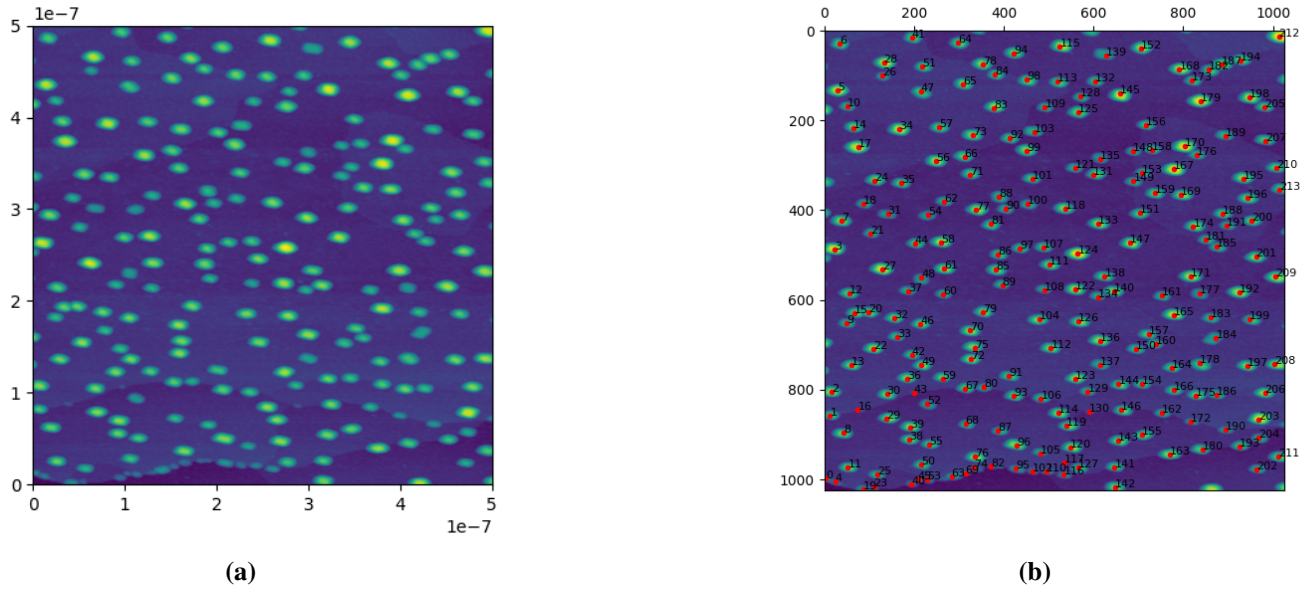


Figure A.4.: Example of cluster height correction. (a) STM data after substrate levelling. (b) Automatically found clusters using the algorithm described in the text. Some of the clusters at the edge are not taken into account because the algorithm includes a functionality to ignore the highest points at the edge of the image if they are exactly at the edge, which means that the cluster was not fully covered.

determination of cluster height, it is crucial to take this into account. Therefore, the surrounding area of each individual cluster should be considered as a baseline for the calculation of the cluster height.

It is possible to manually correct the height of clusters using software designed for processing scanning probe microscope (SPM) data (for example Gwyddion [94]). However, this manual process can be cumbersome, especially as the number of clusters per area increases. Therefore, during the course of the present work, an algorithm “stm-cluster-heighttzer”⁴ was developed to streamline and automate this correction process. In the current section, a concise overview of this algorithm will be presented. For more in-depth information, please refer to the source code [149].

The algorithm can be basally represented as 4 step operation:

1. Find all clusters by scanning every raw and/or every column of the data and finding of local maxima (see Figure A.4).
2. Split the STM image in to regions around the clusters (see Figure A.5(a)).
3. Determine the highest point of cluster and the ground level by excluding all points with highest slope (see Figure A.5(b)).
4. Correcting the cluster height for each individual cluster based on the average of ground level points and there grouping.

The final result of the calculation is a table of all the clusters with the corrected height in three different ways. Averaged: the heights of all ground level points are averaged and subtracted from the initial cluster height. Nearest step: the average height of the nearest step⁵ is subtracted from the height of the cluster’s

⁴The word heighttzer is a combination of height and resizer

⁵The step with the smallest distance between the cluster’s peak and the center of the step coordinates.

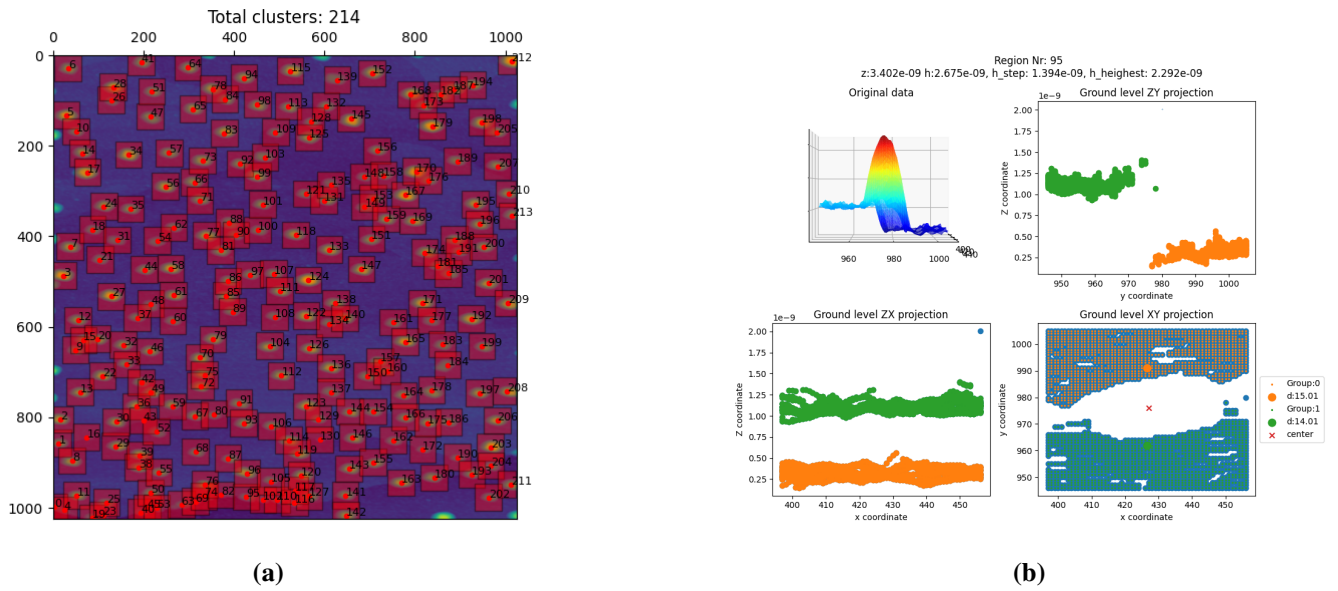


Figure A.5.: Example of cluster height correction. (a) Same STM image as in figure A.4 with the additional marked region around each cluster. It is also possible to select a non symmetric region, in which case the Voronoi diagram algorithm [150] is applied. (b) Determination of the ground level of a region from figure A.5(a). The algorithm eliminates the points with height gradients and clusters the data points by calculating the nearest neighbor distance in three dimensions.

peak. Highest step: The highest averaged height of all separated steps is subtracted from the height of the cluster peak (see Figure A.6).

	x	y	x_m	y_m	initial_Z	corrected_Z_averaged	corrected_Z_closest_step	corrected_Z_highest_step
rectangular 30 pix								
0	998.0	4.0	4.873047e-07	1.953125e-09	2.948160e-09	2.281497e-09	2.070668e-09	1.942243e-09
1	857.0	13.0	4.184570e-07	6.347656e-09	4.783015e-09	3.834228e-09	3.766808e-09	3.500937e-09
2	805.0	16.0	3.930664e-07	7.812500e-09	5.274741e-09	4.192211e-09	4.203353e-09	4.000895e-09
3	487.0	23.0	2.377930e-07	1.123047e-08	6.004031e-09	5.178342e-09	5.208415e-09	5.208415e-09
4	1005.0	25.0	4.907227e-07	1.220703e-08	2.799530e-09	2.067630e-09	1.762365e-09	1.404961e-09
...
209	548.0	1006.0	2.675781e-07	4.912109e-07	5.488743e-09	4.783766e-09	4.875156e-09	4.538335e-09
210	306.0	1008.0	1.494141e-07	4.921875e-07	4.832544e-09	3.927080e-09	4.054252e-09	3.908142e-09
211	948.0	1012.0	4.628906e-07	4.941406e-07	4.775397e-09	4.160457e-09	4.100673e-09	3.909772e-09
212	14.0	1013.0	6.835937e-09	4.946289e-07	6.327953e-09	5.222950e-09	5.378678e-09	5.086095e-09
213	355.0	1015.0	1.733398e-07	4.956055e-07	4.573350e-09	3.689812e-09	3.534042e-09	3.483015e-09

Figure A.6.: Screenshot of the result table generated by the stm-cluster-heightzer algorithm. The first column represents the index, x and y are the pixel coordinates, x_m and y_m are the corresponding coordinates in meters. The initial_Z column shows the peak value of a cluster and the last three columns represent the height correction, which is described in text.

A.5. Error Propagation

A.5.1. Capacitance of a sphere in vicinity of surface.

The error propagation of the formula represented in Equation 4.18 is given here. Only two parameters are considered to have errors, r and d .

$$C_{\text{surf}}(d, r) = 4\pi\epsilon_0 r F [\cosh^{-1}(d/r)] \quad \text{with } F(\xi) = \sinh(\xi) \sum_{n=0}^{\infty} \frac{1}{\sinh[(n+1)\xi]} \quad \text{and } d \pm \Delta d, r \pm \Delta r \quad (\text{A.11})$$

$$\Delta C_{\text{surf}}(d, r) = \sqrt{\left(\frac{\partial C_{\text{surf}}}{\partial r} \Delta r\right)^2 + \left(\frac{\partial C_{\text{surf}}}{\partial d} \Delta d\right)^2} \quad (\text{A.12})$$

$$\frac{\partial C_{\text{surf}}}{\partial r} = \kappa \sinh(\xi) \Gamma + \kappa r \frac{\partial \sinh(\xi)}{\partial r} \Gamma + \kappa r \sinh(\xi) \frac{\partial \Gamma}{\partial r} \quad (\text{A.13})$$

$$\frac{\partial C_{\text{surf}}}{\partial d} = \kappa r \frac{\partial \sinh(\xi)}{\partial d} \Gamma + \kappa r \sinh(\xi) \frac{\partial \Gamma}{\partial d} \quad (\text{A.14})$$

With $\Gamma = \sum_{n=0}^{\infty} \frac{1}{\sinh[(n+1)\xi]}$, $\kappa = 4\pi\epsilon_0$ and $\xi = \cosh^{-1}(d/r)$. Just for clarity every component will be written separately:

$$\frac{\partial \sinh(\xi)}{\partial r} = -\frac{d^2}{r^2(d+r)\sqrt{(d-r)/(d+r)}} \quad (\text{A.15})$$

$$\frac{\partial \Gamma}{\partial r} = \frac{d}{r^2\sqrt{(d/r)-1}\sqrt{(d/r)+1}} \sum_{n=0}^{\infty} (n+1) \frac{\coth((n+1)\xi)}{\sinh((n+1)\xi)} \quad (\text{A.16})$$

$$\frac{\partial \sinh(\xi)}{\partial d} = \frac{d}{r(d+r)\sqrt{(d-r)/(d+r)}} \quad (\text{A.17})$$

$$\frac{\partial \Gamma}{\partial d} = \frac{1}{r\sqrt{(d/r)-1}\sqrt{(d/r)+1}} \sum_{n=0}^{\infty} (n+1) \frac{\coth((n+1)\xi)}{\sinh((n+1)\xi)} \quad (\text{A.18})$$

B. Supplementary material

B.1. C₆₀ on Au(111)

B.1.1. Au(111) clean surface

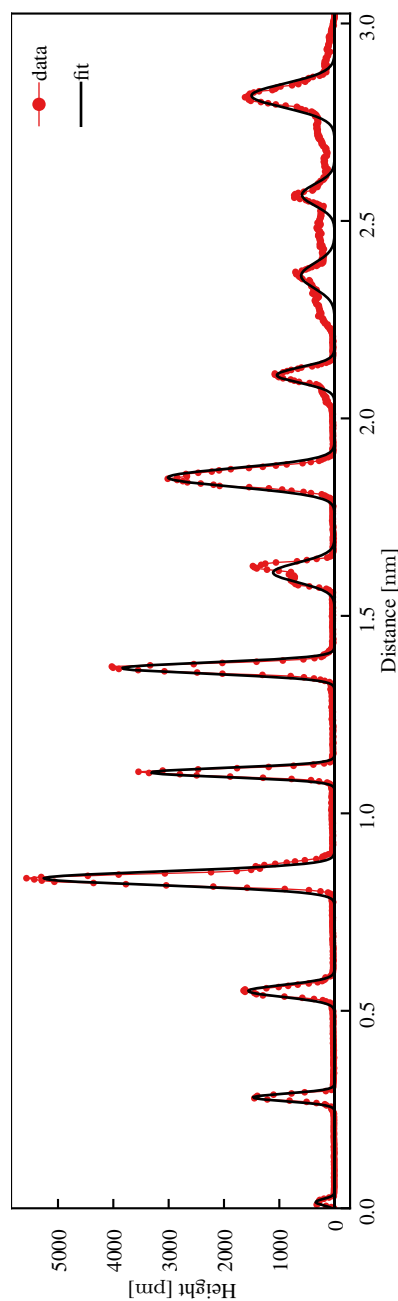


Figure B.1.: Gaussian fits of the binned data of Au(111) clean surface for estimation of atomic step height (see Figure 4.6 upper left corner). Fits were performed using *Fityk* [151].

Table B.1.: Parameters of the Gaussian fits to the peaks in blue profile from Figure 4.6. Fitted curve is also represented in Figure B.1.

peak#.parameter	value [m]	error [m]
1.height	345	56.2
1.center	1.56e-11	9.21e-13
1.hwhm	7.89e-12	7.52e-13
2.height	1480	108
2.center	2.81e-10	4.86e-13
2.hwhm	9.7e-12	4.27e-13
3.height	1560	91
3.center	5.5e-10	5.88e-13
3.hwhm	1.5e-11	5.42e-13
4.height	5260	155
4.center	8.35e-10	3.57e-13
4.hwhm	1.73e-11	3.13e-13
5.height	3330	148
5.center	1.1e-09	3.51e-13
5.hwhm	1.16e-11	3.09e-13
6.height	3850	147
6.center	1.37e-09	3.61e-13
6.hwhm	1.41e-11	3.32e-13
7.height	1110	56.8
7.center	1.61e-09	9.1e-13
7.hwhm	2.48e-11	7.09e-13
8.height	3010	96.8
8.center	1.85e-09	5.29e-13
8.hwhm	2.38e-11	4.43e-13
9.height	1050	66.1
9.center	2.11e-09	9.03e-13
9.hwhm	1.96e-11	8.74e-13
10.height	607	45.7
10.center	2.36e-09	2.41e-12
10.hwhm	3.17e-11	3.23e-12
11.height	591	47.2
11.center	2.57e-09	1.63e-12
11.hwhm	2.74e-11	2.25e-12
12.height	1500	68.3
12.center	2.82e-09	1.07e-12
12.hwhm	3.05e-11	1.31e-12

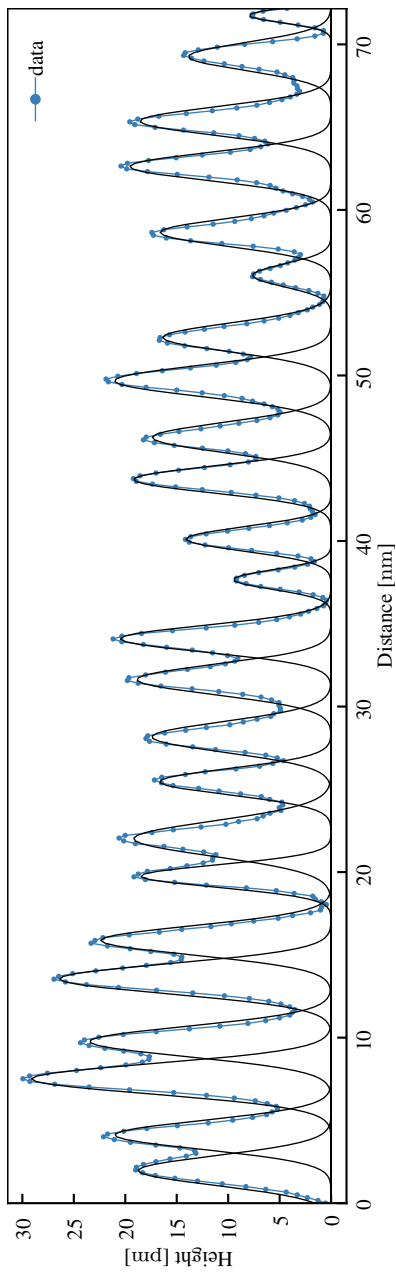


Figure B.2.: Gaussian fits of the superstructure of Au(111) surface in height profiles taken from Figure 4.6. Fits were performed using *Fityk*[151].

Table B.2.: Parameters of the Gaussian fits to the peaks in blue profile from Figure 4.6. Fitted curve is also represented in Figure B.2.

peak#.parameter	value [m]	error [m]	peak#.parameter	value [m]	error [m]
4.height	1.88e-11	3.74e-13	16.height	9.49e-12	4.48e-13
4.center	1.97e-09	3.11e-11	16.center	3.77e-08	2.75e-11
4.hwhm	8.89e-10	3.4e-11	16.hwhm	5.89e-10	3.32e-11
5.height	2.1e-11	3.84e-13	17.height	1.41e-11	4.04e-13
5.center	4.12e-09	2.68e-11	17.center	4.01e-08	2.06e-11
5.hwhm	8.59e-10	3.05e-11	17.hwhm	7.29e-10	2.5e-11
6.height	2.91e-11	3.71e-13	18.height	1.92e-11	3.86e-13
6.center	7.51e-09	1.9e-11	18.center	4.37e-08	1.85e-11
6.hwhm	9.04e-10	2.22e-11	18.hwhm	8.01e-10	2.29e-11
7.height	2.35e-11	3.7e-13	19.height	1.74e-11	3.71e-13
7.center	9.77e-09	2.39e-11	19.center	4.63e-08	2.15e-11
7.hwhm	9.04e-10	2.67e-11	19.hwhm	9.04e-10	2.89e-11
8.height	2.64e-11	3.67e-13	20.height	2.1e-11	3.64e-13
8.center	1.36e-08	1.84e-11	20.center	4.97e-08	1.87e-11
8.hwhm	9e-10	2.19e-11	20.hwhm	9.4e-10	2.5e-11
9.height	2.24e-11	3.7e-13	21.height	1.64e-11	3.72e-13
9.center	1.59e-08	2.15e-11	21.center	5.23e-08	2.33e-11
9.hwhm	8.79e-10	2.49e-11	21.hwhm	8.63e-10	2.88e-11
10.height	1.85e-11	4.36e-13	22.height	7.63e-12	4.18e-13
10.center	1.98e-08	2.04e-11	22.center	5.6e-08	3.78e-11
10.hwhm	6.71e-10	2.3e-11	22.hwhm	6.8e-10	4.62e-11
11.height	1.92e-11	3.5e-13	23.height	1.66e-11	3.78e-13
11.center	2.2e-08	2.46e-11	23.center	5.86e-08	1.92e-11
11.hwhm	1.05e-09	3.32e-11	23.hwhm	8.41e-10	2.39e-11
12.height	1.67e-11	3.92e-13	24.height	1.95e-11	3.75e-13
12.center	2.55e-08	1.97e-11	24.center	6.26e-08	1.72e-11
12.hwhm	7.83e-10	2.54e-11	24.hwhm	8.56e-10	2.16e-11
13.height	1.74e-11	3.67e-13	25.height	1.86e-11	3.75e-13
13.center	2.82e-08	2.01e-11	25.center	6.54e-08	1.81e-11
13.hwhm	9.17e-10	2.66e-11	25.hwhm	8.59e-10	2.28e-11
14.height	1.89e-11	3.7e-13	26.height	1.39e-11	3.76e-13
14.center	3.16e-08	2.07e-11	26.center	6.93e-08	2.23e-11
14.hwhm	9.06e-10	2.73e-11	26.hwhm	8.39e-10	2.69e-11
15.height	2.05e-11	3.85e-13	27.height	8.01e-12	5.35e-13
15.center	3.41e-08	1.82e-11	27.center	7.17e-08	3.17e-11
15.hwhm	8.04e-10	2.23e-11	27.hwhm	4.42e-10	4.26e-11

B.1.2. 0.02 ML C₆₀ || Au(111)

Table B.3.: Parameters of the Gaussian fits to the peaks in blue profile from Figure 4.7(b). Fitted curve is also represented in Figure B.3.

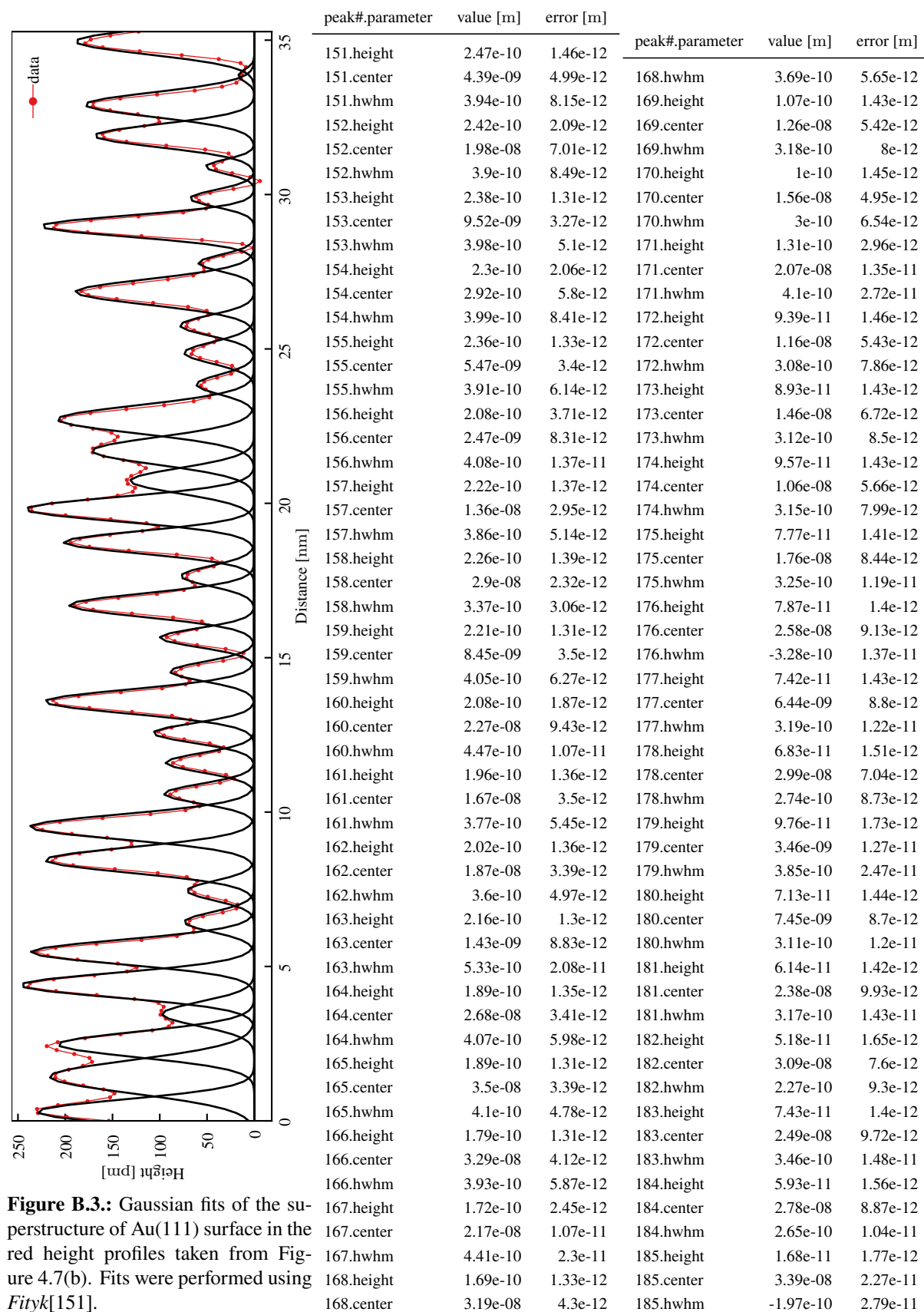


Figure B.3.: Gaussian fits of the superstructure of Au(111) surface in the red height profiles taken from Figure 4.7(b). Fits were performed using *Fityk*[151].

Table B.4.: Parameters of the Gaussian fits to the peaks in the red profile from Figure 4.7(b). Fitted curve is also represented in Figure B.4.

peak#.parameter	value [m]	error [m]	peak#.parameter	value [m]	error [m]
66.height	2.11e-10	1.76e-12	132.hwhm	3.57e-10	3.01e-11
66.center	1.77e-08	5.48e-12	133.height	8.27e-11	2.54e-12
66.hwhm	5.97e-10	8e-12	133.center	3.27e-08	9.83e-12
67.height	2.02e-10	1.78e-12	133.hwhm	2.7e-10	1.24e-11
67.center	2.91e-09	7e-12	134.height	1.03e-10	1.9e-11
67.hwhm	6.52e-10	1.25e-11	134.center	1.48e-08	2.71e-11
68.height	1.93e-10	1.87e-12	134.hwhm	3.61e-10	3.62e-11
68.center	1.58e-08	1.25e-11	135.height	8.24e-11	2.55e-12
68.hwhm	5.64e-10	1.54e-11	135.center	2.66e-08	2.04e-11
69.height	1.98e-10	2.22e-12	135.hwhm	3.4e-10	2.93e-11
69.center	2.96e-08	4.64e-12	136.height	7.66e-11	2.37e-12
69.hwhm	3.83e-10	6.82e-12	136.center	3.47e-08	1.21e-11
70.height	1.77e-10	1.78e-12	136.hwhm	3.2e-10	1.67e-11
70.center	1.97e-08	1.05e-11	137.height	6.77e-11	2.33e-12
70.hwhm	6.34e-10	1.5e-11	137.center	3.08e-08	1.52e-11
72.height	1.9e-10	2.07e-12	137.hwhm	3.29e-10	2.11e-11
72.center	1.38e-08	2.6e-11	138.height	9.37e-11	2.24e-12
72.hwhm	6.46e-10	7.97e-11	138.center	2.37e-08	1.59e-11
73.height	2.21e-10	2.48e-12	138.hwhm	3.8e-10	2.53e-11
73.center	3.67e-08	1.05e-11	139.height	5.6e-11	2.4e-12
73.hwhm	4.14e-10	2.58e-11	139.center	2.85e-08	2.63e-11
74.height	1.62e-10	1.8e-11	139.hwhm	3.37e-10	3.35e-11
74.center	5.87e-09	4.47e-11	140.height	2.06e-10	6.68e-10
74.hwhm	3.91e-10	5.06e-11	140.center	7.9e-09	1.53e-09
76.height	6.87e-11	2.37e-12	140.hwhm	4.33e-10	8.78e-10
76.center	3.17e-08	1.49e-11	141.height	2.05e-10	1.53e-11
76.hwhm	3.39e-10	2.39e-11	141.center	9.85e-09	2.54e-11
82.height	8.17e-11	2.51e-12	141.hwhm	4.29e-10	5.1e-11
82.center	3.37e-08	8.81e-12	142.height	2.09e-10	2.71e-11
82.hwhm	2.79e-10	1.13e-11	142.center	6.78e-09	8.27e-11
118.height	2.27e-11	1.15e-09	142.hwhm	4.71e-10	1.15e-10
118.center	7.53e-09	1.78e-09	143.height	1.06e-10	3.52e-12
118.hwhm	3.24e-10	2.09e-09	143.center	4.96e-09	2.61e-11
125.height	2.31e-10	4e-12	143.hwhm	3.66e-10	2.85e-11
125.center	3.58e-08	1.21e-11	144.height	1.71e-10	1.8e-12
125.hwhm	3.68e-10	1.26e-11	144.center	9.1e-10	1.39e-11
126.height	2.26e-10	4.47e-12	144.hwhm	6.41e-10	2.1e-11
126.center	2.26e-08	1.37e-11	145.height	7.09e-11	1.64e-11
126.hwhm	4.08e-10	1.88e-11	145.center	1.18e-08	4.28e-11
127.height	2.16e-10	4.54e-11	145.hwhm	3.34e-10	4.08e-11
127.center	8.88e-09	1.02e-10	146.height	7.58e-11	2.84e-12
127.hwhm	4.24e-10	1.09e-10	146.center	1.1e-08	5.42e-11
128.height	7.41e-11	4.59e-12	146.hwhm	5.58e-10	1.98e-10
128.center	2.07e-08	1.66e-11	147.height	7.28e-11	2.79e-12
128.hwhm	2.76e-10	2.18e-11	147.center	2.17e-08	4.73e-11
129.height	1.02e-10	2.26e-12	147.hwhm	4.58e-10	6.92e-11
129.center	2.48e-08	1.17e-11	148.height	3.91e-11	3.13e-12
129.hwhm	3.57e-10	1.95e-11	148.center	4.04e-09	2.25e-11
130.height	7.98e-11	2.36e-12	148.hwhm	2.48e-10	3.03e-11
130.center	3.86e-08	1.08e-11	149.height	5.16e-11	4.64e-12
130.hwhm	3.36e-10	1.54e-11	149.center	3.75e-08	4.59e-11
131.height	9.36e-11	2.32e-12	149.hwhm	3.28e-10	4.42e-11
131.center	2.58e-08	1.8e-11	150.height	6.56e-11	1.28e-11
131.hwhm	3.64e-10	2.98e-11	150.center	1.28e-08	2.43e-11
132.height	7.8e-11	2.29e-12	150.hwhm	3.05e-10	3.7e-11
132.center	2.76e-08	1.82e-11			

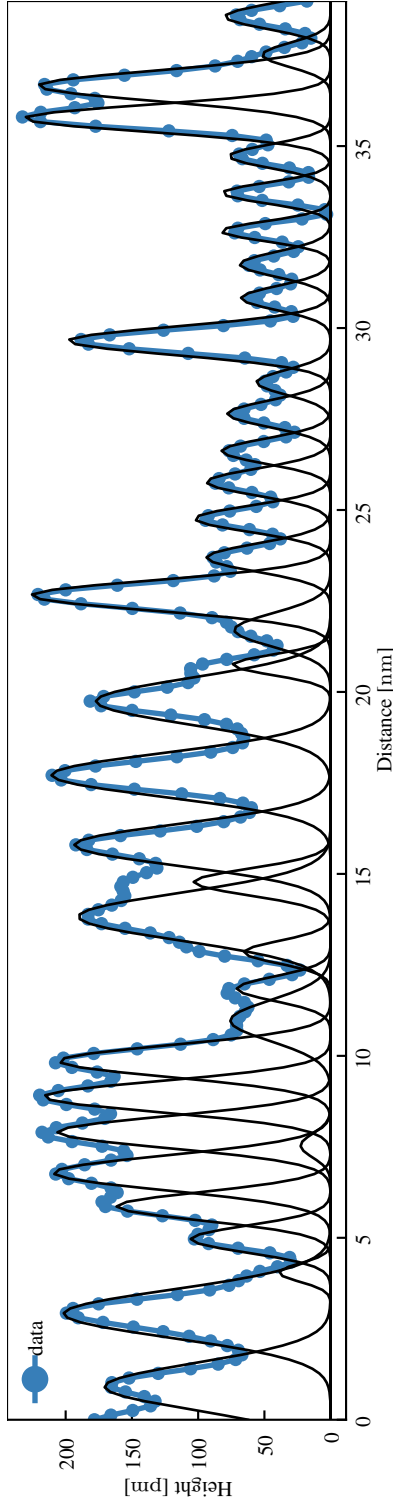
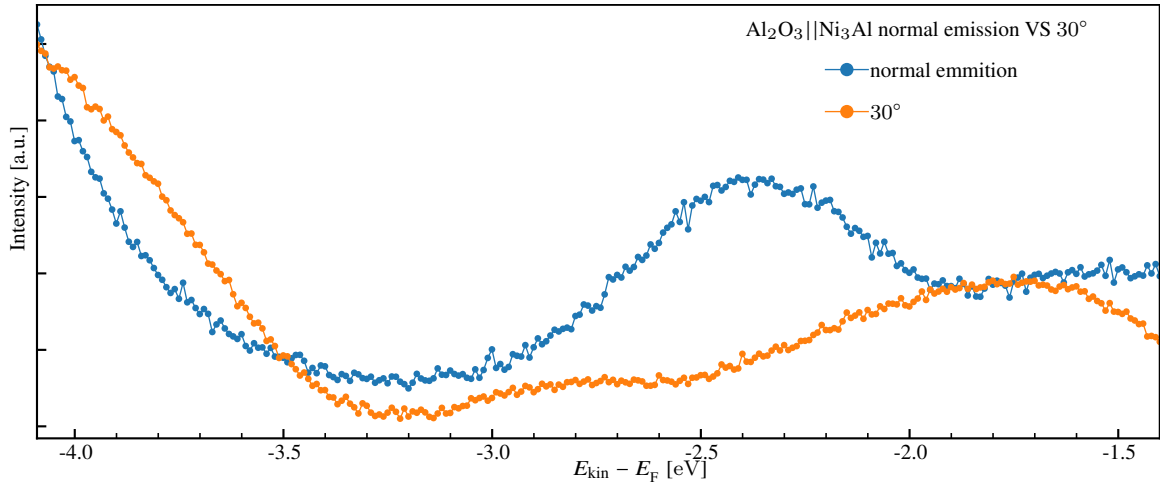


Figure B.4.: Gaussian fits of the superstructure of Au(111) surface in the blue height profiles taken from Figure 4.7(b). Fits were performed using *Fityk*[151].

Table B.5.: Parameters of the Gaussian fits to the peaks in the Figure 4.7(c).

peak#.parameter	value [m]	error [m]
7.height	1.01e-06	8.61e-09
7.center	9.46e-11	1.14e-13
7.hwhm	1.04e-11	8.42e-09
8.height	6.83e-07	6.2e-09
8.center	1.23e-10	1.81e-13
8.hwhm	1.3e-11	1.32e-13

B.2. C_{60} on $Al_2O_3||Ni_3Al$



(a)

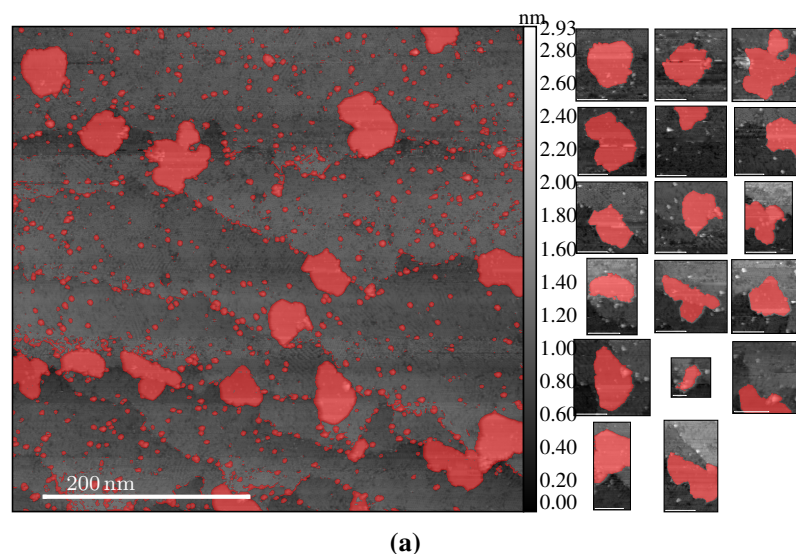
Figure B.5.: UPS Spectrum of bear $Al_2O_3||Ni_3Al$ at different emission angles. In the region between -3.5 and 2.0 eV, which is the region where the HOMO peak of C_{60} appears, a large feature is visible, which probably originates from the $Ni_3Al(111)$ crystal and disappears almost completely below the 30° angle. The image was recorded at RT and with an excitation energy E_{exc} of 21.22 eV (HeI α line).

B.3. $Al_2O_3||Ni_3Al$ preparation procedure

Table B.6.: Preparation routine of $Al_2O_3||Ni_3Al$

#	Action	Duration (min)	Parameters
1	Sputtering	60	5 μ A, 1.5 kV
	Heating	2 \times 7	1150 K, 1000 K
2	Sputtering	45	5 μ A, 1.5 kV
	Heating	2 \times 7	1150 K, 1000 K
3	Sputtering	30	5 μ A, 1.5 kV
	Heating	2 \times 7	1150 K, 1000 K
4	Sputtering	15	5 μ A, 1.5 kV
	Heating	2 \times 7	1150 K, 1000 K
5	Sputtering	10	5 μ A, 1.5 kV
	Heating	2 \times 7	1150 K, 1000 K
6	Sputtering	5	5 μ A, 1.5 kV
	Heating	2 \times 7	1150 K, 1000 K
7	Oxidation	30	1000 K, 40 L (3×10^{-8} mbar)
	Flashing	5	1050 K
8	Oxidation	30	1000 K, 40 L (3×10^{-8} mbar)
	Flashing	5	1050 K
9	Cooling	30	-
	Flashing	10	1050 K

B.4. Separated C₆₀ islands deposited at room temperature



(a)

Figure B.6.: STM images of 0.2 ML of C₆₀ deposited on Al₂O₃||Ni₃Al(111) at room temperature (see also figure 4.10(a)). Left side: flattened image for estimation of whole coverage of C₆₀. Right side: separated large islands. All white bars in the images represent the length scale of 30 nm except for the middle image in the 5th row which length is 10 nm

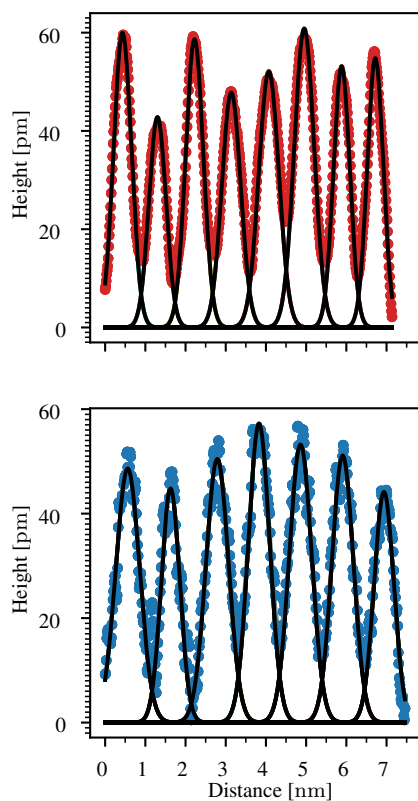


Figure B.7.: Gaussian fits of the C₆₀ molecules in height profiles taken from figure 4.10(c). Fits were performed using *Fityk*[151].

Table B.7.: Parameters of the Gaussian fits to the peaks in red profile from figure 4.10(c).

peak#.parameter	value	err
52.height	6.00E-11	3.74E-13
52.center	4.31E-10	1.63E-12
52.hwhm	2.60E-10	2.12E-12
53.height	4.28E-11	3.80E-13
53.center	1.30E-09	2.25E-12
53.hwhm	2.49E-10	2.90E-12
54.height	5.87E-11	3.74E-13
54.center	2.22E-09	1.67E-12
54.hwhm	2.57E-10	2.16E-12
55.height	4.78E-11	3.64E-13
55.center	3.14E-09	2.20E-12
55.hwhm	2.77E-10	2.99E-12
56.height	5.21E-11	3.57E-13
56.center	4.07E-09	2.25E-12
56.hwhm	2.93E-10	3.23E-12
57.height	6.08E-11	3.56E-13
57.center	4.95E-09	1.90E-12
57.hwhm	2.91E-10	2.60E-12
58.height	5.32E-11	3.87E-13
58.center	5.88E-09	1.77E-12
58.hwhm	2.39E-10	2.29E-12
8.height	5.48E-11	3.90E-13
8.center	6.72E-09	1.67E-12
8.hwhm	2.35E-10	2.12E-12

Table B.8.: Same as in table B.7 but for blue profile.

peak#.parameter	value	error
1.height	4.87E-11	6.77E-13
1.center	5.61E-10	4.84E-12
1.hwhm	3.50E-10	6.40E-12
2.height	4.48E-11	7.55E-13
2.center	1.63E-09	4.64E-12
2.hwhm	2.70E-10	5.79E-12
3.height	5.05E-11	6.92E-13
3.center	2.79E-09	4.71E-12
3.hwhm	3.31E-10	6.12E-12
4.height	5.72E-11	7.17E-13
4.center	3.83E-09	4.22E-12
4.hwhm	3.12E-10	5.87E-12
5.height	5.32E-11	7.06E-13
5.center	4.86E-09	4.59E-12
5.hwhm	3.26E-10	6.45E-12
6.height	5.11E-11	7.15E-13
6.center	5.91E-09	4.58E-12
6.hwhm	3.14E-10	6.22E-12
7.height	4.42E-11	7.38E-13
7.center	6.94E-09	4.86E-12
7.hwhm	2.88E-10	6.19E-12

B.5. C₆₀||HOPG

For the measurement of the UPS of C₆₀ on HOPG, the HOPG substrate was initially prepared by heating it in UHV at a base pressure¹ of 6.1×10^{-10} mbar for 30 min at 600 °C. After the HOPG substrate cooled down to RT, the UPS spectrum was recorded.

Subsequently, 0.25 ML of C₆₀ was evaporated onto the substrate at RT, and another UPS spectrum was recorded. The results of this experiment can be found in Figure B.8. Thereby the peak onset position and the position of the inflection point was determined to $-1.833_{-0.0}^{+0.006}$ and $-1.917_{-0.016}^{+0.003}$ by using the method represented in Appendix A.1.2. As one can see in the zoomed portion of Figure B.8, there is no signal contribution of C₆₀ in the vicinity of the Fermi edge.

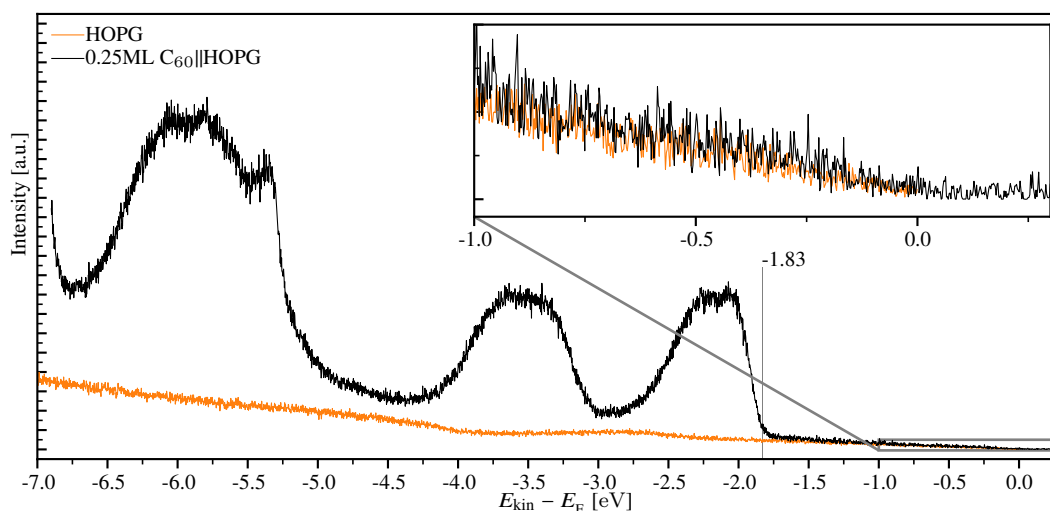


Figure B.8.: UPS spectra of clean HOPG and 0.25ML of C₆₀ on HOPG. $E_{\text{exc}} = 21.22$ eV. Deposited and measured at RT. Image insert in the top right corner shows a zoom into the vicinity of Fermi edge. The vertical line at -1.83 eV represents the PoP described in Appendix A.1.2

¹During preparation, the pressure increased to a maximum of 1.1×10^{-9} mbar.

B.6. Bi on Au(111)

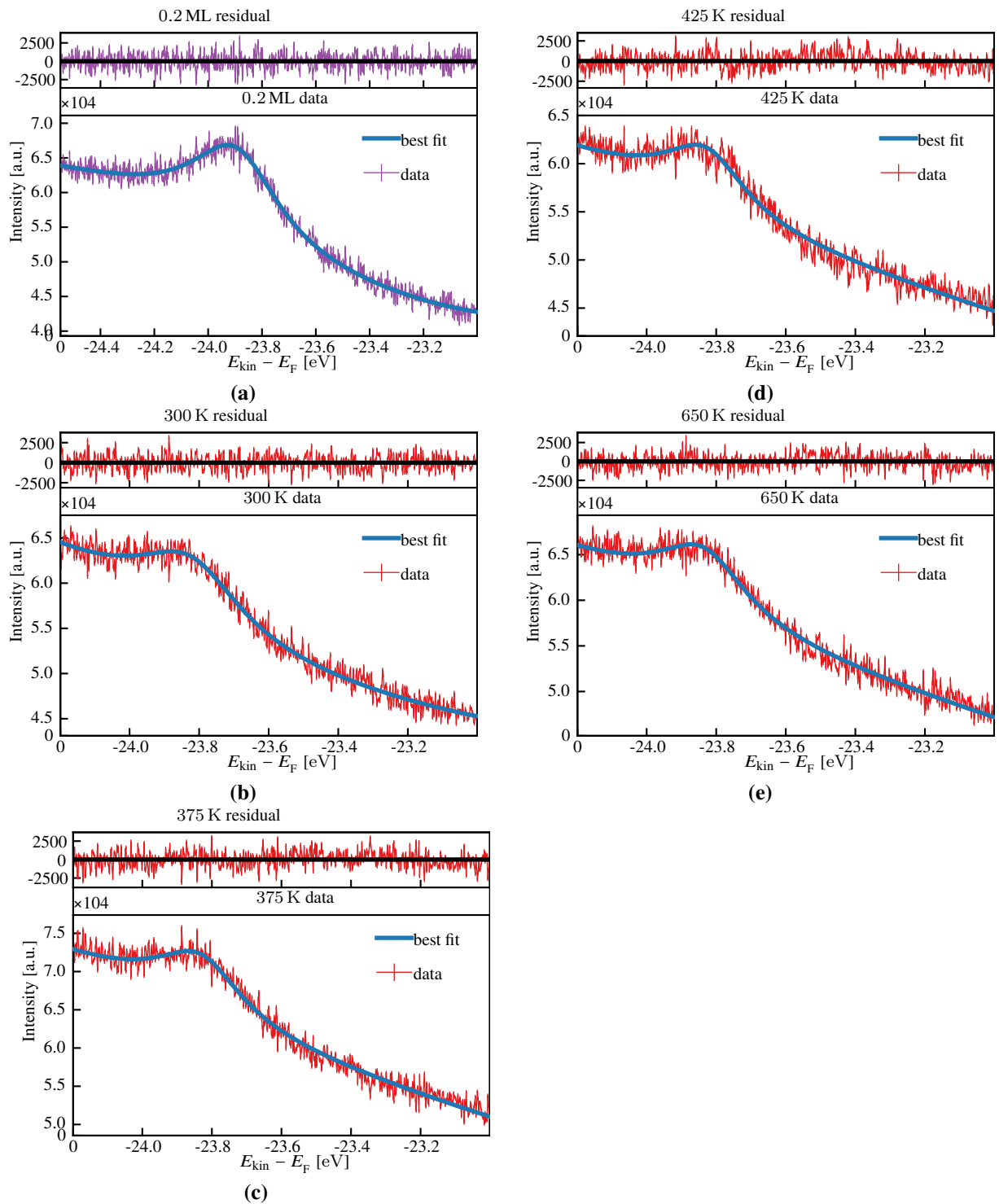


Figure B.9.: Residuals of plots represented in Figure 4.20(a)

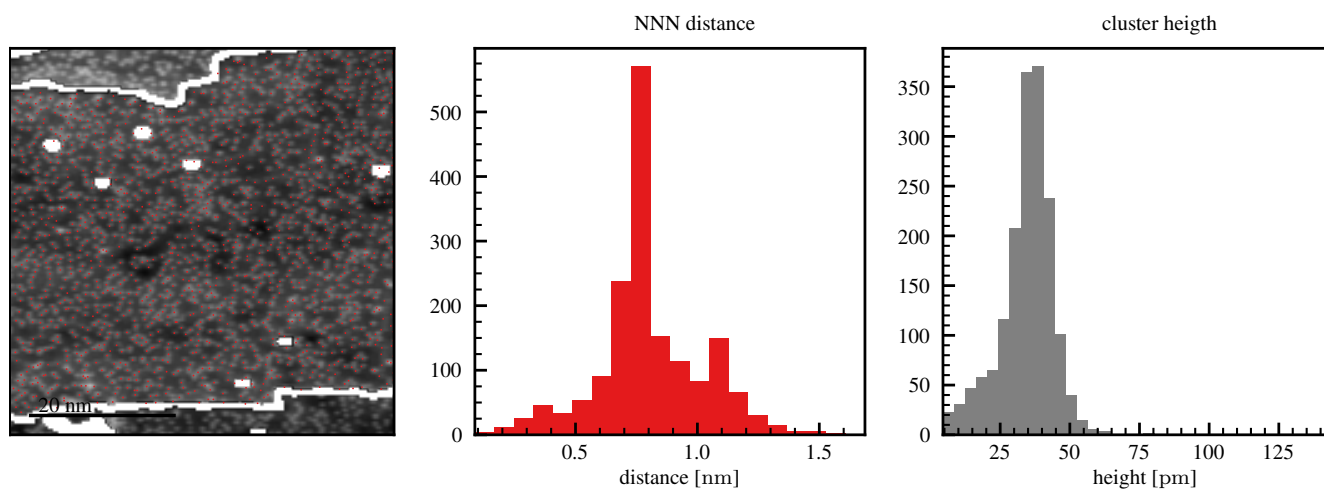


Figure B.10.: Next nearest neighbor (NNN) and height distribution of “cluster-like” structure in STM data of 0.2 ML Bi on Au(111) annealed at 650 K. NNN-distance: 21 bins, bin size 0.08 nm, cluster height: 21 bins, bin size 4 pm. See also Figure 4.20

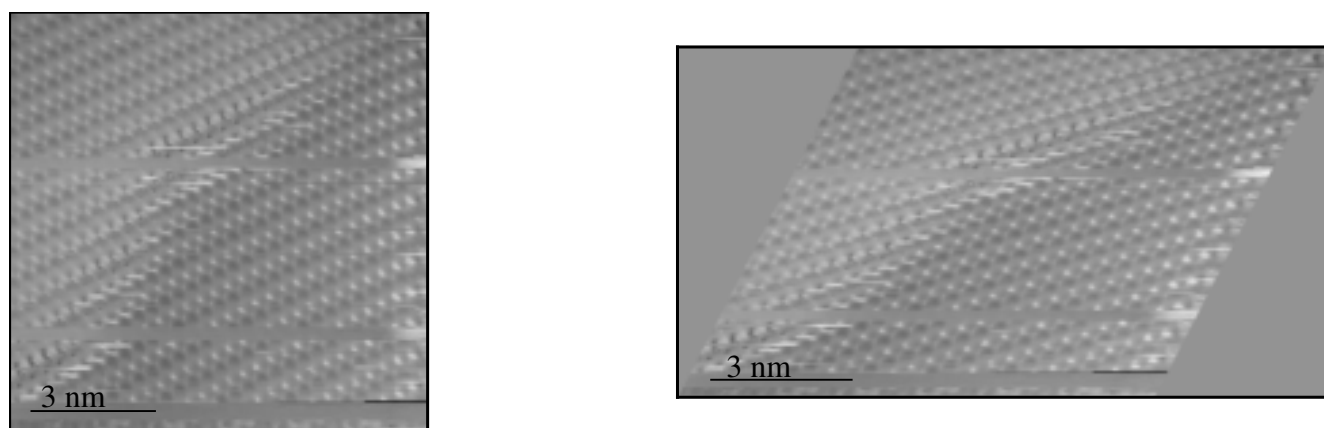


Figure B.11.: Drift correction procedure. Drift correction was done with the help of Gwyddion[94]. Initial lattice vectors of 0.6468 and 0.3657 nm and initial angle of 84.51° (see left hand side) were corrected to 0.4731, 0.4538 nm and 90° (see right hand side), A portion of the image on the right hand side is also shown in Figure 4.21(d)

B.7. Bi on Al₂O₃||Ni₃Al

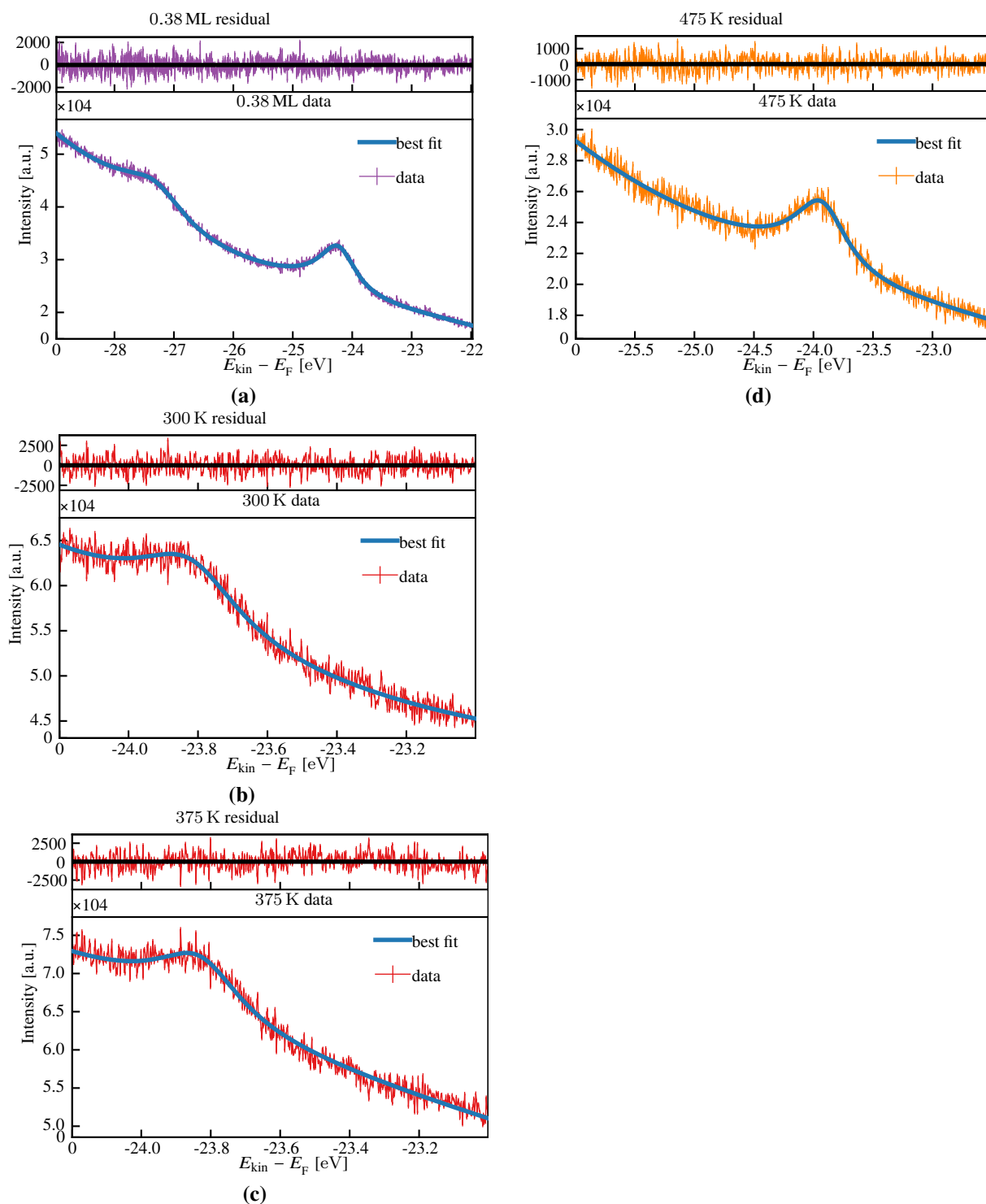


Figure B.12.: Residuals of plots represented in Figure 4.22(a)

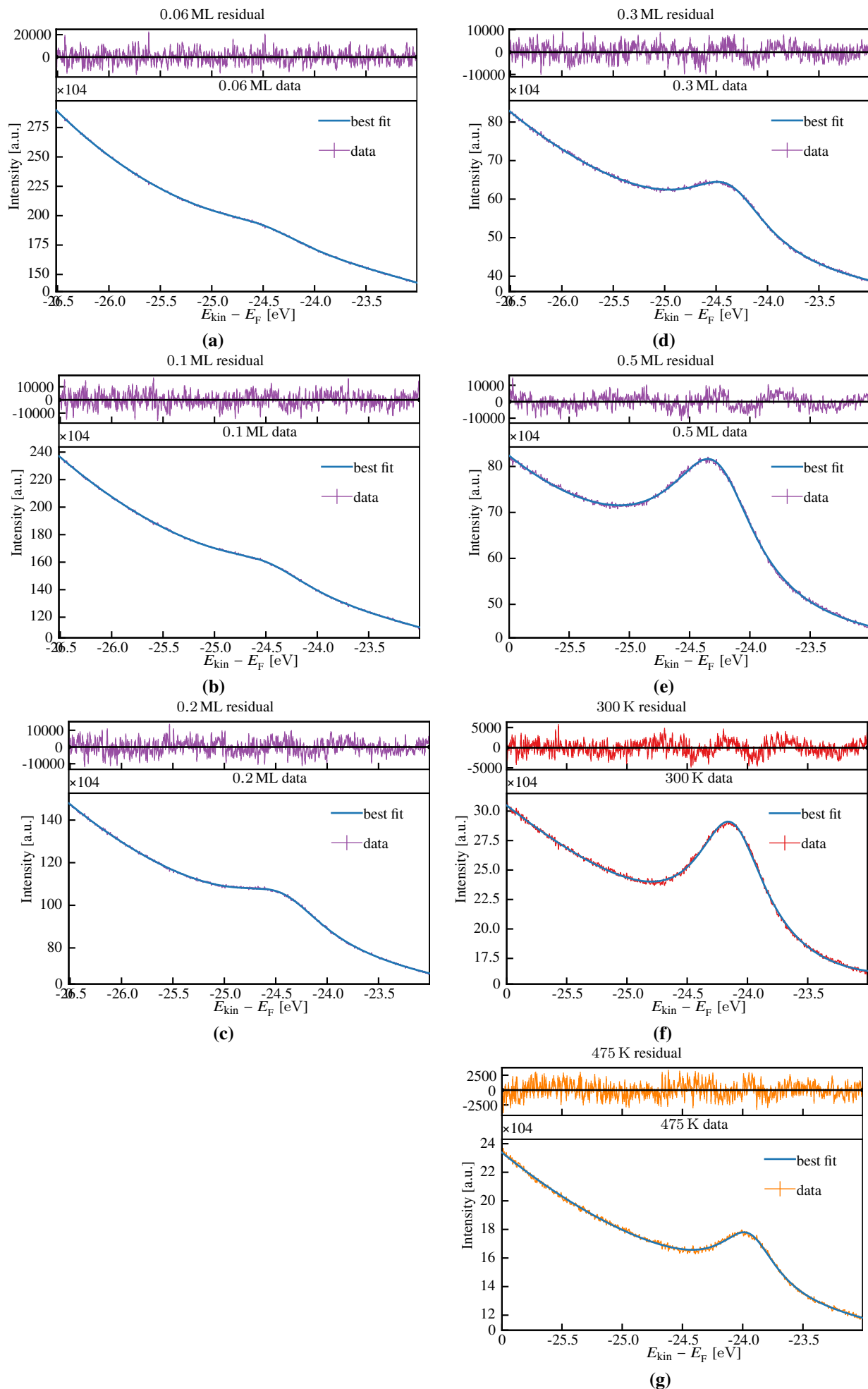


Figure B.13.: Residuals of plots represented in Figure 4.23(a)

Bibliography

- [1] P. M. Solomon. “Device Proposals Beyond Silicon CMOS”. In: *Future Trends in Microelectronics*. Ed. by Serge Luryi, Jimmy Xu, and Alex Zaslavsky. 1st ed. Wiley, June 24, 2010, pp. 127–140. DOI: 10.1002/9780470649343.ch10 (cit. on p. 1).
- [2] Jason Pitters, Jeremiah Croshaw, Roshan Achal, Lucian Livadaru, Samuel Ng, Robert Lupoiu, Taras Chutora, Taleana Huff, Konrad Walus, and Robert A. Wolkow. “Atomically Precise Manufacturing of Silicon Electronics”. In: *ACS Nano* 18.9 (Mar. 5, 2024), pp. 6766–6816. DOI: 10.1021/acsnano.3c10412 (cit. on p. 1).
- [3] Alexey A. Popov, ed. *Endohedral Fullerenes: Electron Transfer and Spin*. Nanostructure Science and Technology. Cham: Springer International Publishing, 2017. DOI: 10.1007/978-3-319-47049-8 (cit. on p. 1).
- [4] Simon C Benjamin, Arzhang Ardavan, G Andrew D Briggs, David A Britz, Daniel Gunlycke, John Jefferson, Mark A G Jones, David F Leigh, Brendon W Lovett, Andrei N Khlobystov, S A Lyon, John J L Morton, Kyriakos Porfyrakis, Mark R Sambrook, and Alexei M Tyryshkin. “Towards a fullerene-based quantum computer”. In: *Journal of Physics: Condensed Matter* 18.21 (May 31, 2006), S867–S883. DOI: 10.1088/0953-8984/18/21/S12 (cit. on p. 1).
- [5] Jeyarama S. Ananta, Biana Godin, Richa Sethi, Loick Moriggi, Xuewu Liu, Rita E. Serda, Ramkumar Krishnamurthy, Raja Muthupillai, Robert D. Bolskar, Lothar Helm, Mauro Ferrari, Lon J. Wilson, and Paolo Decuzzi. “Geometrical confinement of gadolinium-based contrast agents in nanoporous particles enhances T1 contrast”. In: *Nature Nanotechnology* 5.11 (Nov. 2010), pp. 815–821. DOI: 10.1038/nnano.2010.203 (cit. on p. 1).
- [6] Larysa M. Skivka, Svitlana V. Prylutska, Mariia P. Rudyk, Nataliia M. Khranovska, Ievgeniia V. Opeida, Vasyl V. Hurmach, Yuriy I. Prylutsky, Leonid F. Sukhodub, and Uwe Ritter. “C₆₀ fullerene and its nanocomplexes with anticancer drugs modulate circulating phagocyte functions and dramatically increase ROS generation in transformed monocytes”. In: *Cancer Nanotechnology* 9.1 (Dec. 2018), p. 8. DOI: 10.1186/s12645-017-0034-0 (cit. on p. 1).
- [7] Anna Grebinyk. “Synergistic Chemo- and Photodynamic Treatment of Cancer Cells with C₆₀ Fullerene Nanocomplexes”. Artwork Size: 7775 KB Medium: application/pdf Pages: 7775 KB. PhD thesis. [object Object], 2021. DOI: 10.25972/OPUS-22207 (cit. on p. 1).
- [8] Sonia Buckley, Kelley Rivoire, and Jelena Vučković. “Engineered quantum dot single-photon sources”. In: *Reports on Progress in Physics* 75.12 (Dec. 1, 2012), p. 126503. DOI: 10.1088/0034-4885/75/12/126503 (cit. on p. 1).

- [9] Yasuhiko Arakawa and Mark J. Holmes. “Progress in quantum-dot single photon sources for quantum information technologies: A broad spectrum overview”. In: *Applied Physics Reviews* 7.2 (June 1, 2020), p. 021309. DOI: 10.1063/5.0010193 (cit. on p. 1).
- [10] M. Irshad Ahamed, Saahira Ahamed, N. Prathap, M. Nuthal Srinivasan, and C. Mathuvanesan. “Quantum dots and their applications in television display technologies”. In: *World Journal of Advanced Research and Reviews* 16.3 (Dec. 30, 2022), pp. 997–1000. DOI: 10.30574/wjarr.2022.16.3.1455 (cit. on p. 1).
- [11] Puru Jena and Qiang Sun. “Super Atomic Clusters: Design Rules and Potential for Building Blocks of Materials”. In: *Chemical Reviews* 118.11 (June 2018), pp. 5755–5870. DOI: 10.1021/acs.chemrev.7b00524 (cit. on p. 1).
- [12] F. Frank, W. Schulze, B. Tesche, J. Urban, and B. Winter. “Formation of metal clusters and molecules by means of the gas aggregation technique and characterisation of size distribution”. In: *Surface Science* 156 (June 1985), pp. 90–99. DOI: 10.1016/0039-6028(85)90561-8 (cit. on p. 1).
- [13] W.F. Egelhoff. “Core-level binding-energy shifts at surfaces and in solids”. In: *Surface Science Reports* 6.6 (May 1987), pp. 253–415. DOI: 10.1016/0167-5729(87)90007-0 (cit. on p. 1).
- [14] D. Mathur and J. B. Hasted. “Odd and even numbered hydrogen ion clusters”. In: *Nature* 280.5723 (Aug. 1979), pp. 573–574. DOI: 10.1038/280573a0 (cit. on p. 1).
- [15] V. Senz et al. “Core-hole screening as a probe for a metal-to-nonmetal transition in lead clusters”. In: *Physical Review Letters* 102.13 (2009), pp. 3–6. DOI: 10.1103/PhysRevLett.102.138303 (cit. on pp. 1, 73).
- [16] P. Jena, S. N. Khanna, and B. K. Rao, eds. *Physics and Chemistry of Finite Systems: From Clusters to Crystals*. Dordrecht: Springer Netherlands, 1992. DOI: 10.1007/978-94-017-2645-0 (cit. on p. 4).
- [17] K. Rademann, B. Kaiser, U. Even, and F. Hensel. “Size dependence of the gradual transition to metallic properties in isolated mercury clusters”. In: *Physical Review Letters* 59.20 (Nov. 1987), pp. 2319–2321. DOI: 10.1103/PhysRevLett.59.2319 (cit. on pp. 4, 5).
- [18] Bertrand Russell. *History of Western Philosophy*. 0th ed. Routledge, Apr. 2013. DOI: 10.4324/9780203717943 (cit. on p. 3).
- [19] A. Einstein. “Über die von der molekularkinetischen Theorie der Wärme geforderte Bewegung von in ruhenden Flüssigkeiten suspendierten Teilchen”. In: *Annalen der Physik* 322.8 (1905), pp. 549–560. DOI: 10.1002/andp.19053220806 (cit. on p. 3).
- [20] Jürgen Renn. “Die atomistische Revolution”. In: *Physik Journal* 4.3 (Mar. 2005), pp. 53–59 (cit. on p. 3).
- [21] G. Binnig and H. Rohrer. “Scanning tunneling microscopy”. In: *Surface Science* 126.1-3 (Mar. 1983), pp. 236–244. DOI: 10.1016/0039-6028(83)90716-1 (cit. on p. 3).

- [22] Jerome Vernieres, Nathalie Tarrat, Sean Lethbridge, Erica Watchorn-Rokutan, Thomas Slater, David Loffreda, and Richard E. Palmer. “Influence of air exposure on structural isomers of silver nanoparticles”. In: *Communications Chemistry* 6.1 (Jan. 24, 2023), p. 19. DOI: 10.1038/s42004-023-00813-9 (cit. on p. 3).
- [23] David Loffreda, Dawn M. Foster, Richard E. Palmer, and Nathalie Tarrat. “Importance of Defective and Nonsymmetric Structures in Silver Nanoparticles”. In: *The Journal of Physical Chemistry Letters* 12.15 (Apr. 22, 2021), pp. 3705–3711. DOI: 10.1021/acs.jpcllett.1c00259 (cit. on p. 3).
- [24] David Nesvorný, Brian L. Enke, William F. Bottke, Daniel D. Durda, Erik Asphaug, and Derek C. Richardson. “Karin cluster formation by asteroid impact”. In: *Icarus* 183.2 (Aug. 2006), pp. 296–311. DOI: 10.1016/j.icarus.2006.03.008 (cit. on p. 3).
- [25] Vincent Michel, Alexandre Gramfort, Gaël Varoquaux, Evelyn Eger, Christine Keribin, and Bertrand Thirion. “A supervised clustering approach for fMRI-based inference of brain states”. In: *Pattern Recognition* 45.6 (June 2012), pp. 2041–2049. DOI: 10.1016/j.patcog.2011.04.006 (cit. on p. 3).
- [26] ©Copyright Clarivate 2023. All rights reserved. *Web of Science*. 2023. URL: <https://www.webofscience.com/> (cit. on p. 3).
- [27] P. Cotti, H.-J. Güntherodt, P. Munz, P. Oelhafen, and J. Wullschleger. “Photoemission from liquid and solid mercury”. In: *Solid State Communications* 12.7 (Apr. 1973), pp. 635–638. DOI: 10.1016/0038-1098(73)90302-5 (cit. on p. 5).
- [28] W. D. Knight, Keith Clemenger, Walt A. de Heer, Winston A. Saunders, M. Y. Chou, and Marvin L. Cohen. “Electronic Shell Structure and Abundances of Sodium Clusters”. In: *Physical Review Letters* 52.24 (June 1984), pp. 2141–2143. DOI: 10.1103/PhysRevLett.52.2141 (cit. on p. 5).
- [29] Walt A. De Heer. “The physics of simple metal clusters: experimental aspects and simple models”. In: *Reviews of Modern Physics* 65.3 (July 1, 1993), pp. 611–676. DOI: 10.1103/RevModPhys.65.611 (cit. on p. 5).
- [30] Puru Jena. “Beyond the Periodic Table of Elements: The Role of Superatoms”. In: *The Journal of Physical Chemistry Letters* 4.9 (May 2013), pp. 1432–1442. DOI: 10.1021/jz400156t (cit. on pp. 5, 7).
- [31] Keith Clemenger. “Ellipsoidal shell structure in free-electron metal clusters”. In: *Physical Review B* 32.2 (July 1985), pp. 1359–1362. DOI: 10.1103/PhysRevB.32.1359 (cit. on p. 6).
- [32] O. Echt, K. Sattler, and E. Recknagel. “Magic Numbers for Sphere Packings: Experimental Verification in Free Xenon Clusters”. In: *Physical Review Letters* 47.16 (Oct. 1981), pp. 1121–1124. DOI: 10.1103/PhysRevLett.47.1121 (cit. on p. 6).
- [33] M. R. Hoare. “Structure and Dynamics of Simple Microclusters”. In: *Advances in Chemical Physics*. Ed. by I. Prigogine and Stuart A. Rice. Hoboken, NJ, USA: John Wiley & Sons, Inc., Mar. 2007, pp. 49–135. DOI: 10.1002/9780470142592.ch2 (cit. on p. 7).

- [34] Karl-Heinz Meiwes-Broer. *Metal Clusters at Surfaces: Structure, Quantum Properties, Physical Chemistry*. Ed. by A. W. Castleman, R. Stephen Berry, Hellmut Haberland, Joshua Jortner, and Tamotsu Kondow. Springer Series in Cluster Physics. Berlin, Heidelberg: Springer Berlin Heidelberg, 2000. DOI: 10.1007/978-3-642-57169-5 (cit. on pp. 7–9).
- [35] Yoke Khin Yap and Dongyan Zhang. “Physical Vapor Deposition”. In: *Encyclopedia of Nanotechnology*. Ed. by Bharat Bhushan. Dordrecht: Springer Netherlands, 2015, pp. 1–8. DOI: 10.1007/978-94-007-6178-0_362-3 (cit. on p. 8).
- [36] Harald Brune, G. Steven Bales, Joachim Jacobsen, Corrado Boragno, and Klaus Kern. “Measuring surface diffusion from nucleation island densities”. In: *Physical Review B* 60.8 (Aug. 1999), pp. 5991–6006. DOI: 10.1103/PhysRevB.60.5991 (cit. on p. 9).
- [37] Michael Bott, Michael Hohage, Markus Morgenstern, Thomas Michely, and George Comsa. “New Approach for Determination of Diffusion Parameters of Adatoms”. In: *Physical Review Letters* 76.8 (Feb. 1996), pp. 1304–1307. DOI: 10.1103/PhysRevLett.76.1304 (cit. on p. 9).
- [38] Harald Brune, Holger Röder, Corrado Boragno, and Klaus Kern. “Microscopic View of Nucleation on Surfaces”. In: *Physical Review Letters* 73.14 (Oct. 3, 1994), pp. 1955–1958. DOI: 10.1103/PhysRevLett.73.1955 (cit. on p. 9).
- [39] Michael Bowker. “The going rate for catalysts”. In: *Nature Materials* 1.4 (Dec. 2002), pp. 205–206. DOI: 10.1038/nmat774 (cit. on p. 10).
- [40] Thomas W. Hansen, Andrew T. DeLaRiva, Sivakumar R. Challa, and Abhaya K. Datye. “Sintering of Catalytic Nanoparticles: Particle Migration or Ostwald Ripening?” In: *Accounts of Chemical Research* 46.8 (Aug. 2013), pp. 1720–1730. DOI: 10.1021/ar3002427 (cit. on p. 10).
- [41] Shuji Hasegawa. “Reflection High-Energy Electron Diffraction”. In: *Characterization of Materials*. Ed. by Elton N. Kaufmann. Hoboken, NJ, USA: John Wiley & Sons, Inc., Oct. 2012, com139. DOI: 10.1002/0471266965.com139 (cit. on p. 12).
- [42] Michel A. Van Hove, William H. Weinberg, and Chi-Ming Chan. *Low-Energy Electron Diffraction: Experiment, Theory and Surface Structure Determination*. Ed. by Gerhard Ertl and Robert Gomer. Vol. 6. Springer Series in Surface Sciences. Berlin, Heidelberg: Springer Berlin Heidelberg, 1986. DOI: 10.1007/978-3-642-82721-1 (cit. on pp. 12, 13).
- [43] *The Nobel Prize in Physics 1986*. Press release. Oct. 1986 (cit. on p. 14).
- [44] Bert Voigtländer. *Scanning Probe Microscopy: Atomic Force Microscopy and Scanning Tunneling Microscopy*. NanoScience and Technology. Berlin, Heidelberg: Springer Berlin Heidelberg, 2015. DOI: 10.1007/978-3-662-45240-0 (cit. on pp. 15–17).
- [45] J. Bardeen. “Tunnelling from a Many-Particle Point of View”. In: *Physical Review Letters* 6.2 (Jan. 15, 1961), pp. 57–59. DOI: 10.1103/PhysRevLett.6.57 (cit. on p. 16).
- [46] Alex D Gottlieb and Lisa Wesoloski. “Bardeen’s tunnelling theory as applied to scanning tunnelling microscopy: a technical guide to the traditional interpretation”. In: *Nanotechnology* 17.8 (Apr. 28, 2006), R57–R65. DOI: 10.1088/0957-4484/17/8/R01 (cit. on p. 16).

- [47] Paul Adrien Maurice Dirac. “The quantum theory of the emission and absorption of radiation”. In: *Proceedings of the Royal Society of London. Series A, Containing Papers of a Mathematical and Physical Character* 114.767 (Mar. 1927), pp. 243–265. DOI: 10.1098/rspa.1927.0039 (cit. on p. 16).
- [48] J. Tersoff and D. R. Hamann. “Theory and Application for the Scanning Tunneling Microscope”. In: *Physical Review Letters* 50.25 (June 1983), pp. 1998–2001. DOI: 10.1103/PhysRevLett.50.1998 (cit. on p. 17).
- [49] H Neddermeyer. “Scanning tunnelling microscopy of semiconductor surfaces”. In: *Reports on Progress in Physics* 59.6 (June 1996), pp. 701–769. DOI: 10.1088/0034-4885/59/6/001 (cit. on p. 17).
- [50] N. D. Lang. “Vacuum tunneling current from an adsorbed atom”. In: *Physical Review Letters* 55.2 (July 1985), pp. 230–233. DOI: 10.1103/PhysRevLett.55.230 (cit. on p. 17).
- [51] Katsuyoshi Kobayashi and Masaru Tsukada. “Simulation of scanning tunneling microscope image based on electronic states of surface/tip system”. In: *Journal of Vacuum Science & Technology A: Vacuum, Surfaces, and Films* 8.1 (Jan. 1990), pp. 170–173. DOI: 10.1116/1.577057 (cit. on p. 17).
- [52] Jose Manuel Blanco, Fernando Flores, and Rubén Pérez. “STM-theory: Image potential, chemistry and surface relaxation”. In: *Progress in Surface Science* 81.10-12 (Jan. 2006), pp. 403–443. DOI: 10.1016/j.progsurf.2006.07.004 (cit. on p. 17).
- [53] H. Hertz. “Ueber einen Einfluss des ultravioletten Lichtes auf die elektrische Entladung”. In: *Annalen der Physik und Chemie* 267.8 (1887), pp. 983–1000. DOI: 10.1002/andp.18872670827 (cit. on p. 18).
- [54] Wilhelm Hallwachs. “Ueber den Einfluss des Lichtes auf electrostatisch geladene Körper”. In: *Annalen der Physik und Chemie* 269.2 (1888), pp. 301–312. DOI: 10.1002/andp.18882690206 (cit. on p. 18).
- [55] *The Nobel Prize in Physics 1921*. Press release. 1921 (cit. on p. 18).
- [56] Stefan Hüfner. *Photoelectron spectroscopy: principles and applications*. Springer series in solid-state sciences 82. Berlin ; New York: Springer-Verlag, 1995 (cit. on p. 18).
- [57] L. Hedin and J.D. Lee. “Sudden approximation in photoemission and beyond”. In: *Journal of Electron Spectroscopy and Related Phenomena* 124.2-3 (July 2002), pp. 289–315. DOI: 10.1016/S0368-2048(02)00060-9 (cit. on p. 20).
- [58] Friedrich Reinert and Stefan Hüfner. “Photoemission spectroscopy—from early days to recent applications”. In: *New Journal of Physics* 7 (Apr. 2005), pp. 97–97. DOI: 10.1088/1367-2630/7/1/097 (cit. on p. 20).

- [59] Eva Pavarini, Erik Koch, Dieter Vollhardt, Alexander I. Lichtenstein, Institute for Advanced Simulation, German Research School for Simulation Sciences, and Deutsche Forschungsgemeinschaft, eds. *DMFT at 25: infinite dimensions: lecture notes of the Autumn School on Correlated Electrons 2014: at Forschungszentrum Jülich 15-19 September 2014*. Schriften des Forschungszentrums Jülich. Reihe Modeling and Simulation Band 4. Meeting Name: Autumn School on Correlated Electrons. Jülich: Forschungszentrum Jülich, Zentralbibliothek, Verl, 2014 (cit. on p. 20).
- [60] G. D. Mahan. “Theory of Photoemission in Simple Metals”. In: *Physical Review B* 2.11 (Dec. 1970), pp. 4334–4350. DOI: 10.1103/PhysRevB.2.4334 (cit. on p. 20).
- [61] G. D. Mahan. “Collective excitations in x-ray spectra of metals”. In: *Physical Review B* 11.12 (June 1975), pp. 4814–4824. DOI: 10.1103/PhysRevB.11.4814 (cit. on p. 20).
- [62] S Doniach and M Sunjic. “Many-electron singularity in X-ray photoemission and X-ray line spectra from metals”. In: *Journal of Physics C: Solid State Physics* 3.2 (Feb. 1970), pp. 285–291. DOI: 10.1088/0022-3719/3/2/010 (cit. on pp. 20, 79).
- [63] Dominik Wolter. “Mass selected copper clusters on well-ordered aluminum oxide layers”. PhD thesis. TU Dortmund, 2018 (cit. on pp. 22, 61).
- [64] S. Degen, a. Krupski, M. Kralj, a. Langner, C. Becker, M. Sokolowski, and K. Wandelt. “Determination of the coincidence lattice of an ultra thin Al₂O₃ film on Ni₃Al(111)”. In: *Surface Science* 576 (2005), pp. L57–L64. DOI: 10.1016/j.susc.2004.12.020 (cit. on pp. 23, 24, 44, 45).
- [65] A Rosenhahn, J Schneider, C Becker, and K Wandelt. “The formation of Al₂O₃-layers on Ni₃Al(111)”. In: (1999), p. 5. DOI: 10.1016/S0169-4332(98)00669-2 (cit. on pp. 23, 24).
- [66] M. Schmid, G. Kresse, A. Buchsbaum, E. Napetschnig, S. Gritschneider, M. Reichling, and P. Varga. “Nanotemplate with Holes: Ultrathin Alumina on Ni₃Al(111)”. In: *Physical Review Letters* 99.19 (Nov. 2007). DOI: 10.1103/PhysRevLett.99.196104 (cit. on pp. 23, 24).
- [67] S.G. Addepalli, B. Ekstrom, N.P. Magtoto, J.-S. Lin, and J.A. Kelber. “STM atomic-scale characterization of the γ' -Al₂O₃ film on Ni₃Al(111)”. In: *Surface Science* 442.3 (Dec. 1999), pp. 385–399. DOI: 10.1016/S0039-6028(99)00951-6 (cit. on p. 23).
- [68] Mineyuki Arikawa. “Fullerenes—an attractive nano carbon material and its production technology”. In: *Nanotechnology Perceptions* 2.3 (2006), pp. 221–228 (cit. on p. 25).
- [69] A. V. Silant'ev. “Energy spectrum and optical properties of C₆₀ fullerene within the Hubbard model”. In: *Physics of Metals and Metallography* 118.1 (Jan. 2017), pp. 1–9. DOI: 10.1134/S0031918X16100112 (cit. on p. 25).
- [70] Judah Ginsberg. “The Discovery of Fullerenes”. In: *American Chemical Society* (2010), p. 1 (cit. on p. 25).
- [71] H. W. Kroto, J. R. Heath, S. C. O'Brien, R. F. Curl, and R. E. Smalley. “C₆₀: Buckminsterfullerene”. In: *Nature* 318.6042 (Nov. 1985), pp. 162–163. DOI: 10.1038/318162a0 (cit. on p. 25).

- [72] M. S. Dresselhaus, G. Dresselhaus, and P. C. Eklund. *Science of fullerenes and carbon nanotubes*. San Diego: Academic Press, 1996 (cit. on p. 25).
- [73] Ph. Hofmann. “The surfaces of bismuth: Structural and electronic properties”. In: *Progress in Surface Science* 81.5 (Jan. 2006), pp. 191–245. DOI: 10.1016/j.progsurf.2006.03.001 (cit. on pp. 26, 27, 58).
- [74] H. Mönig, J. Sun, Yu. M. Koroteev, G. Bihlmayer, J. Wells, E. V. Chulkov, K. Pohl, and Ph. Hofmann. “Structure of the (111) surface of bismuth: LEED analysis and first-principles calculations”. In: *Physical Review B* 72.8 (Aug. 3, 2005), p. 085410. DOI: 10.1103/PhysRevB.72.085410 (cit. on pp. 26, 58).
- [75] J. Sun, A. Mikkelsen, M. Fuglsang Jensen, Y. M. Koroteev, G. Bihlmayer, E. V. Chulkov, D. L. Adams, Ph. Hofmann, and K. Pohl. “Structural determination of the Bi(110) semimetal surface by LEED analysis and *ab initio* calculations”. In: *Physical Review B* 74.24 (Dec. 6, 2006), p. 245406. DOI: 10.1103/PhysRevB.74.245406 (cit. on pp. 26, 58).
- [76] Pierre De Marcillac, Noël Coron, Gérard Dambier, Jacques Leblanc, and Jean-Pierre Moalic. “Experimental detection of α -particles from the radioactive decay of natural bismuth”. In: *Nature* 422.6934 (Apr. 2003), pp. 876–878. DOI: 10.1038/nature01541 (cit. on p. 26).
- [77] Planck Collaboration et al. “Planck 2018 results. VI. Cosmological parameters”. In: *Astronomy & Astrophysics* 641 (Sept. 2020), A6. DOI: 10.1051/0004-6361/201833910 (cit. on p. 26).
- [78] Donal Keogan and Darren Griffith. “Current and Potential Applications of Bismuth-Based Drugs”. In: *Molecules* 19.9 (Sept. 23, 2014), pp. 15258–15297. DOI: 10.3390/molecules190915258 (cit. on p. 26).
- [79] Thomas E Sox and Christy A Olson. “Binding and killing of bacteria by bismuth subsalicylate”. In: *Antimicrobial agents and chemotherapy* 33.12 (1989), pp. 2075–2082 (cit. on p. 26).
- [80] Hongzhe Sun. *Biological chemistry of arsenic, antimony and bismuth*. John Wiley & Sons, 2010 (cit. on p. 26).
- [81] Philip C. Andrews, Victoria L. Blair, Richard L. Ferrero, Peter C. Junk, Lukasz Kedzierski, and Roshani M. Peiris. “Bismuth(III) β -thioxoketonates as antibiotics against *Helicobacter pylori* and as anti-leishmanial agents”. In: *Dalton Trans.* 43.3 (2014), pp. 1279–1291. DOI: 10.1039/C3DT52544A (cit. on p. 26).
- [82] Ruizhuo Ouyang, Yang Yang, Xiao Tong, Kai Feng, Yaoqin Yang, Huihong Tao, Xiaoshen Zhang, Tianyu Zong, Penghui Cao, Fei Xiong, Ning Guo, Yuhao Li, Yuqing Miao, and Shuang Zhou. “Potent anticancer activity of a new bismuth (III) complex against human lung cancer cells”. In: *Journal of Inorganic Biochemistry* 168 (Mar. 2017), pp. 18–26. DOI: 10.1016/j.jinorgbio.2016.12.006 (cit. on p. 26).
- [83] Khursheed Ahmad. “Bismuth Halide Perovskites for Photovoltaic Applications”. In: *Bismuth - Fundamentals and Optoelectronic Applications*. Ed. by Yanhua Luo, Jianxiang Wen, and Jianzhong Zhang. IntechOpen, Dec. 2, 2020. DOI: 10.5772/intechopen.92413 (cit. on p. 26).

- [84] Jizhou He, Xiaodong Hu, Zonghao Liu, Wei Chen, and Giulia Longo. “Prospect for Bismuth/Antimony Chalcogenides-Based Solar Cells”. In: *Advanced Functional Materials* 33.48 (Nov. 2023), p. 2306075. DOI: 10.1002/adfm.202306075 (cit. on p. 26).
- [85] Mercuri Kanatzidis, Hongzhe Sun, and Stefanie Dehnen. “Bismuth—The Magic Element”. In: *Inorganic Chemistry* 59.6 (Mar. 16, 2020), pp. 3341–3343. DOI: 10.1021/acs.inorgchem.0c00222 (cit. on p. 26).
- [86] Mauro Mato and Josep Cornella. “Bismuth in Radical Chemistry and Catalysis”. In: *Angewandte Chemie International Edition* 63.8 (Feb. 19, 2024), e202315046. DOI: 10.1002/anie.202315046 (cit. on p. 26).
- [87] Neil W. Ashcroft and N. David Mermin. *Solid state physics*. New York: Holt, Rinehart and Winston, 1976. 826 pp. (cit. on p. 27).
- [88] Irene Aguilera, Christoph Friedrich, and Stefan Blügel. “Electronic phase transitions of bismuth under strain from relativistic self-consistent G W calculations”. In: *Physical Review B* 91.12 (Mar. 18, 2015), p. 125129. DOI: 10.1103/PhysRevB.91.125129 (cit. on p. 27).
- [89] Dimitris A. Papaconstantopoulos. *Handbook of the Band Structure of Elemental Solids: From Z = 1 To Z = 112*. Boston, MA: Springer US, 2015. DOI: 10.1007/978-1-4419-8264-3 (cit. on p. 27).
- [90] Torsten Richter. “Untersuchung von deponierten und gewachsenen Silberclustern auf Fullerschichten mittels Rastertunnelmikroskopie”. PhD thesis. 2007 (cit. on pp. 30, 31, 33).
- [91] James C. Withers, Raouf O. Loutfy, and Timothy P. Lowe. “Fullerene Commercial Vision”. In: *Fullerene Science and Technology* 5.1 (Jan. 1997), pp. 1–31. DOI: 10.1080/15363839708011971 (cit. on p. 30).
- [92] W. Z. Li, S. S. Xie, L. X. Qian, B. H. Chang, B. S. Zou, W. Y. Zhou, R. A. Zhao, and G. Wang. “Large-Scale Synthesis of Aligned Carbon Nanotubes”. In: *Science* 274.5293 (Dec. 6, 1996), pp. 1701–1703. DOI: 10.1126/science.274.5293.1701 (cit. on p. 30).
- [93] UKL Technical Services. *Data Temperature handbook*. Vol. TH0906 V2.1. Labfacility Ltd, Middlesex, UK, 2006 (cit. on p. 30).
- [94] David Nečas and Petr Klapetek. “Gwyddion: an open-source software for SPM data analysis”. In: *Central European Journal of Physics* 10 (1 2012), pp. 181–188. DOI: 10.2478/s11534-011-0096-2 (cit. on pp. 32, 41, 42, 80, 92).
- [95] Shengzhong Liu, Ying-Jie Lu, Manfred M. Kappes, and James A. Ibers. “The Structure of the C₆₀ Molecule: X-Ray Crystal Structure Determination of a Twin at 110 K”. In: *Science* 254.5030 (Oct. 18, 1991), pp. 408–410. DOI: 10.1126/science.254.5030.408 (cit. on p. 33).
- [96] Stefanie Duffe. “Thermally activated processes and electronic properties of size selected Ag clusters and grown metal islands on C60 functionalized surfaces”. PhD thesis. Technische Universität Dortmund, May 6, 2009. DOI: 10.17877/DE290R-14222 (cit. on p. 33).

- [97] Ts Padmore, G Thornton, and Ha Padmore. “The surface electronic structure of Ag(001) and Ag(111) studied with multichannel detection angle-resolved photoemission”. In: *Vacuum* 38.4 (Jan. 1988), pp. 261–265. DOI: 10.1016/0042-207X(88)90057-7 (cit. on p. 34).
- [98] R. Otero, A.L. Vázquez De Parga, and J.M. Gallego. “Electronic, structural and chemical effects of charge-transfer at organic/inorganic interfaces”. In: *Surface Science Reports* 72.3 (July 2017), pp. 105–145. DOI: 10.1016/j.surfrep.2017.03.001 (cit. on p. 34).
- [99] Dennis L. Lichtenberger, Mark E. Jatzko, Kenneth W. Nebesny, Charles D. Ray, Donald R. Huffman, and Lowell D. Lamb. “The Ionizations of C₆₀ in the Gas Phase and in Thin Solid Films.” In: *MRS Proceedings* 206 (1990), p. 673. DOI: 10.1557/PROC-206-673 (cit. on p. 34).
- [100] C. Becker. “UHV Surface Preparation Methods”. In: *Encyclopedia of Interfacial Chemistry*. Elsevier, 2018, pp. 580–590. DOI: 10.1016/B978-0-12-409547-2.11050-9 (cit. on p. 34).
- [101] Heekeun Shin, A. Schwarze, R. D. Diehl, K. Pussi, A. Colombier, É. Gaudry, J. Ledieu, G. M. McGuirk, L. N. Serkovic Loli, V. Fournée, L. L. Wang, G. Schull, and R. Berndt. “Structure and dynamics of C₆₀ molecules on Au(111)”. In: *Physical Review B* 89.24 (June 2014), p. 245428. DOI: 10.1103/PhysRevB.89.245428 (cit. on pp. 37, 38).
- [102] Michael Paßens and Silvia Karthäuser. “Interfacial and intermolecular interactions determining the rotational orientation of C₆₀ adsorbed on Au(111)”. In: *Surface Science* 642 (Dec. 2015), pp. 11–15. DOI: 10.1016/j.susc.2015.07.025 (cit. on p. 38).
- [103] Mitchell P. Yothers, Aaron E. Browder, and Lloyd A. Bumm. “Real-space post-processing correction of thermal drift and piezoelectric actuator nonlinearities in scanning tunneling microscope images”. In: *Review of Scientific Instruments* 88.1 (Jan. 2017), p. 013708. DOI: 10.1063/1.4974271 (cit. on p. 41).
- [104] Joseph A. Smerdon, Vincent Fournée, Julian Ledieu, and Katariina Pussi. “C₆₀ Adsorbed on Ni(111) and Co(0001) Surfaces”. In: *The Journal of Physical Chemistry C* 127.3 (Jan. 26, 2023), pp. 1655–1664. DOI: 10.1021/acs.jpcc.2c07056 (cit. on p. 43).
- [105] Sebastian Gritschneider, Stefan Degen, Conrad Becker, Klaus Wandelt, and Michael Reichling. “Atomic structure of a stripe phase on Al₂O₃ / Ni₃Al (111) revealed by scanning force microscopy”. In: *Physical Review B* 76.1 (July 2007). DOI: 10.1103/PhysRevB.76.014123 (cit. on p. 43).
- [106] C Becker, A Rosenhahn, A Wiltner, K von Bergmann, J Schneider, P Pervan, M Milun, M Kralj, and K Wandelt. “Al₂O₃-films on Ni₃Al(111): a template for nanostructured cluster growth”. In: *New Journal of Physics* 4 (Oct. 2002), pp. 75–75. DOI: 10.1088/1367-2630/4/1/375 (cit. on p. 45).
- [107] A. Rosenhahn, J. Schneider, J. Kandler, C. Becker, and K. Wandelt. “Interaction of oxygen with Ni₃Al(111) at 300 K and 1000 K”. In: *Surface Science* 433-435 (Aug. 1999), pp. 705–710. DOI: 10.1016/S0039-6028(99)00126-0 (cit. on p. 46).

- [108] Thomas Andreev, Ingo Barke, and Heinz Hövel. “Adsorbed rare-gas layers on Au(111): Shift of the Shockley surface state studied with ultraviolet photoelectron spectroscopy and scanning tunneling spectroscopy”. In: *Physical Review B* 70.20 (Nov. 2004), p. 205426. DOI: 10.1103/PhysRevB.70.205426 (cit. on p. 47).
- [109] S.Å. Lindgren and L. Walldén. “Cu surface state and Cs valence electrons in photoelectron spectra from the Cu(111)/Cs adsorption system”. In: *Solid State Communications* 28.3 (Oct. 1978), pp. 283–286. DOI: 10.1016/0038-1098(78)90644-0 (cit. on p. 47).
- [110] R Hesper, L. H Tjeng, and G. A Sawatzky. “Strongly reduced band gap in a correlated insulator in close proximity to a metal”. In: *Europhysics Letters (EPL)* 40.2 (Oct. 1997), pp. 177–182. DOI: 10.1209/epl/i1997-00442-2 (cit. on pp. 48, 49).
- [111] Isabel Fernández Torrente, Katharina J Franke, and Jose Ignacio Pascual. “Spectroscopy of C₆₀ single molecules: the role of screening on energy level alignment”. In: *Journal of Physics: Condensed Matter* 20.18 (May 2008), p. 184001. DOI: 10.1088/0953-8984/20/18/184001 (cit. on pp. 48, 49).
- [112] Wolfgang Demtröder. *Experimentalphysik. 2: Elektrizität und Optik: mit 19 Tabellen, zahlreichen durchgerechneten Beispielen und 145 Übungsaufgaben mit ausführlichen Lösungen*. 4., überarb. u. erw. Aufl. Berlin [u.a]: Springer, 2006. 488 pp. (cit. on p. 48).
- [113] John David Jackson. *Classical electrodynamics*. New York: Wiley, 1962. 641 pp. (cit. on p. 49).
- [114] R. Antoine, Ph. Dugourd, D. Rayane, E. Benichou, M. Broyer, F. Chandezon, and C. Guet. “Direct measurement of the electric polarizability of isolated C₆₀ molecules”. In: *The Journal of Chemical Physics* 110.19 (May 15, 1999), pp. 9771–9772. DOI: 10.1063/1.478944 (cit. on p. 49).
- [115] H. Hövel, B. Grimm, M. Pollmann, and B. Reihl. “Cluster-Substrate Interaction on a Femtosecond Time Scale Revealed by a High-Resolution Photoemission Study of the Fermi-Level Onset”. In: *Physical Review Letters* 81.21 (Nov. 23, 1998), pp. 4608–4611. DOI: 10.1103/PhysRevLett.81.4608 (cit. on p. 49).
- [116] Xinghua Lu, M. Grobis, K. H. Khoo, Steven G. Louie, and M. F. Crommie. “Charge transfer and screening in individual C₆₀ molecules on metal substrates: A scanning tunneling spectroscopy and theoretical study”. In: *Physical Review B* 70.11 (Sept. 24, 2004), p. 115418. DOI: 10.1103/PhysRevB.70.115418 (cit. on pp. 49, 73).
- [117] EVOCHEM GmbH. *Evochem Advanced Materials GmbH*. "<https://www.evo-chem.de/>". 2020 (cit. on p. 50).
- [118] Günter Sauerbrey. “Verwendung von Schwingquarzen zur Wägung dünner Schichten und zur Mikrowägung”. In: *Zeitschrift für Physik* 155.2 (Apr. 1959), pp. 206–222. DOI: 10.1007/BF01337937 (cit. on p. 51).
- [119] Diethelm Johannsmann. *The Quartz Crystal Microbalance in Soft Matter Research. Soft and Biological Matter*. Cham: Springer International Publishing, 2015. DOI: 10.1007/978-3-319-07836-6 (cit. on p. 51).

- [120] INFICON GmbH. *Instruments For Intelligent Control*. "https://www.inficon.com/". 2000 (cit. on p. 51).
- [121] Jeong Heum Jeon, Kyung Hoon Chung, Howon Kim, and Se-Jong Kahng. "Corner hole adatom stacking fault structure of Bi on Au(111)". In: *Surface Science* 603.1 (Jan. 2009), pp. 145–150. DOI: 10.1016/j.susc.2008.10.036 (cit. on p. 53).
- [122] Naoya Kawakami, Chun-Liang Lin, Kazuaki Kawahara, Maki Kawai, Ryuichi Arafune, and Noriaki Takagi. "Structural evolution of Bi thin films on Au(111) revealed by scanning tunneling microscopy". In: *Physical Review B* 96.20 (Nov. 2017), p. 205402. DOI: 10.1103/PhysRevB.96.205402 (cit. on pp. 53, 58).
- [123] Bingchen He, Guo Tian, Jian Gou, Baoxing Liu, Kongchao Shen, Qiwei Tian, Zhengqing Yu, Fei Song, Haipeng Xie, Yongli Gao, Yunhao Lu, Kehui Wu, Lan Chen, and Han Huang. "Structural and electronic properties of atomically thin Bismuth on Au(111)". In: *Surface Science* 679 (Jan. 2019), pp. 147–153. DOI: 10.1016/j.susc.2018.09.005 (cit. on pp. 53, 55, 58).
- [124] Hans Warlimont and Werner Martienssen, eds. *Springer Handbook of Materials Data*. Springer Handbooks. Cham: Springer International Publishing, 2018. DOI: 10.1007/978-3-319-69743-7 (cit. on p. 53).
- [125] John C. Fuggle and Nils Mårtensson. "Core-level binding energies in metals". In: *Journal of Electron Spectroscopy and Related Phenomena* 21.3 (1980), pp. 275–281 (cit. on pp. 54, 55).
- [126] Julian Andreas Hochhaus. *lmfitxps*. Version 1.1.0. July 2023. DOI: 10.5281/zenodo.8181379 (cit. on p. 55).
- [127] Matt Newville et al. *lmfit/lmfit-py: 1.2.2*. Version 1.2.2. July 2023. DOI: 10.5281/zenodo.8145703 (cit. on p. 55).
- [128] V. Fournée, P. J. Pinhero, J. W. Andereg, T. A. Lograsso, A. R. Ross, P. C. Canfield, I. R. Fisher, and P. A. Thiel. "Electronic structure of quasicrystalline surfaces: Effects of surface preparation and bulk structure". In: *Physical Review B* 62.21 (Dec. 1, 2000), pp. 14049–14060. DOI: 10.1103/PhysRevB.62.14049 (cit. on pp. 55, 79).
- [129] Franciscus Martinus Frederikus de Groot, Akio Kotani, and Frank de Groot. *Core level spectroscopy of solids*. Advances in condensed matter science 6. Boca Raton, Fla.: CRC Press, 2008. 490 pp. (cit. on p. 56).
- [130] C. Becker, K. von Bergmann, A. Rosenhahn, J. Schneider, and K. Wandelt. "Preferential cluster nucleation on long-range superstructures on Al₂O₃/Ni₃Al(111)". In: *Surface Science* 486.1-2 (July 2001), pp. L443–L448. DOI: 10.1016/S0039-6028(01)01052-4 (cit. on p. 61).
- [131] Keith D Bonin and Vitaly V Kresin. *Electric-Dipole Polarizabilities of Atoms, Molecules, and Clusters*. WORLD SCIENTIFIC, Oct. 1997. DOI: 10.1142/2962 (cit. on p. 63).
- [132] Ingo Barke. "'Morphology and electronic structure of gold clusters on graphite'". PhD thesis. Universität Dortmund, Jan. 14, 2005. DOI: 10.17877/DE290R-14835 (cit. on pp. 63, 64).

- [133] Michael Seidl, John P. Perdew, Marta Brajczewska, and Carlos Fiolhais. “Ionization energy and electron affinity of a metal cluster in the stabilized jellium model: Size effect and charging limit”. In: *The Journal of Chemical Physics* 108.19 (May 15, 1998), pp. 8182–8189. DOI: 10.1063/1.476173 (cit. on p. 66).
- [134] M. Astruc Hoffmann, G. Wrigge, and B. V. Issendorff. “Photoelectron spectroscopy of Al 32000 - : Observation of a "Coulomb staircase" in a free cluster”. In: *Physical Review B* 66.4 (July 16, 2002), p. 041404. DOI: 10.1103/PhysRevB.66.041404 (cit. on p. 66).
- [135] H Hovel, B Grimm, M Pollmann, and B Reihl. “Femtosecond dynamics of final-state effects in the valence band photoemission of silver clusters on a graphite substrate”. In: *The European Physical Journal D* (1998) (cit. on p. 67).
- [136] Siegfried Flügge. *Rechenmethoden der Elektrodynamik: Aufgaben mit Lösungen*. Berlin ; New York: Springer-Verlag, 1986. 304 pp. (cit. on p. 67).
- [137] Dana Longcope. *Capacitance of a sphere near a ground plane — images charges to infinity*. Jan. 17, 2019. URL: https://solar.physics.montana.edu/dana/ph519/sph_cap.pdf (cit. on pp. 68, 69).
- [138] S Krause, M B Casu, A Schöll, and E Umbach. “Determination of transport levels of organic semiconductors by UPS and IPS”. In: *New Journal of Physics* 10.8 (Aug. 2008), p. 085001. DOI: 10.1088/1367-2630/10/8/085001 (cit. on p. 75).
- [139] Paul H.C. Eilers, Valentin Pesendorfer, and Rogerio Bonifacio. “Automatic smoothing of remote sensing data”. In: *2017 9th International Workshop on the Analysis of Multitemporal Remote Sensing Images (MultiTemp)*. 2017 9th International Workshop on the Analysis of Multitemporal Remote Sensing Images (MultiTemp). Brugge: IEEE, June 2017, pp. 1–3. DOI: 10.1109/MultiTemp.2017.8076705 (cit. on pp. 75–77).
- [140] Paul H. C. Eilers. “A Perfect Smoother”. In: *Analytical Chemistry* 75.14 (July 2003), pp. 3631–3636. DOI: 10.1021/ac034173t (cit. on pp. 75, 76).
- [141] valpesendorfer. *vam.whittaker*. URL: <https://github.com/WFP-VAM/vam.whittaker> (cit. on p. 75).
- [142] Michael Schmid, David Rath, and Ulrike Diebold. “Why and How Savitzky–Golay Filters Should Be Replaced”. In: *ACS Measurement Science Au* 2.2 (Apr. 20, 2022), pp. 185–196. DOI: 10.1021/acsmesuresciau.1c00054 (cit. on p. 76).
- [143] Clement Atzberger and Paul H.C. Eilers. “A time series for monitoring vegetation activity and phenology at 10-daily time steps covering large parts of South America”. In: *International Journal of Digital Earth* 4.5 (Sept. 2011), pp. 365–386. DOI: 10.1080/17538947.2010.505664 (cit. on p. 77).
- [144] Alexander Kononov. *peak_onset*. URL: https://github.com/Hexanders/peak_onset (cit. on p. 77).

- [145] Matthew Newville, Till Stensitzki, Daniel B. Allen, and Antonino Ingargiola. *LMFIT: Non-Linear Least-Square Minimization and Curve-Fitting for Python*. Version 0.8.0. Sept. 2014. DOI: 10.5281/zenodo.11813 (cit. on p. 78).
- [146] Andrea Damascelli, Zahid Hussain, and Zhi-Xun Shen. “Angle-resolved photoemission studies of the cuprate superconductors”. In: *Reviews of Modern Physics* 75.2 (Apr. 2003), pp. 473–541. DOI: 10.1103/RevModPhys.75.473 (cit. on p. 77).
- [147] Julian Andreas Hochhaus and Hideki Nakajima. *LG4X-V2*. DOI: 10.5281/zenodo.7777423 (cit. on p. 78).
- [148] G. K. Wertheim and P. H. Citrin. “Fermi surface excitations in X-ray photoemission line shapes from metals”. In: *Photoemission in Solids I*. Ed. by M. Cardona and L. Ley. Vol. 26. Series Title: Topics in Applied Physics. Berlin, Heidelberg: Springer Berlin Heidelberg, 1978, pp. 197–236. DOI: 10.1007/3540086854_5 (cit. on p. 79).
- [149] Alexander Kononov. *stm-cluster-heightzer*. URL: <https://github.com/Hexanders/stm-cluster-heightzer> (cit. on p. 80).
- [150] Franz Aurenhammer. “Voronoi diagrams—a survey of a fundamental geometric data structure”. In: *ACM Computing Surveys* 23.3 (Sept. 1991), pp. 345–405. DOI: 10.1145/116873.116880 (cit. on p. 81).
- [151] Marcin Wojdyr. “*Fityk*: a general-purpose peak fitting program”. In: *Journal of Applied Crystallography* 43.5 Part 1 (Oct. 2010), pp. 1126–1128. DOI: 10.1107/S0021889810030499 (cit. on pp. 84–87, 89).

List of Acronyms

LN ₂	liquid nitrogen. 2, 31, 32, 34, 39–43, 48, 54, 55, 57, 59–61
ML	monolayer. 9, 31–44, 47, 51–61, 63–66, 70, 71, 86, 89–94, VI
AFM	atomic force microscope. 31–33, 45, V
ARPES	angle resolved photoelectron spectroscopy. 47
DFT	density functional theory. 24, 27, 38
DOS	density of states. 15
DS	Doniach-Sunjic. 54, 55, 57, 59, 79
EB-PVD	electron beam physical vapor deposition. 7, 8
fcc	face centered cubic. 73
FWHM	full width at half maximum. 55, 57, 60, 61, 79
HCP	hexagonal close packed. 33, 36, 37, 41, 43, 48, 49
HOMO	highest occupied molecular orbital. 2, 25, 29, 30, 34–36, 40, 45–49, 63, 73, 75, 76, 88, 111, III, VI
HOPG	highly ordered pyrolytic graphite. 31, 32, 49, 90, VI
ICP-MS	inductively coupled plasma mass spectrometry. 50
ICP-OES	inductively coupled plasma optical emission spectroscopy. 50
LEED	low-energy electron diffraction. 2, 11–13, 21, 23, 24, 38, 45, 50, 52, 53, 55, V
LHe	liquid helium. 36
LUMO	lowest unoccupied molecular orbital. 25
MCP	multichannel plates. 19
MTNT	metal-to-nonmetal transition. 5, 73
NMR	nuclear magnetic resonance. 1

PES	photoemission spectroscopy. 18, 19, 49, 75, 77
PID	proportional-integral-differential controller. 51, 54
PoP	peak onset position. 34, 35, 90
PVD	physical vapor deposition. 7, 8, 10, 50
QCM	quartz crystal microbalance. 30, 31, 33, 51–53, V
RT	room temperature. 31–34, 39, 40, 42, 43, 48, 49, 56–58, 88, 90
SPM	scanning probe microscope. 80
STEM	scanning transmission electron microscopy. 3
STM	scanning tunneling microscope. 2, 3, 10, 11, 14, 16–18, 21, 23, 24, 29–45, 48, 50, 51, 53–65, 68, 70, 73, 79–81, 89, 92, III, V, VI
STS	scanning tunneling spectroscopy. 49, 73
UHV	ultra-high vacuum. 2, 7, 21, 30, 31, 39, 50–54, 90, III
UPS	ultraviolet photoelectron spectroscopy. 2, 11, 21, 29, 30, 32, 34–36, 39–50, 53–59, 69, 72, 73, 75–79, 88, 90, 111, III, VI
XPS	x-ray photoelectron spectroscopy. 1, 55, 79

List of Symbols

E_F	Fermi energy. 15–17, 19, 34, 35, 39, 46, 47, 54, 55, 57, 59–61, 76, 78, 79, 88, 90, 91, 93, 94
E_{Ar^+}	Ion energy of argon atoms used during sputtering process.. 39
I_p	ionization potential. 4, 5
J	unit of energy in International System of Units (SI) . 5
M	molar mass. 4
N_A	Avogadro constant. 4
$\rho(E)$	Density of states. 15
ρ	density. 4
E_{exc}	UPS excitation energy. In the present work, two different lines of helium discharge lamps were used HeI α : $E_{exc} = 21.22$ eV and HeII α : $E_{exc} = 40.81$ eV. 34, 35, 39, 88, 90, 111
E_{onset}	Energy position of the onset of the HOMO peak of the C ₆₀ molecule in an UPS spectrum. 35, 40, 47, 49, 76
E_{HOMO}	Energy position of the highest occupied molecular orbital. 39, 111
E_{infl}	Energy position of the inflection point of E_{HOMO} peak. 35, 40, 47, 76
HeII α	Spectral line of He gas at the energy of 40.81 eV. Less than 5 % of the intensity of HeI α . 54, 55, 78, 79, 111
HeI α	Spectral line of He gas at the energy of 21.22 eV. This line is most intense. 34, 35, 39, 78, 88, 111
I_{sput}	Ion current measured on the surface of the sample during the sputtering process with argon ions.. 34, 35, 39
ϵ_0	vacuum permittivity. $\epsilon_0 = 8.854\,187\,812\,8(13) \times 10^{-12}$ F/m. 5, 66–68, 82
a_0	Bohr radius. $5.291\,772\,109\,03(80) \times 10^{-11}$ m. 66
e^-	elementary charge. 5, 48
k_B	Boltzmann constant. 8, 9, 16, 78
r_s	Wigner-Seitz radius. 4, 66
w	work function. 5
eV	electronvolt, unit of energy $1\text{ eV} = 1.602\,176\,634 \times 10^{-19}$ J. 5

Acknowledgments

An dieser Stelle möchte ich mich bei allen bedanken, die mich über die Jahre unterstützt haben.

Ein besonders großer Dank gilt meinem Betreuer, Prof. Dr. Heinz Hövel, für die Möglichkeit, in seiner Arbeitsgruppe an diesem spannenden Thema zu arbeiten. Mit seinem beeindruckenden Wissen und seiner umfangreichen Erfahrung stand er mir trotz seiner zahlreichen Aufgaben stets zur Seite, wenn es im Labor oder bei der Auswertung schwierig wurde. Seine positive und ermutigende Art hat mir dabei sehr geholfen.

Prof. Dr. Ilya Akimov danke ich für sein Interesse an meiner Arbeit und seine Bereitschaft, trotz der intensiven Phase seiner eigenen Forschungsarbeit nach Einreichung der Arbeit das Zweitgutachten ohne Zeitverzug zu erstellen.

Prof. Dr. Götz S. Uhrig und Dr. Bärbel Siegmann danke ich für ihre Zeit und ihre Mitwirkung in meiner Prüfungskommission.

Den Mitgliedern der Arbeitsgruppen von Prof. Dr. Heinz Hövel und Prof. Dr. Metin Tolan möchte ich für die stets angenehme Atmosphäre sowohl bei der Arbeit als auch bei den außerdienstlichen Aktivitäten danken. Ein besonderer Dank gilt Dr. Christian Sternemann für seine Zeit und wertvollen Ratschläge bei der Vorbereitung meines Disputationsvortrags.

Mein herzlicher Dank geht an Dr. Dominik Wolter und Dr. Stefanie Riese für ihre Einführung in das Laborleben eines Physikers und ihre Unterstützung, besonders zu Beginn meiner Promotion.

Ebenso danke ich unseren Technikern Thorsten Witt und Georg Jülicher, die bei zahlreichen elektronischen und mechanischen Problemen immer eine Lösung fanden. Daniel Tüttmann danke ich für die zuverlässige und konstante Versorgung mit flüssigem Helium und Stickstoff, die für meine Arbeit von zentraler Bedeutung war. Vielen Dank an Susanne Kralemann und die mechanische Werkstatt für die harte Arbeit und ihre beeindruckende Fähigkeit, komplexe mechanische Arbeiten an der Vakuumapparatur durchzuführen. Ohne ihr schnelles und professionelles Engagement bei der Reparatur des Manipulators wäre dieses Projekt nicht möglich gewesen.

Ich danke Christoph Konietzko für seine Unterstützung in grammatikalischen und sprachlichen Fragen.

Ein besonderer Dank gilt meinen Kindern Mitja, Ylva, Nikolai und Timur, die mich immer wieder motiviert haben, für ausgezeichnete Ablenkung sorgten und meine häufige Abwesenheit, besonders in den intensiven Phasen der Dissertation, geduldig ertrugen.

Mein größter Dank gebührt meiner Partnerin Belinda Bracklow, die mir über die Jahre eine unverzichtbare Stütze war. Ohne ihren unermüdlichen täglichen Einsatz und ihre moralische Unterstützung hätte ich diese Arbeit nicht bewältigen können.